Titel

MODEL-BASED DAMAGE FEATURE EXTRACTION FOR STRUCTURAL-HEALTH MONITORING APPLICATIONS

Dissertation

zur Erlangung des Grades

des Doktors der Ingenieurwissenschaften

der Naturwissenschaftlichen-Technischen Fakultät

der Universität des Saarlandes

von

Christian Dürager

Saarbrücken

2018

Tag des Kollopuiums: 10.12.2018

Dekan: Univ.-Prof. Dr.rer.nat Guido Kickelbick

Berichterstatter:

Prof. Dr.-Ing. Christian Boller

Prof. Dr. Wieslaw Staszewski

Vorsitz: Prof. Dr.-Ing. Joachim Rudolph

Akad. Mitarbeiter: Dr.-Ing. Joachim Schmitt

Contents

Nomenclature

$\beta_{0,1}$	Assumed step size
Δr	Difference between real- and estimated distance
δr	Uncertainty for propagation distance
$\epsilon_{1,2}$	Threshold parameter
Γ_{A0}	Estimated dispersion coefficient A_0 wave pulse
Γ_{S0}	Estimated dispersion coefficient S_0 wave pulse
μ	Step size
ν	Physical process variable
ω	Angular frequency
ω_0	Center frequency
ψ	Chirping coefficient
ψ_{A0}	Estimated chirping coefficient A_0 wave pulse
ψ_{S0}	Estimated chirping coefficient S_0 wave pulse
ρ_μ	Criteria for new step size
τ_0	Wave pulse width
$\triangle t_{\mu C}$	Maximum time delay microcontroller
$\triangle t_{Air}$	Time delay air
$\triangle t_{interface}$	Maximum time delay
Ξ	Sample Space
ξ_D	Damage process variable

ξ_{RE} Random error variable

ξ_{SE} Systematic errors variable

$a(s), b(s)$ polynomials

a^k Unknown Parameters (Model-based)

A_0 First antisymmetric Lamb wave mode

$A_{A_{0inc}}$ Estimated amplitude A_0 wave pulse

a_m discrete Fourier coefficient

A_n Wave pulse amplitude

a_n Wave pulse parameter

$A_{S_{0inc}}$ Estimated amplitude S_0 wave pulse

b_0 Slope of straight line

c_g Group velocity

c_p Phase velocity

e Error

E_{A_0inc} Incident wave pulse A_0

E_{A_0ref} Reflected wave pulse A_0

E_n Individual wave pulse

E_{S_0inc} Incident wave pulse S_0

E_{S_0ref} Reflected wave pulse S_0

$F(t)$ measured signal envelope

F_y, F_x Forces

F_{est} Estimated signal envelope

g	Gravity, $g = 9.080655\ \frac{m}{s^2}$
HT	Hilbert Transform
I	Index parameter
J	Jacobian
$J(a^k)$	Jacobian
k	Wave number
$k(\omega)$	Wave number depending on the frequency ω
k_0''	Dispersion coefficient
k_1	Wave number symmetrical mode
k_2	Wave number symmetrical mode
k_{max}	Maximum number of iteration steps
L	Length of string
m	Order of polynomial
m_k	Simpler model function
r	Propagation distance
R_{pe}	Internal resistor
S	Squared error
s^k	Correction factor
S_0	First symmetric Lamb wave mode
$S_{1,2,3}$	Sensor positions
S_D	Damage process
s_D	Damage sequence

S_P Physical process

S_{RE} Random error process

$s_{RE}(t)$ Random error sequence

S_{SE} Systematic error process

$s_{SE}(t)$ Systematic error sequence

T Tension

t Discrete time variable

$TOA_{A_{0inc}}$ Estimated time of arrival A_0 wave pulse

$TOA_{S_{0inc}}$ Estimated time of arrival S_0 wave pulse

v Wave velocity

v_0 Initial wave velocity

$x(t)$ Measured signal

x_0 Initial guess

$x_{base}(t)$ Measured data - pristine state

x_{damage}, y_{damage} Coordinates real damage position

$x_{estimate}, y_{estimate}$ Coordinates estimated damage position

$x_E(t)$ Estimated signal

x_k Solution for non-linear optimization problem

$y(t)$ Output signal

y_0 Distance from starting point

Acknowledgment

Special thanks to Prof. Dr.-Ing. Christian Boller from the University of Saarland, and Prof. Dr. Manfred Morari from the ETH Zurich for supporting me during this thesis with words and deeds. In addition, I would like to say thank you to Dr. Andreas Brunner and Dr. Michele Griffa from EMPA for their qualified support. Also a big thanks to the EMPA and SR Technics teams for their support. Before closing, I would like to thank all involved colleges, friends and family members for their support during the development of this thesis.

Abstract / Zusammenfassung

Zusammenfassung

Das Thema automatische Strukturüberwachung ist seit mehr als zwei Jahrzehnten ein wichtiges Thema im Bereich Wissenschaft und Forschung. Auch wenn der Nutzen der Strukturüberwachung für die Industrie unumstritten ist, sind bis heute nur wenige Anwendung aus der Praxis bekannt. Ein Grund dafür ist die relativ hohe Anforderung an die Messsignalauswertung; eine Schädigung an der Struktur hat nur einen relativen geringen Einfluss auf das gemessene Signal im Vergleich zu anderen Einflüssen. Aus diesem Grund wird in dieser Dissertation eine neue Möglichkeit für die Erkennung von Schädigungsmerkmalen innerhalb von gemessenen Signalen vorgestellt. Vorteil der hier vorgestellten Methode gegenüber derzeit bekannten Methoden ist die Möglichkeit auch schwer zu erkennende Schädigungsmerkmale (z.B. geringe Amplitude, überlappte oder stark verrauchte Signale) innerhalb des gemessenen Signals zu identifizieren. Am Beginn der Arbeit wird der aktuelle Stand der Wissenschaft im Bereich Signalverarbeitung für Strukturüberwachungsaufgaben diskutiert. Der eigentliche wissenschaftliche Schwerpunkt, eine neue Methode zur Erkennung von schädigungsrelevanten Kennzeichen innerhalb eines gemessenen Signals, wird im Hauptteil der Arbeit vorgestellt und erklärt. Die Machbarkeit der vorgestellten Methode, wird anhand von synthetischen Signalen und anhand einer realen Anwendung gezeigt. Am Ende der Arbeit werden die Ergebnisse zusammengefasst und die Grenzen der Methode aufgelistet.

Abstract

The topic of automatic structural health monitoring has been an important topic in science and research for more than two decades. Although the benefits of structural health monitoring for the industry are undisputed, only few practical applications are known to this day. One reason for this is the relatively high requirement on the measurement signal evaluation; a Damage to the structure has only a relatively small effect on the measured signal compared to other influences. For this reason, this dissertation presents a new possibility for the detection of

damage features within measured signals. The advantage of the present method in compare to currently known methods is the ability to estimate even difficult to identify damage characteristics (e.g., low amplitude, overlapped or noisy signals) within the measured signal. At the beginning of this work the current state of science in the field of damage feature extraction for structure health monitoring applications will be discussed. The actual scientific focus, the invention of a new method for damage feature extraction within a measured signal is presented and explained in the main part of the thesis. The feasibility of the presented method is demonstrated based on synthetic signals and also based on a real application. At the end of the thesis, the results are summarized and the limits of the method are listed.

1 Introduction

The detection of damages in structures at the earliest possible time is of great interest for operators of infrastructure, whether it be for civil structures such as for example bridges or offshore oil platforms, or transportation systems such as for example aircrafts or trains, because it will enable to operate the infrastructure safe and economical. Clearly, the safety aspect is obvious and in our days a very high standard of safety is achieved by inventing maintenance and inspection procedures such as predefined maintenance intervals and/or non-destructive testing (NDT) procedures during specific periods. Even economical aspects are also essential when it comes to damage detection. As an example, an evaluation of an unforeseen damage due to fatigue on an aircraft during its operation can lead to extensive downtimes which would entail additional cost due to passengers claims and additional operational costs. But not only unforeseen damage can lead to an economical loss, also established maintenance procedures are sometimes very cost intensive when it comes to inspection at hard to access locations because sometimes the time needed for providing the access to the inspection area exceeds the actual inspection time. For example, to inspect the bold holes in an aircraft fuel tank several days are needed for providing the access whereas the actual inspection needs only 0.5 hours.

An other aspect for damage detection is the original designed life time of the infrastructure because with increasing age the possibility for damages to the structure is more likely. If one further consider that many of the existing infrastructures are currently nearing the end of their original design life time it can be expected that the effort for damage detecting will increase in the future. But with the actual existing and established damage detection methods the increasing need for inspection could not be covered. It is for that reason why new damage detection strategies where established in the past. Damage detection is usually carried out in the context of one or more closely related disciplines that include [1] :

- structural health monitoring (SHM),
- condition monitoring (CM),

- non-destructive testing (NDT),
- health and usage monitoring (HUMS),
- statistical process control (SPC),
- damage prognosis (DP).

The term structural health monitoring (SHM) usually refers to the process of integrating a damage detection strategy for aerospace, civil or mechanical engineering structures in order to monitor the structure or mechanical system over time. The different aspects of SHM will be discussed in more detail in the section 1.2 - *Background on Structural-Health Monitoring*. Condition monitoring (CM) is analogous to SHM, but specifically addresses damage detection in rotating and reciprocating machinery [2]. Non- destructive testing (NDT) is a common used damage detection method for a wide field of applications. In compare to the above mentioned detection methods, for NDT the structure has to be taken out of operation which can be also decelerated as off-line whereas SHM and CM are on-line inspection methods where the structure can be monitored during their operation. Health and usage monitoring (HUMS) are closely related to CM with a special focus on damage detection for rotorcraft drive trains. Statistical process control (SPC) is process-based rather than structure based and uses a variety of sensors to monitor changes in the process [3]. Once damage has been detected, the term damage prognosis (DP) describes the attempt to predict the remaining useful life of a system [4].

Non-destructive testing (NDT), condition monitoring and SPC are methods already established and recognized methods for damage detection and their applications are present in all different fields of infrastructure monitoring. However, in the near future these methods will not sufficiency enough to handle with the increasing use of infrastructure and the associated growing demand for damage detection. It is therefore a widely belief that damage monitoring will change more and more to structural health monitoring applications (SHM) because it enables the monitoring of structures during its operation which in turn can reduce the needed maintenance effort because only in case of a detected damage a repair or

change of the component will be needed [1]. Therefore, this thesis will focus primarily on SHM.

1.1 Background on Structural-Health Monitoring

In discussions with people not involved in the topic of structural-health monitoring, the first question is always: "What is structural-health monitoring?" The second question is: "Why is monitoring of a structure needed at all?" Although this thesis deals mainly with one specific part of structural-health monitoring, i.e., damage feature extraction, a very brief explanation of structural-health monitoring (SHM) and the reasons for its existence will be given to begin with. For a more in-depth discussion of the SHM topic, the interested reader is referred to the literature on SHM, e.g. [5], [6] or [7] .

1.1.1 Damage tolerance

In 1951 a new type of aircraft design for high altitude service, the Comet I developed by the UK Havilland Aircraft Company, entered service. In 1954 tragic accidents occurred with the planes, originated by fatigue crack propagation leading to the disintegration of the pressurized fuselage. Failure analysis revealed that although designed and tested for the conditions found in service, the design was defective as concerns crack arrest capability. As a lesson learned from the Comet accidents the design philosophy for new aircraft changed from crack arrest capability towards the philosophy based upon damage tolerance.

The philosophy of damage tolerance assumes that damages in the aircraft structure are unavoidable and measures are taken for its control along the aircraft life cycle. This leads to weight savings and therefore lightweight structures, but also to increased maintenance costs, particularly those related with periodical inspections. In compare, the safe life design philosophy means that the structure is designed such that it is able to withstand a defined fatigue life, normally termed in flight hours, without any inspection being required. Once the fatigue life has

been achieved and the load spectrum has not been exceeded, the component has to be replaced. The damage tolerant design philosophy in turn allows for damage to grow. This may be either achieved such that a crack grow at any time up to a certain where it then be stopped by a crack stopper or the component will have fractured and the loads transferred by that component will be transferred by some other component. Damage tolerance can however also be based on assuming a crack to be available at a badly inspect able location and to determine how much the crack is allowed to grow until it finally reaches a critical stage [8].

With damage tolerant aircraft, inspection intervals are defined on the basis of acceptable damage propagation. Starting from an initial defect size corresponding to greater undetectable size using conventional inspection tools (e.g.., visual- or NDT inspection), the number of flight cycles up to critical dimensions is estimated [9]. That means, essential ingredients of these approaches are the knowledge of crack propagation as related with applied loading, and periodical inspections with a frequency that undetected damage in one inspection will not grow up to critical size before next inspection.

Although lightweight structures have undeniable advantages and their development offers great potential for saving costs, there is one decisive drawback: because of their optimized design, lightweight structures are more prone to fatigue damage such as cracks and fractures. If recognized at an early stage, the fatigue damage is not a problem for the integrity of the structure, but this proviso leads to the need for periodic inspections of the structure. To return to the example of aircraft, there are established inspection intervals at which some problematic points on the structure must be inspected. These inspections are time-consuming in themselves, but in some cases an even greater effort may be required in order to obtain access to the problematic points. Thus, for a 30-minute inspection, the time required for gaining access for the inspection may be several hours, and in 80% to 90% of cases no damage will be found.

The question is, how can such large numbers of unnecessary inspections be avoided? One approach is based on the idea that the structure itself could rec-

ognize damage and immediately notify the operator about the issue. This corresponds with the idea of structural-health monitoring. In a nutshell, SHM implies a system integrated into the structure which operates with autonomy and informs the operator in the event of damage to the structure [7]. This results in a reduction in the number of inspections required and, in the ideal case, access to a neuralgic point of the structure is only needed in the event of identified damage. Therefore, it should be possible to increase the efficiency of the lightweight concept.

As already mentioned in the introduction, potential applications for SHM can be identified in the whole area of infrastructures. For example, Farrar and Worden showed in their book some interesting applications to civil infrastructures [1], whereas Staszewski et al. focused more on SHM application related to aerospace [6].

In this thesis the focus is on application for the aerospace industry. This is because most of the present work and experiments were carried out on airframe structures, but nevertheless, the ideas present in this thesis are also applicable for other areas of infrastructure.

In principle, SHM cannot be explained as an isolated idea, but rather as an integrated system consisting of different sub systems or components, such as for example:

- *Method*: for the detection of a possible damage (e.g. Ultrasonic Testing, guided waves),
- *Sensors*: as a connecting link between the structure and the SHM system,
- *Signal Acquisition*: in order to read and convert the data from the sensors,
- *Signal- or Data Processing*, for extracting the desired information about possible damage from the measured data,
- *Damage Estimation*: for calculating the damage location,
- *Damage Assessment*: which includes different assessment levels [10]:
  - Level 1 = damage identified,

– Level 2 = position of the damage,

– Level 3 = size of the damage,

– Level 4 = type of damage,

– Level 5 = possible implication for the structural integrity.

Each component of the SHM system is necessary for the functioning of the whole system and every individual component has to be developed for the respective application. For example, in cases where propagating waves are used for the detection of a damage to the structure, a different kind of sensor is needed compared with cases where mechanical stresses are used for identifying damage to the structure. For a better illustration all above listed components of the SHM system are shown in Fig.(1).

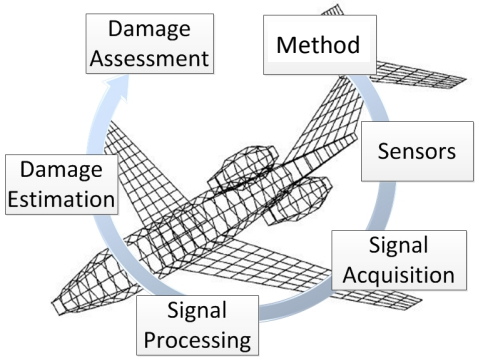

Figure 1: Principal components within a typical structural-health monitoring system.

The first two components, the method and sensors, of the above described SHM system are depending on the respective application. For instance, when vibration data is used for damage detection the method of mode analyses or resonance frequencies may applied, whereas for detection of damages within the structure

the method of guided waves can lead to lead a successful detection of a damage. The choice of the respective sensors is strong linked with the applied method. Even though both components have to selected and developed carefully their application follows a straight forward approach and many handbooks about the respective methods and sensors are available.

The situation is different for the remaining components; Their development needs a in deep knowledge about data processing and because of the unpredictable behaviour of a damage event very often the problem is associated with non-linear performance. It is for that reason why the data processing forms the central intelligence of the entire structure system - it reflects the functionality of the structure and monitors its operational reliability. In other words, the data processing enables the structure to "feel". When the term data processing is mentioned in connection with SHM, following partial aspects may involved [1]:

- data acquisition,
- data preprocessing (e.g. filtering),
- damage feature extraction,
- damage estimation,
- damage classification,
- structure assessment.

Due to its significance for the structure system, the topic of data processing is subject to scientific investigation using various approaches. Some of these approaches are rudimentary and their applications are limited to simple monitoring functions, whereas other approaches employ more intelligent monitoring strategies such as, for example, artificial neural networks or machine learning algorithms. Even when such approaches are capable of realizing the basic physical behaviours of structures, their application is limited to previously known physical effects. However, the behaviour of a damage event to the structure is not in any way predictable.

In this work, the main focus is on several aspects of the above mentioned data processing topic, mainly:

- data acquisition and preprocessing,
- damage feature extraction,
- damage estimation.

The data processing approach introduced in this work is quite different: the process displays the different physical effects within the entire structure system based on mathematical models, and the mathematical models are capable of being adapted to physical effects which are not known in advance. As a result, the process identifies the parameters or features relevant to a damage even when they were not previously known or were hidden by other structural effects. This represents a clear improvement in the damage feature extraction and the entire structure system compared to the currently available data processing strategies, and will significantly accelerate achievement of the overall aim –a feeling structure for real applications.

Although the present thesis concentrates mainly on the topic of data processing, at least as important for the structure system are the other necessary parts such as sensors, the sensor arrangement and the data acquisition system, and without consideration of these components the introduction of a structure monitoring system would not be complete. Consequently, in this thesis the various components of a structural health monitoring system are introduced, and if they were not commercially available, these components were newly developed for the purposes of this work, with the aim of a real application for damage detection on thin plate-like structures. The tests on the entire structure monitoring system or structural-health monitoring system, including introduced and developed components and the resulting outcomes, are described at the end of the thesis.

1.2 Some Notes for the Reader

As previously mentioned, the main focus in this work is on a novel data processing method for the extraction of damage-related features within a measured signal.

A more general discussion of the data processing issue for damage identification in structures is given in chapter 3. Here, the physical process of signal measurement and effect of damage inside a structure on the measured signal is discussed. The current state of the art in the field of data processing for damage detection in structures is illustrated based on a classification matrix for the different data processing methods. All the illustrated methods are discussed in chapter 3.

In chapter 4, the concept of model-based damage feature extraction is introduced. The chapter starts with a high-level view on the introduced concept in order to give the reader a broader perspective on the data processing problem, and the reader is cautioned regarding the applicability of the presented theory to other signal processing problems. In the second part of chapter 4, the data processing concept is explained using a real problem based on measured Lamb waves in thin plate-like structures. The feasibility of the whole data processing concept is proven at the end of chapter 4. For the proof of concept, a synthetic signal was used in this work.

Although the main scientific part of this work deals with data processing for measured signals from solid structures, in the last two chapters two different SHM systems for damage detection are presented. In chapter 6, an SHM system for monitoring the integrity of aircraft fuselage skin panels is presented. The whole SHM system was developed within the framework of this thesis, and it consists of the following parts:

1. Several piezoelectric transducers fix bonded to the structure,
2. Wireless measurement devices connected to each sensor,
3. Model-based damage feature extraction algorithm,
4. Nonlinear damage position estimation algorithm.

All the individual components are discussed together with the results in chapter 6. In the end of this thesis a short summary including the limitations of the herein present methods will be discussed, followed by the outlook for the next steps.

2 Damage Feature Extraction Procedure

The principal aim of structural-health monitoring is clear –to identify and, in the best case scenario qualify, the damage to a structure. These two main items, identifying and qualifying the damage, constitute the purpose of the damage feature extraction process and indicate the importance of the process in the structural-health monitoring system. A damage-sensitive feature is some quantity extracted from the measured system response data that indicates the presence (or not) of damage in a structure [1]. Although this statement is accepted by the SHM community, there remains a need to clarify the question of why the process of damage identification and qualification is seen as complicated. In order to answer this question in the next section the underlying processes involved during a damage event to a structure will be discussed.

This chapter is organized as follows: Firstly, the basic physical process involved in the damage process in a structure and the resulting measured signal will be explained. This leads the reader to the intrinsic problem of analysing a signal for damage monitoring of structures. In the second part of this chapter, existing signal processing or damage feature extraction procedures are discussed, and a novel classification matrix is presented for the various methods with different levels of functionality. The various methods listed in the matrix are discussed in the last section of the chapter.

2.1 Underlying Processes

The processing of the data is performed with one goal in mind –to extract the desired information and reject the extraneous data [11]. The first important issue is that of identifying the desired information. Of course it is perfectly clear that if we are looking for damage inside a structure, the desired information is about such damage, but in many cases this damage is not visible from outside, e.g., a crack or delamination inside the structure. In order to identify this kind of hidden damage, appreciably different methods and processes can be applied, always depending on the respective application (structure, expected damage). Strictly speaking, the

process of damage estimation consists of several processes which are illustrated in Fig.(2).The big gray box < underlying damage estimation process > on the schematic drawing shows the principal physical process used for damage identification inside the structure of interest, (e.g., wave propagation or stress and strain measurements) and the "damage process" which means the effect of the damage on the principal physical process, such as, for example, a wave reflected from an area of internal damage to the structure. Both processes will form the output of the underlying damage estimation process, which in theory is an idealized output without any noise or errors.

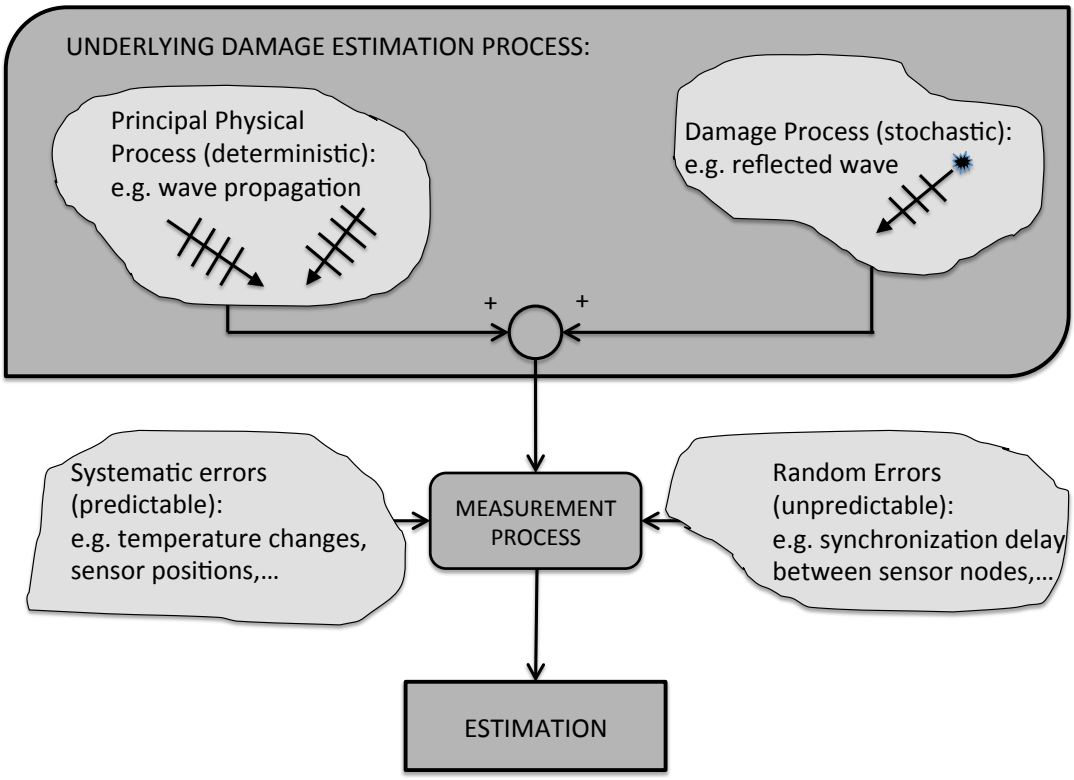

Figure 2: Process map of the damage estimation process with the different physical processes involved.

In reality however, all measurements are an approximation to the real process under investigation because measurements are always affected by uncertainties

such as noise or errors. Errors can be caused by, e.g., temperature changes, which may affect the physical behaviour of a structure or may have other effects on the measurement process which are previously known and therefore reproducible. Therefore, these types of errors are predictable.

Another type of error which is not predictable is called a random error. Random errors can be affected by electronic noise or synchronization delays between wireless nodes.

2.1.1 Mathematical Process Models

In the above subsection, the different physical processes involved in the damage feature estimation procedure were explained, together with their temporal behaviour. This general view of the procedure is not sufficient for the development of the mathematical models needed for the model-based approach proposed in this work. Therefore, in this subsection the more general process map from Fig.(2) above will be translated into the mathematical model structure displayed in Fig.(3). The mathematical description of the different processes involved follows this illustration of the damage feature extraction procedure.

Principal Physical Process, $S_P(t, \nu)$:

When it is assumed that there are no uncertainties, either systematic or random, the structure response process in the pristine state (without damage) can be interpreted as a deterministic process, which means that the process is repeatable and continued measurements from the process reproduce an identical sequence over and over again. Mathematically, a deterministic process can be expressed as:

$$S_P(t, \nu) \quad \nu \in \Xi, t \in I \tag{1}$$

where I is a set of index parameters and Ξ is the sample space. As already mentioned, the principal physical process is a deterministic process, which means that t[1] and ν are deterministic. The corresponding output of the baseline process

[1]Since the text in this thesis is predominantly concerned with discrete time, the usual time symbol t is used as a discrete-time index

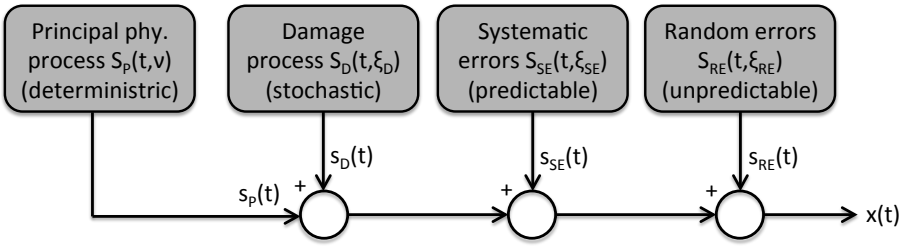

Figure 3: Characteristic flow chart of the measured signal $x(t)$ composition. The different processes involved are summed to form the resulting signal $x(t)$ which, in turn, is the signal containing the hidden information about possible damage to the structure.

is a discrete deterministic sequence defined by:

$$s_P(t) := S_P(t, \nu) \tag{2}$$

where all parameters and time events are previously known.

Damage Process, $S_D(t, \xi_D)$:

The process of damage appearance is quite different from the principal physical process and can be seen as a random process because neither the location nor the size of the damage is known in advance, and furthermore, the time of occurrence of the damage is not previously known. The output of the damage process is a sequence with several unknown parameters, such as unknown time, location or amplitude, and these unknown parameters are the features of interest –the damage features. A stochastic process can be expressed mathematically as:

$$S_D(t, \xi_D) \quad \xi_D \in \Xi, t \in I \tag{3}$$

where I is a set of index parameters and Ξ is the sample space. For the case of a damage process it is assumed that t and ξ_D both vary, and therefore the whole process is considered as a random time function [11]. The corresponding output discrete random sequence of the damage process S_D is defined by:

$$s_D(t) := S_D(t, \xi_D) \tag{4}$$

and this is a particular realization of a stochastic process in which each distinct value of time can be interpreted as a random value. Thus we can consider the outcome of a damage process as a sequence of ordered (in time) random variables.

Systematic Errors, $S_{SE}(t, \xi_{SE})$:

The third process which has an influence on the measured signal $x(t)$ is the process of systematic errors. Systemic errors are predictable and typically constant or proportional to the true value. Systematic errors can be caused by, e.g., interference with the measurement process from the environment, such as temperature changes or environmental vibrations. The output of the systematic error process is the sequence $s_{SE}(t)$ consisting of unknown but predictable parameters in time t and sample space ξ_{SE}.

Random Errors, $S_{RE}(t, \xi_{RE})$:

Random errors are always present in the measurement process and are unpredictable. They are affected by the inherently unpredictable fluctuations in the readings of the measurement apparatus. For example, for wireless networks, the synchronization signal between the different nodes changes slightly between every measurement, which has a direct effect on the measurement results. As an outcome from the random error process $S_{RE}(t, \xi_{RE})$ we obtain a sequence $s_{RE}(t)$ consisting of unknown and unpredictable parameters in time t and sample space ξ_{RE}.

Resulting Signal, $x(t)$:

All the separate sequences together form the resulting discrete measured response signal $x(t)$, as illustrated in Fig.(3) above. When we consider the measured signal as a discrete random signal, its definition is as follows:

$$x(t) := s_P(t) + s_D(t) + s_{SE}(t) + s_{RE}(t) \tag{5}$$

All the uncertainties within a measured signal, whether predictable or unpredictable, make the identification of damage-related features difficult. This applies not only to the analysis of measured signals from structures, but also in various other engineering fields such as speech recognition or automatic heart-rhythm recognition. Although the objective is to extract the features of interest from a measured signal, the analysis methods differ, mainly because of the different underlying physical or biological processes. It is for exactly that reason that separate extraction strategies for the identification of damage-related features are needed.

2.2 Damage Feature Extraction Processes: State of the Art and Some Theoretical Background

The process of damage feature extraction is not a new concept; it was needed from the outset of the development of structural-health monitoring in order to identify the interesting features within a measured response from the structure. Concepts already in use include some well-known signal analysis methods, e.g., Fourier or wavelet transforms, and other methods related to the scientific field of data prediction and parameter estimation. Different methods provide different types of results. For example, results from analysis methods based on transforms provide information about the spectral representation of the signal, whereas results from prediction methods contain more physical information about the underlying processes. Another useful source of diagnostic features is to build a physical or data-based parametric model of the structure; the parameters of these models or the predictive errors associated with these models than become the damage-sensitive features.

To the best of the author's knowledge, no classification of the different damage feature extraction methods is currently available, and therefore this study starts with the invention of a classification system as illustrated in Fig.(4). The idea behind the classification system is to list the different analysis methods and group them into six different levels, starting with the first level, which represents the lowest level of mathematical complexity, and progressing through the levels to methods with a more complex mathematical background. Simultaneously, the level of complexity corresponds with the ability of the methods to handle measured data with different levels of uncertainty. For example, the methods in the lowest level are only able to process data which have almost no uncertainty, while in the highest level the data may contain uncertainties, predictable or unpredictable.

The main advantage of the novel damage feature extraction method introduced in this work is its ability to extract the features of interest even when these features are overlapped by other features with a much higher amplitude within the analysed signal. Therefore, the damage feature extraction procedure introduced in this work corresponds with Level 6 on the damage feature extraction classification diagram illustrated in Fig.(4).

2.2.1 Level 1: Measurement Comparison

The lowest level, Level 1, involves no explicit mathematical model; it is based on measured data in the pristine condition of the structure, which can be interpreted as a type of baseline model for comparison with all subsequent measurements. If there are any changes in the measured data, the comparison process indicates the difference between the pristine state and the actual measured data 5. Mathematically, the baseline method can be expressed as vector subtraction between the actual measured data $x(t)$ and the data measured in the pristine state $x_{base}(t)$ of the structure:

$$y(t) = x_{base}(t) - x(t) \tag{6}$$

where y is the difference signal and t is the discrete time index. A major drawback of this method is the fact that different measurement conditions can also

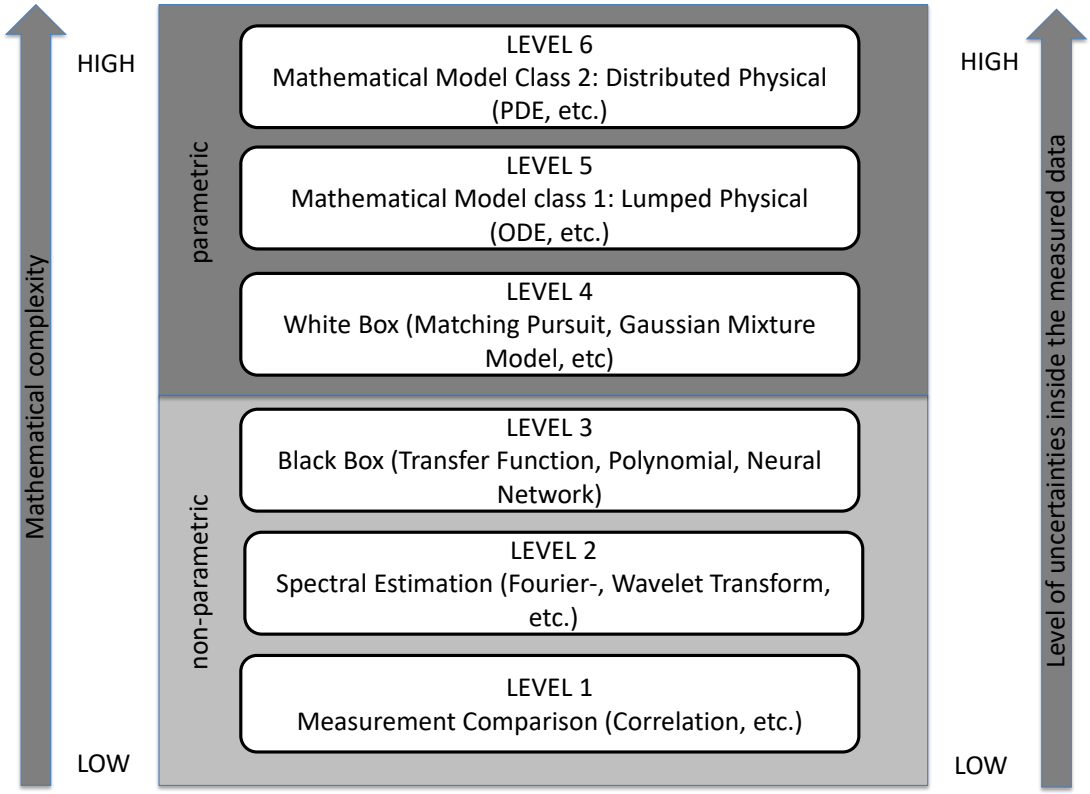

Figure 4: Comparison between different damage feature extraction methods: levels of complexity and uncertainty. The first three levels are non-parametric analysis methods. Starting from Level 4, the analysis methods are parametric, and the two highest levels use a model-based approach.

affect the resulting measured data, and as a consequence, the correlation with the baseline measurement indicates some differences which are not caused by damage. Therefore, this method is limited to applications with consistent conditions, e.g., laboratory conditions.

Worden et al. [12] or Farrar et al. [1] , in their work on the fundamental axioms of structural-health monitoring, made a clear statement that all damage feature extraction methods are based on a comparison between different states or conditions of the structure. In addition, the authors state the following. "The fact that damage detection algorithms require a comparison of system states is at the root of one of the main problems in SHM. If the normal condition or base-

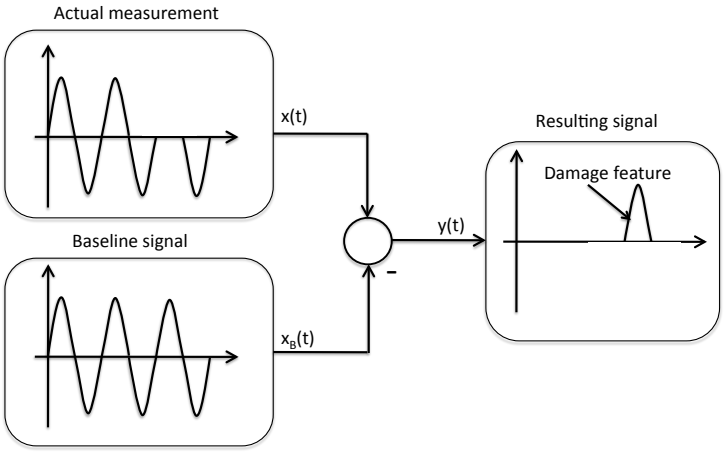

Figure 5: Example of a damage feature extraction process in Level 1: baseline subtraction.

line state changes as a result of environmental or operational variations, then the application of a novel detection algorithm may yield a false-positive indication of damage." For example, Farrar et al. [13] found during their experiments that the day-night temperature cycle affects the measured response data from the structure more than a possible defect in the structure. In order to overcome the influence of temperature differences on the measured response signal, Croxford et al. [14] implemented a temperature compensation strategy. They used two different methods for compensation of the temperature effect: optimal baseline selection and baseline signal stretching. Satisfactory experimental results were obtained when both methods were combined. The analysis of the proposed method leads to several guidelines for practical implementation of temperature compensation. Liu et al. [15] invented in their work a method for baseline correction by reconstructing the baseline signal at the temperature of the current signal. They used the orthogonal matching pursuit for compensating the amplitude of baseline signal. Several literature can be found for temperature compensation of baseline measurements when guided waves are used for damage detection e.g. [16], [17] or [18].

2.2.2 Level 2: Spectral Estimation

In the next level, the mathematical model incorporates little a priori information and is used to analyse the information content (spectrum, time-frequency, etc...) of the raw measurement data, in an attempt to draw some rough conclusions about the nature of the signals under investigation (Fig. (6)). The gaol of the spectral estimation is to estimate the spectral density of a random signal from a sequence of time samples of the signal. The spectral density characterizes the frequency content of the signal. The technique of spectral estimation is common used for monitoring of rotating machineries such as for example gear- or bearing applications and the application on rotating machinery has made the transition from research topic to actual practice [1], [19].

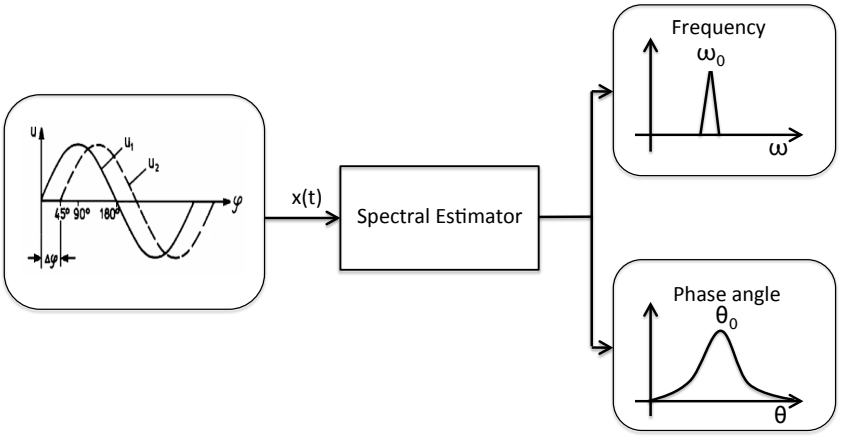

Figure 6: Typical example of a spectral estimation process: analysis of two sine waves.

Fourier Transform

If a signal is discrete and periodic then it can be represented by a Fourier series [20]. The discrete Fourier series representation of a signal is given by the pair

$$x(t) = \sum a_m e^{j\omega_m t} \tag{7}$$

and

$$a_m = \frac{1}{M} \sum x(t) e^{-j\omega_m t} \tag{8}$$

where a_m are the discrete Fourier coefficients and $e^{-jx} = cos(x) - jsin(x)$. These relations imply that the discrete signal under investigation can be decomposed into a unique set of harmonics. In other words, the representation of the signal as a Fourier series enables us to extract spectral content from the signal, and the corresponding coefficients can be considered as an equivalent representation of the information in the signal under investigation. However, the information about the harmonic base functions has global support. For example, in decomposing a signal where a discontinuity in time is present, all the weights of the basis function will be affected; the phenomenon of discontinuity is diluted. Therefore, FT is usually used for stationary signals [21].

Short-Time Fourier Transform

The classical Fourier transform is a very strong signal analysis tool for stationary signals. However, for non-stationary signals it fails to describe how the frequency evolves with time. For these types of signals the short-time Fourier transform (STFT) is used, as it is able to extract the frequency content of the signal and its corresponding time value. The STFT breaks up the non-stationary signal into small segments, so-called windows, and then the FT is applied to each segment to ascertain the frequencies that exist in that segment. These spectra, taken together, indicate how the spectrum varies in time [21, 5]. However, the STFT windowing process results in a trade-off between the time and the frequency resolutions, and therefore accuracy cannot be obtained simultaneously in both time and frequency domains.

The method of STFT is very commonly used for analysing measured response

signals from structures, since the STFT gives a very brief overview of the frequency spectra of the signal. Here, only the most cited publications are named, e.g., Ihn and Chang [22] or Giurgiutu and Cuc [23]. Droubi et al. [24] used in their work for the processing of measured data from acoustic emission data the Fast-Fourier Transform in order to extract the spectral information.

Wavelet Transform

The wavelet transform (WT) breaks up a signal into a series of wavelets that are shifted and scaled. The functional basis consists of dilated and shifted versions of a single basis function called a mother wavelet, which can be seen as a wave packet. The WT has the advantage that it can adjust the window length according to the needs of the real signal. Therefore, detailed information (high-frequency components) can be obtained with a narrow window and general information (low-frequency components) with a wide window. A good introduction to WT is given in the book by Staszewski et al. [10], where the two main types of WT, the continuous wavelet transform and the discrete wavelet transform, are described. However, the WT has difficulty in picking up the correct wavelet for a specific target signal, and therefore the application of WT requires considerable knowledge and experience.

A good overview about wavelet transform for SHM applications is given in the compendium provided by Reda Taha et al. [25] although the work was done in 2006. More actual, Shaopeng et al. [26] used the so called empirical wavelet transform (EWT) for analysing multi-mode signals gained from acoustic emission data. The idea of EWT is decompose a signal accordingly to its contained information. Sarrafi et al. [27] combined the wavelet transform with a probabilistic model in order to overcome the problems with uncertainties coming from operational/environmental variability. A novelty approach for the design of a mother wavelet for the processing of measured signals from guided waves is presented in the work from Chen et al. [28]. They used a emitted tone-burst signal as mother wavelet for the detection of damage features caused by corrosion.

Summary: Spectral Estimation

In summary, all damage feature extraction methods which are based on transforms are powerful tools when the information about possible damage in the structure is hidden in the frequency content of the signal. Examples of such applications are primarily in the field of civil infrastructures, where the frequency behaviour of the structure under investigation is analysed. Due to the outdated infrastructure in many countries, SHM applications for civil structures have become very popular in the last few decades, leading to many publications. For example, Amezequita et al. [29] and Noel [30] used the WT for extracting information about vibration from the measured signal. For other damage detection methods, e.g., guided ultrasonic waves, the application of transfer methods is limited to signals where the damage-related features are clearly separated from other features in the signal. Staszewski et al. [10] used the WT for analysing measured signals obtained from guided ultrasonic wave propagation. They filtered out the information about the different wave modes within the measured signal.

2.2.3 Level 3: Black Box Models

At the next level are black box models, which are basically used as data prediction mechanisms. They have a parametric form (polynomial, transfer function, etc.) but there is little physical information that can be gleaned from their outputs. The black box model means that we know only the input $x(t)$ and the output $y(t)$ of the system, but the system itself is not known. The behaviour of the system is derived using data prediction mechanics such as polynomials or transfer functions. Examples for black box models are [1]:

- Look-up table models,
- Curve fitting,
- Transfer function,
- Neuronal networks.

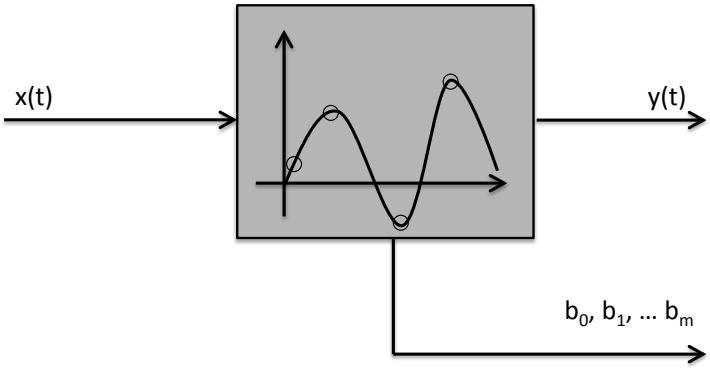

Figure 7: Black box model: example of curve fitting by polynomial interpolation.

Curve Fitting:

One commonly used data prediction method is fitting of various types of functions, e.g., polynomials, exponential functions or sine and cosine functions, to the measured data. In many cases, a polynomial of a certain degree will be appropriate as a rudimentary model, as illustrated in Fig.(7). A simple example of a curve-fitting model is that of a straight line. Here the polynomial equation is given by

$$y = b_0 + b_1 x \tag{9}$$

where b_1 is the slope of the straight line. For more complex data, such as a simple curve, the degree of the polynomial equation must be expanded to a higher order m as follows.

$$y = b_0 + b_1 x + ... + b_m xm \tag{10}$$

Park et al. [31] measured the deformation of a steel beam using a strain gauge fibre-optic sensor and extracted the information about the deformation from the measured data using a 2^{nd} order polynomial equation.

Neural Networks

One damage feature extraction method which can be associated with a black box model is the method of artificial neural networks (ANNs) or only neuronal networks. This method has been frequently used in the last few decades. ANNs are biologically inspired artificial intelligence representations that mimic the functionality of the nervous system. Similar to biological neural networks, ANNs consist of a set of transfer functions which can be discontinuous, (e.g., symmetrized Heaviside step function), continuous or linear. The goal of the ANN is to solve problems in the same way as the human brain, and this means that the ANN must learn from defined and known data in order to be able to interpret measured data. Even though the ANN is biologically inspired, the underlying physical process, in the best case, may be approximated by polynomials. One of the first know applications of Neuronal Networks for damage feature extraction was invented in 2001 by Sohn et al [32]. They present a Neuronal Network algorithm in their paper with the general purpose of feature extraction and data reduction that contain the maximum amount of information from the original data set. For the fundamentals of ANNs, see, for example, Haykin [33].

Due to its popularity, the ANN method is increasingly finding its way into SHM applications. For example, Su and Ye [34] extracted spectrographic features from Lamb wave signals in the time-frequency domain to construct a damage parameters database (DPD). The DPD was then used off-line to train a multilayer feed forward ANN under the supervision of an error back-propagation algorithm. In his book, Giurgiutiu [5] gave a short introduction to ANNs and their possible uses in SHM applications. Based on the example of measurement data from electromechanical impedance (EMI) experiments on thin circular aluminium plates with different damage locations, the functionality of ANNs in applications with EMI measurements was demonstrated. Lam et al. [35] used a combination of the pattern recognition method and the Bayesian ANN design method to form a practical SHM methodology. In their damage detection method, they proposed Ritz vectors as pattern features to detect the damage location and severity; these changes correspond to the differences between the measured Ritz vectors for the

undamaged and the possibly damaged structures. The functionality of the method was demonstrated using analytical models. Bao et al. [36] described in their work an approach of reducing the noise within measured data by transforming signals in images and training a deep neural network for anomaly classification. For machine health monitoring Zhao et al. [37] used different methods of deep-learning. The compared and discussed the results in order to give a overview of possible application. Cha et al. [38] invented in their work a visual inspection system in combination with a deep-learning algorithm to avoid the human factor during visual inspection.

Transfer Function

Another possibility for predicting the behaviour of the system without knowing the physical principles of the system, is to derive a so-called transfer function from the input and output data, (e.g., [39]). In principle, the dynamic behaviour of a linear system can be described by differential equations in the time domain,

$$a_n \frac{d^n y}{dt^n} + a_{n-1} \frac{d^{n-1} y}{dt^{n-1}} + ... + a_1 \frac{dy}{dt} + a_0 y = b_m \frac{d^m x}{dt^m} + ... + b_1 \frac{dx}{dt} + b_0 x,\ n \geq m, \quad (11)$$

where x is the input and y is the output of the linear system. When the initial state of the linear system is assumed to be without energy and furthermore the Laplace transform [40] ($y(s) = L\{y(t)\}$, $x(s) = L\{x(t)\}$) is applied to the differential equation the above differential equation changes to,

$$\begin{aligned} &a_n \cdot s^n \cdot y(s) + a_{n-1} \cdot s^{n-1} \cdot y(s) + ... + a_1 \cdot s \cdot y(s) + a_0 \cdot y(s) = \\ &b_m \cdot s^m \cdot x(s) + b_{m-1} \cdot s^{m-1} \cdot x(s) + ... + b_1 \cdot s \cdot x(s) + b_0 \cdot x(s). \end{aligned} \quad (12)$$

The quotient $\frac{y(s)}{x(s)}$ forms now the transfer function $G(s)$,

$$G(s) = \frac{y(s)}{x(s)} = \frac{b_m \cdot s^m + b_{m-1} \cdot s^{m-1} + ... + b_1 \cdot s + b_0}{a_n \cdot s^n + a_{n-1} \cdot s^{n-1} + ... + a_1 \cdot s + a_0} = \frac{Z(s)}{N(s)}. \quad (13)$$

The transfer function of a linear system is thus a rational function,

$$G(s) = \frac{b(s)}{a(s)} \tag{14}$$

where the polynomials $a(s)$ and $b(s)$ are given by equation (12) and the transfer function is not any more depending on the input- and out signals.

Much literature can be found on the topic of transfer functions for damage feature extraction. Here, only the papers that are the most relevant from the point of view of the author are briefly mentioned.

Zang et al. [41] presented a possible method for correlating measured frequency responses from multiple sensors and proposed to use these correlated responses as an indicator for structural damage detection. They developed one transfer function for the pristine state of the structure and a second transfer function for all subsequent responses of the structure, and correlated both transfer functions. Experiments on real structures showed that the algorithm required further investigation, leading to the combination of the transfer function method with neural networks. Lanza di Scalea et al. [42] estimated in their work the dynamic transfer function between two outputs of a linear system subjected to an uncontrolled and generally unknown excitation and possible uncorrelated noise present at both outputs. They demonstrated that by taking in account the normalizing factor for the two outputs the linear system works stable also for unknown excitation.

Summary: Black Box Models

The examples illustrated above represent only a few data prediction methods, and the list of suitable methods can be expanded to include others, such as least mean square estimation or more sophisticated methods.

Black box models are very often used for applications on civil structures like bridges and one of the reason is the problem of the identification of the physical properties of the structures because their development phase was many years (decades) ago. Examples for black box models used for the monitoring of bridges can be found in e.g. [43] or [44]. Park et al. [45] used displacement measurement taken by different linear sensor for performing a inverse structural analysis of a steel beam.

Nevertheless, there is still little physical information that can be gleaned from the output of black box models.

2.2.4 Level 4: White Box Models

Progressing to Level 4, white box models are evolved that can use the underlying black box structures; however, now the parameters can be used to extract limited physical information from the data as illustrated in Fig.(8). For instance, a black box transfer function model fitted to the data yields polynomial coefficients that can be factored to extract resonance frequencies and damping coefficients, characterizing the overall system response being measured. In this chapter only the below listed examples of White Box Models will be discussed,

- Matching Pursuit,
- Gaussian Mixture Model.

A more complete list of possible white Box Models for SHM application can be found in the book about machine learning provided by Farrar et al. [1].

Matching Pursuit

In recent years another damage feature extraction method has become very popular; the matching pursuit (MP) method. The idea of MP is to find a solution to the problem of approximate data by comparing the measured data with a set of redundant data (library) functions. The library may include functions such as wavelets or Fourier sets and the algorithm automatically chooses the function $f(n)$ within the library which is optimal for the representation of a given signal $x(t)$. In the first step, this is an approximation. A criterion for the optimality of a given solution can be formulated as the minimization of the error. Finding the minimum error requires checking all the possible combinations (subsets) of functions from the library, leading to a combinatorial explosion. Therefore, the problem is intractable even for moderate library sizes.

Mallat and Zhang [46], in 1993, first proposed the MP method for decomposing any signal into a linear expansion of waveforms selected from a redundant library

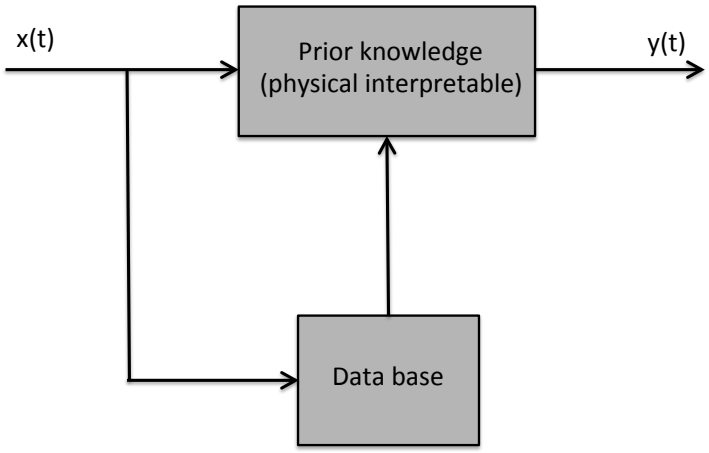

Figure 8: Basic structure of a white box model for damage feature extraction.

of functions. Their work showed that even where the MP is a very powerful tool for analysing and coding signals, some effort has to be made to find ways of reducing the high dimensionality of the library.

Raghavan and Cesnik [47] combined chirplet matching pursuit with a mode correlation check for single-point sensors. In their work they demonstrated the functionality of the proposed algorithm using numerical and experimental results. The proposed algorithm was able to separate overlapping multimodal reflections and estimate the radial locations of defects.

A different approach for solving the problem of identification of damage features within measured response signals, uses guided ultrasonic waves (GUW). This approach was taken by Xu et al. [48], using MP with Gaussian and chirplet libraries to decompose and approximate Lamb waves and extract the wave parame-

ters. They stated that the Gaussian library-based MP is optimal for decomposing symmetric signals, whereas the chirplet library-based MP is able to decompose asymmetric signals, e.g., dispersed Lamb waves.

Marchi et al. [49] used a time-frequency procedure based on the warped frequency transform (WFT) to process multimodal and dispersive Lamb waves for structural-health monitoring (SHM) applications. The WFT was combined with a basic pursuit algorithm to extract the distance travelled by the ultrasonic waves, even in the case of the multimodal dispersive propagation associated with broadband excitation of the waveguide. They proved the concept of the algorithm based on a real thin aluminium plate with artificial damage.

Probabilistic Methods –Gaussian Mixture Model

In signal processing, probabilistic methods for feature extraction are commonly used for a wide range of applications. Examples include:

- Speech recognition,
- Image analysis,
- Biomedicine,
- Control applications,
- Seismology.

Thus, it is not surprising that probabilistic signal processing methods are also used for SHM applications. The most relevant studies are highlighted below.

An overview of statistical signal processing for fault detection is given in two papers by Worden et al. [12], [2] and in the work of Kulkarni and Achenbach [50]. Numerous publications are available discussing the processing of data obtained from vibration-based monitoring methods, and therefore only the most well-known studies are named here, e.g., [51], [52] and [53]. Flynn et al. [54] used a Rayleigh-based statistical model of scattered wave measurements in combination with a maximum likelihood algorithm for damage location in guided ultrasonic wave applications.

A relatively new probabilistic approach for damage signal processing is the so-called Gaussian mixture model. The basic idea of this method is to estimate, in the first step, the damage index from the measured response signals and, in the second step, to calculate the probability of a possible damage to the structure using all involved Gaussian models. As a result of the mixture of Gaussian models the damage-related feature is identified. A good overview of Gaussian mixture models is given by Qiu [55]. This study demonstrated the feasibility of the Gaussian mixture model for damage estimation using a practical example.

2.2.5 Level 5: Mathematical Model Class 1

Progressing up the levels, Level 5 introduces true model-based techniques that explicitly incorporate the process physics using a lumped physical model structure, usually characterized by ordinary differential or difference equations (ODE). The lumped physical model simplifies descriptions of the behaviours of physical systems by approximating the behaviour of the distributed system under certain assumptions. A typical ordinary differential equation contains one or more derivatives of an unknown function $y(t)$ which can be determined from the equation. The equation may also contain y itself, as well as given functions and constants. For example, in a general form an ODE can be written as

$$F(x, y, y^{'}, ..., y^{(n-1)}) = y^{(n)} \tag{15}$$

where x is a given function and y is a unknown function. This type of ODE can be solved using numerical methods.

For example, if we drop a stone, then its acceleration can be calculated by

$$y^{''} = \frac{d^2y}{dt^2} \tag{16}$$

which is equal to the acceleration due to gravity ($g = 9.080665\ \frac{m}{s^2}$). Equation (16) is only an approximation to reality because we ignore the air resistance. By integration we obtain the velocity

$$y^{'} = \frac{dy}{dt} = gt + v_0, \tag{17}$$

where v_0 is the initial velocity at the beginning of the motion, (e.g., $v_0 = 0$). Integrating once more, we obtain the distance travelled

$$y = \frac{1}{2}gt^2 + v_0 t + y_0, \tag{18}$$

where y_0 is the distance from the start point. This simple example of a stone attracted by the earth's gravity demonstrates the use of ODE for solving physical problems. The problem was first described by the initial 2^{nd}-order ODE y'', and by reducing the degree of the ODE we obtained the distance travelled by the stone y.

For the case a set of differential equations have to solved the single equations can be converted into a form of matrix. The matrix representation of the set of differential equations is known as state-space representation.

More examples of ODE for describing physical phenomena can be found in engineering books such as the famous book by Kreyszig [56], or the book by Giurgiutiu [5] which is more focused on SHM applications.

Applications of lumped physical models for damage feature extraction are limited to simpler physical problems such as vibration-based monitoring methods. For example, Overbey et al. [57] used a state-space model for extracting parameters of interest from simulated vibration data. For validation, the state-space model was subsequently tested in an experiment.

Todd et al. [58] presented a feature extractor for a non-linear time series obtained from vibration-based monitoring methods. They first tuned the excitation for maximum state-space sensitivity and then combined it with a state-space reconstruction approach to yield a feature that was very sensitive to subtle changes in the system. The experiment was based on an eight-degrees-of-freedom system, where damage was imparted as a local stiffness reduction.

Worden et al. [59], in their paper "A review of non-linear dynamics applications to structural health monitoring" provide a good illustration of how to use ODE for solving physical problems based on a cracked beam.

The list of relevant publications is almost endless, but it is obvious that the majority of relevant publications are in the field of vibration monitoring for civil

structures. This is due to the physical simplicity of such engineering systems.

2.2.6 Level 6: Mathematical Model Class 2

It is fair to say that only the simplest physical systems can be modelled by ODE, whereas more complex problems such as wave propagation lead to partial differential equations (PDEs) which are included in the last level, Level 6, of our model-based damage feature extraction scheme. The top level captures distributed physical model structures in the form of partial differential equations. PDEs arise in connection with various physical and geometrical problems when the functions involved depend on two or more independent variables, usually time t and one or more spatial variables.

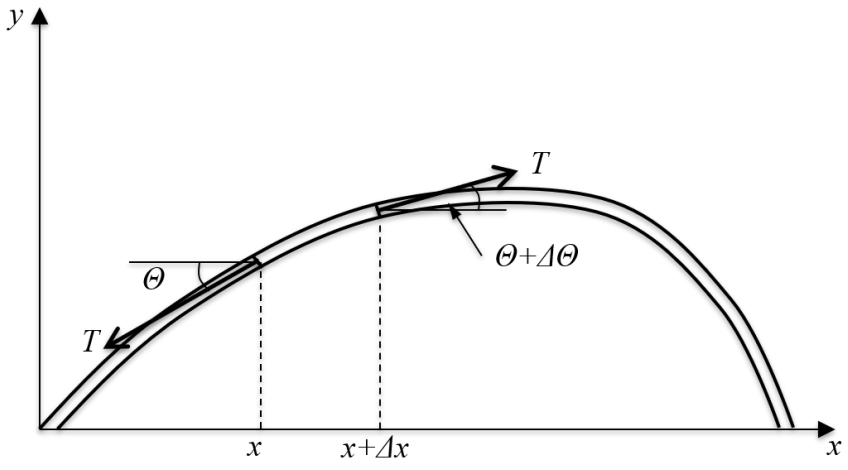

Figure 9: Force diagram for short segment a string in transverse vibration.

In order to give the reader a clearer picture of distributed physical models, an example based on a freely vibrating stretched string is given. We consider a string of length L with its ends held fixed at the points $x = 0$ and $x = L$. The string has a uniform linear density μ and is stretched with tension T (Figure (9)). Now the

string is deformed from its equilibrium configuration, in such a way that a short segment of the string of length δx has a force F acting on it, given by [60]

$$\begin{aligned} F_y &= T\sin(\theta + \Delta\theta) - T\sin\theta \\ F_x &= T\cos(\theta + \Delta\theta) - T\cos\theta \end{aligned} \tag{19}$$

where θ and $\theta + \Delta\theta$ are the directions of tangents to the string at the ends of the segment. With the assumption that the transverse displacement is small, we obtain the simplified version of Eq.(19):

$$\begin{aligned} F_y &\approx T\Delta\theta \\ F_x &\approx 0. \end{aligned} \tag{20}$$

The equation governing the transverse motion of the segment is therefore

$$T\Delta\theta = (\mu\Delta x)a_y \tag{21}$$

where θ embodies the variation of y with x at a given value of time t and a_y embodies the variation of y with time t at a given value of x. When we introduce partial derivatives for the parameters x, y and t and assume the relationship

$$\tan\theta = \frac{\delta y}{\delta x} \tag{22}$$

we obtain

$$\begin{aligned} \Delta\theta &= \frac{\delta^2 y}{\delta x^2}\Delta x \\ a_y &= \frac{\delta^2 y}{\delta t^2}. \end{aligned} \tag{23}$$

Thus Eq.(21) becomes

$$T\frac{\delta^2 y}{\delta x^2}\Delta x = \mu\Delta x\frac{\delta^2 y}{\delta t^2}. \tag{24}$$

When we express Eq.(24) in a more physically meaningful way, we obtain

$$\frac{\delta^2 y}{\delta x^2} = \frac{\mu}{T}\frac{\delta^2 y}{\delta t^2}. \tag{25}$$

Both equations (Eq.(24) and Eq.(25)) are examples of PDEs for a progressive traveling wave on a long string. When we look more closely at Eq.(25), we realize that the factor $\frac{\mu}{T}$ is merely the square of the speed. Therefore the speed of the propagating wave v can be expressed as

$$v = (\frac{T}{\mu})^2 \tag{26}$$

and we can write Eq.(25) in a more compact form:

$$\frac{\delta^2 y}{\delta x^2} = \frac{1}{v^2}\frac{\delta^2 y}{\delta t^2}. \tag{27}$$

This is commonly known as a two-dimensional wave equation [56].

The equation derived here is only one example of a PDE. In order to solve such PDEs more sophisticated mathematical methods must be applied in comparison to the less complicated examples of ODEs. One possible way to solve the problem is by using numerical methods such as the Euler method, the Runge-Kutta method or the Crank-Nicolson method, to name only a few of the available numerical methods [56]. Numerical approaches are very commonly used for the virtual simulation of physical processes, for example, for finite element simulation (FEM) or continuous dynamic simulation. All these numerical methods play an important role in obtaining a thorough knowledge of the physical behaviours of structures, whether in a pristine state or a damaged state. An enormous number of literature articles can be found on this topic, which indicates the importance of virtual simulation in the field of SHM, (e.g., [10, 5]).

It is the assumption of the author; for real time model-based feature extraction,a numerical solution of the PDE may not efficient enough because the time spent on the calculation of the result would be too long. For this reason, an analytical approach is more suitable for solving the PDE. In most cases, and especially for very complex physical processes, the analytical approach is an approximation

to the real physical process, and therefore in this study we consider approximate analytical or mathematical models.

2.3 Chapter Summary

The purpose of this chapter has been to introduce the main data processing methods for damage feature extraction used for SHM applications. In principle it can be distinguished between two main methods [1] ,

- Non-physical parametric models,
- Physical Parametric models.

Non-physical parametric models does not proceed from a law-based physical model and this method is also known as data-based approach [1] . That means, one established training data from all possible healthy and damage states of interest for the structure and then uses non-physical parametric models in order to identify damage relevant features out of the measured data. In principle, for the methods in this class parameters are within the models but in most of the cases this parameters have no physical connection to the physical process of interested. The advantages of non-physical parametric models are lower complexity of the of the data processing methods. On the other hand their feasibility of handle uncertainties with in measured data is limited.

The method based on physical parametric models for damage feature extraction are usually implemented by building a physics-based or law-based model of the process of interest. This can be a numerical model such as for example a finite element (FE) model or a analytical model whereby the latter are sometimes complicated to develop and therefore the complexity may be reduced by an approximation on the real physical process. The mentioned complexity is clear a disadvantage of the method based on physical parameters. But, in case the goal is to extracted as much information as possible about the damage out of the measured signal the method based on physical parameters should be preferred.

3 Model-based Damage Feature Extraction Method Introduced in this Work

When working on a scientific topic, there are important questions regarding the novelty of the work and the benefit the work offers to the scientific community. Both these questions are answered in this chapter.

3.1 Introduction to the Basic Concept

The underlying concept for the extraction of damage features within a measured signal is as follows. In the first step, the measured signal is examined to identify whether it contains a feature caused by damage. As soon as a damage-related feature is identified within the signal, the underlying mathematical model of the damage signal will be adapted to the identified damage signal.

Although this concept is already known from other engineering fields, e.g., for the detection of heartbeats in an electrocardiogram or for speech recognition in modern smart phones, the major challenge faced by the identification of damage features (and the main difference from well-known applications) is the relatively high ratio of regular features within the measured signal to the interesting damage-related features. In other words, the damage-related features will be overlapped and possibly hidden by the regular features within the measured signal.

The solution for this problem, and one of the main innovations in the present work, is the combination of static mathematical models of the underlying physical processes with adaptive mathematical models of previously unknown physical processes, such as a damage event. In order to ensure the detection of small and hidden damage-related features, on the one hand the static mathematical models must be relatively accurate reflections of the underlying physical processes and on the other hand the adaptive models need the ability to adjust to a broad spectrum of possible damage features.

As a further innovation, all unpredictable errors such as synchronization events between sensor nodes or unpredictable environmental effects are considered as

a further adaptive mathematical model which facilitates the application of the present damage feature extraction process to real structures.

In the following sections, the functional principle of the proposed damage feature extraction (DFE) procedure is explained and the idea of model-based feature extraction is introduced. This broader view of the introduced solution will be refined based on an example of a real application where Lamb waves are used for damage detection on thin plate-like structures. At the end of this chapter, the functionality and stability of the proposed DFE procedure is proven based on synthetic input signals. These synthetic signals are calculated in accordance with the expected measured signal $x(t)$ as described in section 2. In comparison to signals measured on a real structure, the use of synthetic signals for the concept proof allows certain parameters of the synthetic signal to be varied within a predefined range. This enables testing of the DFE procedure on a broad spectrum of signal possibilities.

Furthermore, the functionality of the DFE procedure was tested based on real measured data in the framework of the entire structural-health monitoring system introduced in this work. The results are described and discussed in chapter 5.

3.2 Functional Principle of the Proposed Damage Feature Extraction Procedure

In this section, the functionality of the DFE is explained for the case of a general application. The entire DFE procedure with its related processes is illustrated in Fig.(10).

i In the first block < Static mathematical models > shown in Fig.(10) on the left-hand side, the sequences for the principal physical process $s'_P(t)$ and the systematic error $s'_{SE}(t)$ are calculated based on the respective mathematical models of the underlying physical processes. All parameters for both calculations are previously known. The sequences are subsequently summed to represent the input signal for the second block, < Adaptive processes > in Fig.(10).

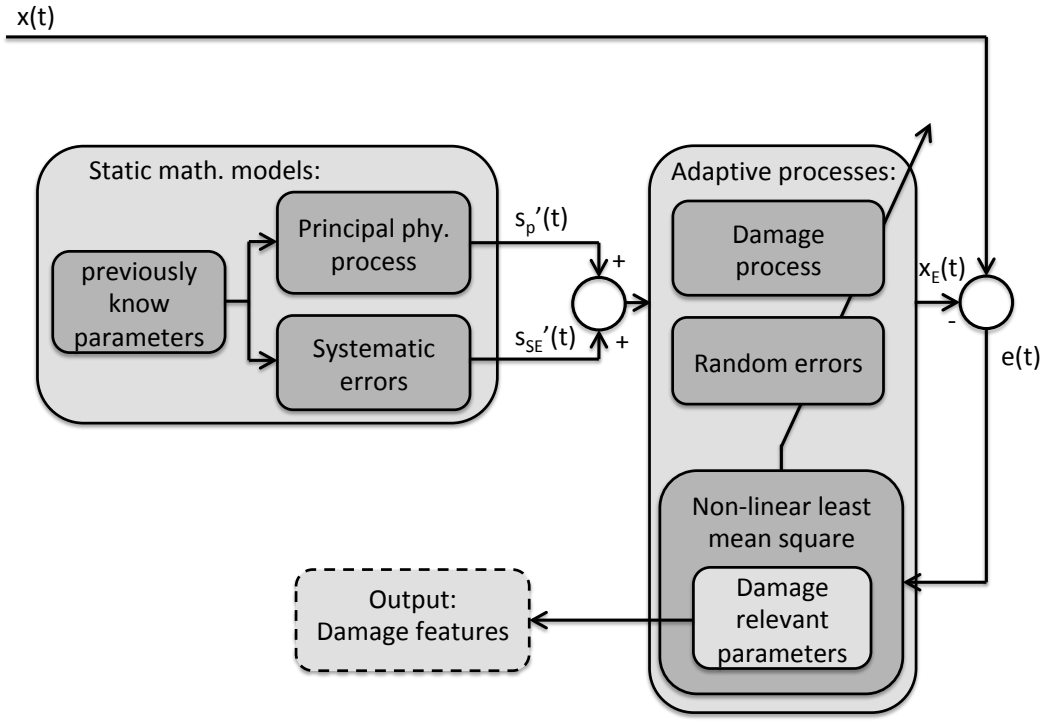

Figure 10: Flow chart of the model-based feature extraction approach introduced in this work. On the left-hand side the static mathematical models are displayed and on the right-hand side the two adaptive processes (damage process and random errors) are displayed together with the nonlinear least mean square.

The major challenge in this first block is the creation of a sufficiently accurate approximation of the mathematical models to the previously known real physical processes involved. The resulting sequence should preferably be an exact reflection of the measured signal for the case where no damage is present in the structure, with no random errors such as changing temperatures involved in the measurement process.

ii The second block < Adaptive processes > forms the core part of the introduced DFE procedure. It consists of an adaptive mathematical model of the damage process and a second adaptive mathematical model of the

random errors. Both models are rough estimations of the expected physical processes. It is important that the mathematical models involved in this adaptive process express the expected physical processes but simultaneously provide the possibility of adapting to the real processes as soon as their sequences occur in the measured signal. For example, a wave pulse reflected from an area of damage to the structure can have its fundamental structure previously approximated, but its incident pulse and its parameters such as amplitude or pulse width are not known in advance, and therefore they can be estimated only after the damage event has occurred and measurements are taken. The output of an adaptive model is the estimated signal $x_E(t)$.

iii The adaptation process of the approximate mathematical models is carried out based on a nonlinear least mean square (NLMS) algorithm. The reason why a NLMS is required is the nonlinear nature of the entire process involved in the damage estimation. As a consequence, the measured signals are also of a nonlinear nature. The task of the NLMS algorithm is to minimize the error e between the measured signal $x(t)$ and the estimated signal $x_E(t)$ by adjusting the unknown parameters of $<$ Adaptive processes $>$. After the error e is reduced to a given minimum, the values of the adjusted parameters coincide with the weighting parameters and contain the parameters or features of the damage. The challenge here is to choose an NLMS algorithm which enables estimation of the parameters across a broad spectrum of possible parameters on the one hand, and on the other hand is able to find a minimum between the estimated signal $x_E(t)$ and the measured signal $x(t)$ when there is a likelihood of errors occurring.

iv As already mentioned above, the goal of the nonlinear least mean square algorithm is to minimize the error between the measured signal $x(t)$ and the estimated signal $x_E(t)$. However, a straightforward concept for the reduction of nonlinear problems does not exist, and therefore the nonlinear behaviour has to be reduced to linear behaviour in a certain area. In this study the approach is as follows. In the first step, the squared error S between the measured signal $x(t)$ and the estimated signal $x_E(t)$ is calculated by:

$$S(a^k) = \left\| x - x_E(a^k) \right\|^2 \tag{28}$$

where a^k are the unknown parameters which will be adapted in order to reduce the error between the measured and estimated signal. In the second step, the gradient of S will be calculated by setting Eq.(29) to zero, in order to minimize the error e.

$$\frac{\partial S(a^k)}{\partial a} = 0. \tag{29}$$

Exact calculation of the gradient is the most comprehensive part of the non-linear least square calculation. Several ways of solving the minimization problem exist. Each method has its advantages and drawbacks, such as calculation speed or stability over a wide range of initial starting points, and the choice of method always depends on the application for which it is used.

3.2.1 A short Introduction to Non-linear Optimization

In principle, most of the non-linear optimization problems are solved iteratively, that means they start at an initial guess x_0 and tries to find a minimum (or maximum) solution of x_k for given function $f(x)$. At each iteration k, the non-linear function $f(x)$ is replaced by a simpler model function m_k that approximates $f(x)$ around x_k. In order to estimate the minimum solution different calculation methods can be applied, where each has advantages and disadvantages and their use is strongly depending on the respective application. The most popular non-linear optimization methods which are introduced in short here are [61]:

- Line search,
- Trust-reagion,
- Newton method,
- Gauss-Newton method,
- Levenberg-Marquardt.

In the line search method, the algorithm chooses a search direction and the step size in order to solve a one-dimensional minimization problem. The advantage of the line search method is its possibility to convergent globally (converges to a local minimiser from an starting point x_0), but it needs a relatively long time for convergence to a minimum and sometimes it do not convergence at all.

The trust-region optimization method works in a similar way as the line search method with the difference that first it define a region around the current best solution, in which a certain model (usually a quadratic model) can to some extent approximate the original objective function. In a next step the trust-region method takes a step forward according to the model depicts within the region. If a notable decrease is gained after the step forward, then the model is believed to be a good representation of the original objective function.

The Newton method uses first and second derivatives which enables to distinguish between global or local minimum. As for the above explained optimization methods, first a initial stating point is given and a quadratic approximation to the objective function is constructed that matches the first and second derivative values at that point. Then the approximate instead of the original objective function is minimized. The minimizer of the approximate function is used as the starting point in the next step and repeat the procedure iteratively. As a advantage the Newton method has superior convergence properties when the starting point is near the solution, but it may fails if initial starting point is far away from the solution.

An improved Newton methods and commonly used methods is the Gauss-Newton method, because it offers the possibility of starting the calculation of the minimum at a distance from the true minimum value but still achieving results within a reasonable time. In the example described in the following section, the Levenberg-Marquardt algorithm is used. This is a modified version of the Gauss-Newton method used for the estimation of the minimum. In comparison to the Gauss-Newton method, the Levenberg-Marquardt algorithm enables the estimation of the minimum even when the initial starting point is relatively far away from the real minimum. The drawback is that it takes somewhat longer than the Gauss-Newton method, which represents a significant disadvantage for the estimation of damage.

To reiterate, the actual minimizing function employed, (e.g., the Levenberg-Marquardt algorithm) is not the innovation in this work. However, the combination of the Levenberg-Marquardt algorithm with the entire model-based concept and its adaptation to the application is one of several innovations introduced.

This section has reviewed the basic ideas behind the damage feature extraction procedure introduced in this work, and has simultaneously indicated a broader range of potential applications. In the next section, the introduced concept is adapted to a real problem, namely, the estimation of damage features within signals measured for Lamb wave damage detection applications.

3.3 Analysing Lamb Wave Signals: A Practical Application

3.3.1 Short Introduction to Damage Detection with Lamb Waves

The physical principle used for the practical demonstration of the model-based damage feature extraction procedure is based on propagating wave pulses in thin solid structures, and their ability to interact with discontinuities in the structure, also known as Lamb waves. The physical principle of Lamb wave damage detection and the main parts of the process introduced in this work are illustrated in Fig.(11).

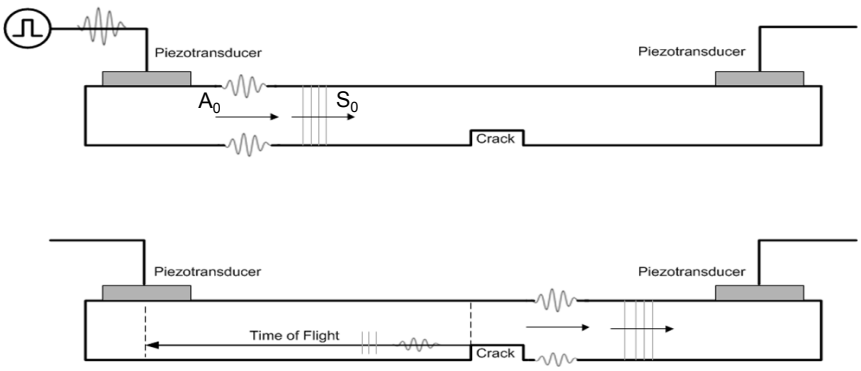

Figure 11: Illustration of the physical principle of damage detection in solid structures using Lamb waves.

The principle is as follows: a wave pulse is excited in the structure by an actuator. This wave pulse propagates through the structure and is reflected and scattered by discontinuities in the structure such as damage. The reflected wave and scattered pulses are detected by sensors and converted back into electrical

signals. These sensors are mounted on the structure surface. The measured signal contains information about the propagation distances of the reflected and scattered wave pulse. This information can be used for the localization of the damage. The possibility of locating the damage in a two-dimensional area is an advantage of the propagating wave method compared to conventional ultrasonic scanning methods.

Lamb waves results from mode conversion phenomena and superposition of reflected dilatational waves and vertically polarized shear waves. Both types of plane waves exist only in certain modes and are described by the dispersion-relations, which relate the phase velocity with the wave number, or frequency, depending on the plate thickness and material properties. The Lamb waves were analytically derived primarily by Horace Lamb [62] in 1917. Lamb waves are divided into symmetric or longitudinal modes and antisymmetric or transversal modes. The dispersion relation for the symmetric modes is given by [63]

$$\frac{tan(\xi_2 h)}{tan(\xi_1 h)} = -\frac{4k^2\xi_1\xi 2}{(k^2-\xi_2^2)^2} \tag{30}$$

and for the antisymmetric modes by

$$\frac{tan(\xi_2 h)}{tan(\xi_1 h)} = -\frac{(k^2-\xi_2^2)^2}{4k^2\xi_1\xi 2} \tag{31}$$

where $\xi_1^2 = k_1^2 - k^2$ and $\xi_2^2 = k_2^2 - k^2$ and k_1 is the wave number of the symmetric mode and k_2 is the wave number of the antisymmetrical mode . The numerical solutions of Eq. 30 and Eq. 31 for an aluminum plate are given in Fig.(12) [64].

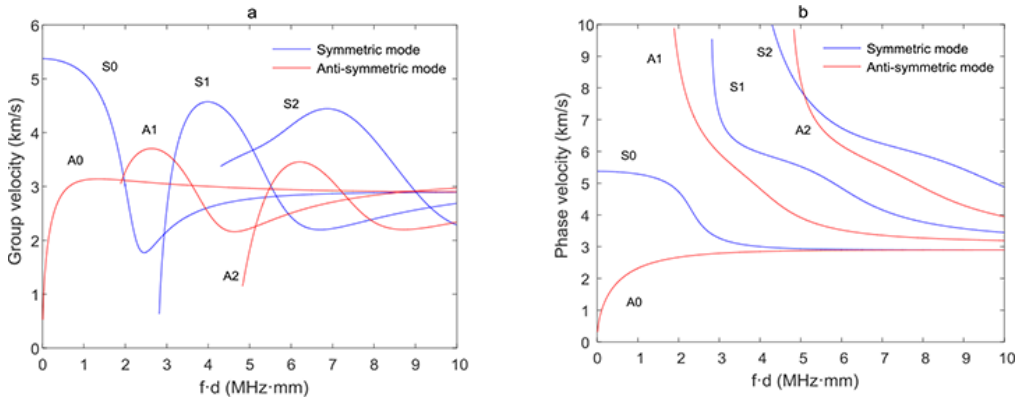

Figure 12: Dispersion curve for symmetric (blue) and antisymmetric (red) Lamb wave mode for an aluminium plate of thickness d [64]

.

One reason why this method is not yet widely used for damage detection is the fact that the measured signals are difficult to analyse. The main problems are:

- A single excited wave pulse spreads out and splits into several wave pulses during propagation,
- Each wave pulse propagates with the same frequency but different wave speed,
- Different wave pulses may interfere during their propagation,
- The propagation behaviour of the wave pulses depends on the environmental conditions.

This study is focused on the development of a prototype process for the localization of damages based on propagating wave pulses. The prototype process consists of:

- An algorithm for extracting the damage-related features from the measured returning signals

3.3.2 Simplified Assumptions to Lamb wave propagation in this work

As already mentioned, the behaviour propagating Lamb waves is highly non-linear and their analytical consideration is very complex and a consideration of all involved physical effects would be beyond the framework of this thesis. Therefore some assumptions and simplifications to the physical behaviour of Lamb waves were made in this thesis:

- Only the first symmetrical (S_0) and first anti-symmetrical (A_0) are considered,
- All effects involved by the actuators and sensors such, as for example non-linearity are not assumed,
- Only the reflected wave pulse form the damage is assumed to be present. The scattered wave pulse is not considered in this work,
- Only isotropic structures are assumed (e.g. aluminium plate). For anisotropic structures, such as for example composite structures, the present damage feature extraction algorithm must be expanded by an attentional mathematical model of the structure.

3.3.3 State-of-the-Art Lamb Wave Signal Analysis

Methods for investigating measured signals can be split into two main groups. In the first group, the properties of the sensor are adapted to the desired behaviour of the propagating pulse. In the second group, signal processing techniques are applied to the measured signal for analysis. The first group includes, for example, the work presented by Giurgiutiu [5] where he adapted the shape of the actuator to the desired mode of the propagating pulse. This makes it possible to selectively excite only one mode. However, overlapping pulses with the same mode cannot be separated by this method. Another approach belonging to the first group is based on sensor arrays. Alleyne and Caweley [65] implemented a 2D Fourier transform method numerically in conjunction with a sensor array. The presented method allowed the identification of individual wave modes even in the most dispersive regions. Giurgiuitiu and Boa [66] developed an embedded ultrasonic structural

radar algorithm using a linear phased array of nine piezoelectric elements. They were able to map artificially induced cracks in an aluminium plate specimen, even when the crack was not in the direct field of view of the array. All methods in the first group have in common that the sensor array is fix bonded onto the structure, and thus it is not possible to adapt the sensor arrays to varying signals.

The second group, comprising the signal processing techniques, can offer more flexibility for varying measured signals. Time-frequency analysis methods are commonly used for analysing measured signals from propagating wave pulses. Prasad et al. [67] used the short-time Fourier transform to extract a suitable parameter from a structural defect. Oseguda et al. [68] and Queck et al. [69] used the Hilbert-Huang transform to process measured data from propagating wave pulses. Another often-used time-frequency-based analysis method is the wavelet transform. This decomposes a signal in terms of waveform packets. Staszewski et al. [10] presented a summary of recent developments in wavelet-based data analysis.

In practice, inspections with Lamb waves are most satisfactorily performed when only one, or occasionally two, guided wave modes are used [70]. Wilcox et al. [71] and Liu et al. [72] introduced a technique for compensating for the effect of dispersion for guided waves. A different approach is presented by Xu and Giurgiutiu. They used a time reversal method to overcome the baseline measurement problem [21]. Several authors have proposed and developed a spectral warping method, i.e., a nonlinear rescaling of the frequency axis to remove dispersion from a signal in the time-space domain using frequency transformation, (e.g., [73], [74] and [75]). As a supplement to this discussion, the principal methods for damage feature extraction are categorized at the beginning of this thesis in section 2.2.

All the above-mentioned analysis methods for interpreting signals from propagating waves have one major disadvantage, namely, the fact that specially educated technicians are needed for setting up the test equipment and for the interpretation of the results. As for traditional NDT inspections, this may lead to misinterpretation of the measured signals due to human factors. Furthermore, the inspection process is very time-consuming. In contrast, the analysis method developed in this work enables the identification of damage features within a measured signal to be

completely autonomous, which helps to minimize errors due to misinterpretation of the measured signal. As well as the advantage of autonomous signal feature identification, the developed analysis process offers further advantages such as:

- It enables the identification of the wave packets in the measured signals and their respective wave modes even when individual wave packets are overlapping,
- The analysis method is able to automatically adjust to different measured signals within a certain range, enabling flexible use,
- Environmental influences such as changing temperatures are automatically compensated for.

In the following, the developed analysis method is presented starting with a description of the underlying theory and followed by an explanation of the different parts and their functions. The method is subsequently verified using synthetic data. At the end of this chapter the limitations of the method are discussed.

3.3.4 Damage Feature Extraction for Lamb Waves Introduced in this Work

The basic idea behind the present damage feature extraction (DFE) procedure for Lamb waves is based on an approximate analytical calculation of the expected wave pulses (in this work only reflected waves from the damage are assumed to be damage relevant features) or wave packets within a measured signal and a nonlinear least mean square (NLMS) curve-fitting algorithm. The whole DFE procedure with its various parts is illustrated in the flow chart shown in Fig.(13).

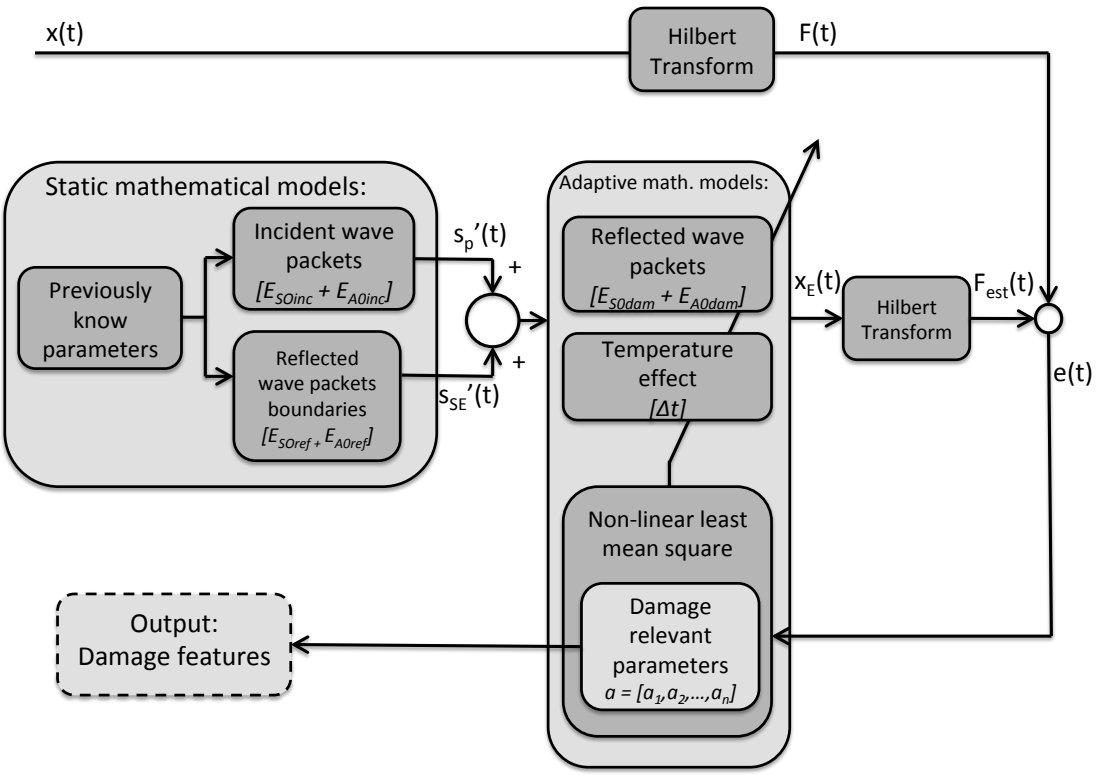

Figure 13: Flow chart of the damage feature extraction procedure for Lamb wave analysis. The core parts of the introduced procedure are the static mathematical models for the incident wave packets and the temperature effect, and the adaptive processes with the two mathematical models of the reflected wave packets from the damage and the synchronization error. In order to reduce the quantity of data required for analysing the measured signal $x(t)$ and the estimated signal $x_E(t)$, their envelopes $F(t)$ and $F_{est}(t)$ are calculated using the Hilbert transform.

The core parts of the illustrated procedure are the static approximated mathematical models for the different wave packets, (e.g., incident waves A_0 and S_0 and reflected waves from the edges of the structure) expected in the measured signal[2] $x(t)$, including the static mathematical model of the temperature effect together with the adaptive process which includes the approximate mathematical model of the expected wave packets reflected from possible damage and the mathematical

[2]The content of the measured signal $x(t)$ is explained in more detail in section (2.1.1).

model of the synchronization error induced by the synchronization delay between different sensor nodes. The working principle of the DFE procedure for Lamb wave signal analysis is as follows.

From the measured signal $x(t)$, the envelope $F(t)$ is calculated using the Hilbert transform. The reduction of the input signal to its envelope helps to reduce the calculation power required for the following comparison between the calculated envelope $F_{est}(t)$ of the estimated signal $x_E(t)$ and the envelope $F(t)$ from the measured signal $x(t)$. The estimated signal $x_E(t)$ is calculated based on the mathematical models consisting of:

- Static approximate mathematical model of the expected wave packets,
- Mathematical model of the temperature effect,
- Adaptive approximate mathematical model of the reflected wave packets from the damage,
- Adaptive mathematical model of the synchronization error between the different sensor nodes.

The real intelligence and the important novelty arise from the adaptive process. The previously discussed approximate mathematical model of the reflected wave packet from the damage and the mathematical model of the synchronization error are linked to the nonlinear least mean square (NLMS) algorithm via a feedback loop to give information about the existing error $e(t)$ between the envelope of the input signal $F(t)$ and the envelope of the estimated signal $F_{est}(t)$. The task of the NLMS algorithm is to adjust the damage-related parameters $a = [a_1, a_2, ..., a_n]$ of the adaptive mathematical models in such a way that the error $e(t)$ is minimized. After the minimum is reached, the calculated parameters correspond to the damage-related features.

3.3.5 Basic Concepts

The drawbacks when using Lamb waves for damage detection and the problems involved in the extraction of the damage-related features were described explicitly above. In order to allow the reader to visualize the problems involved, the lower

graph in Figure (14) shows a typical example of a measured signal from Lamb waves.

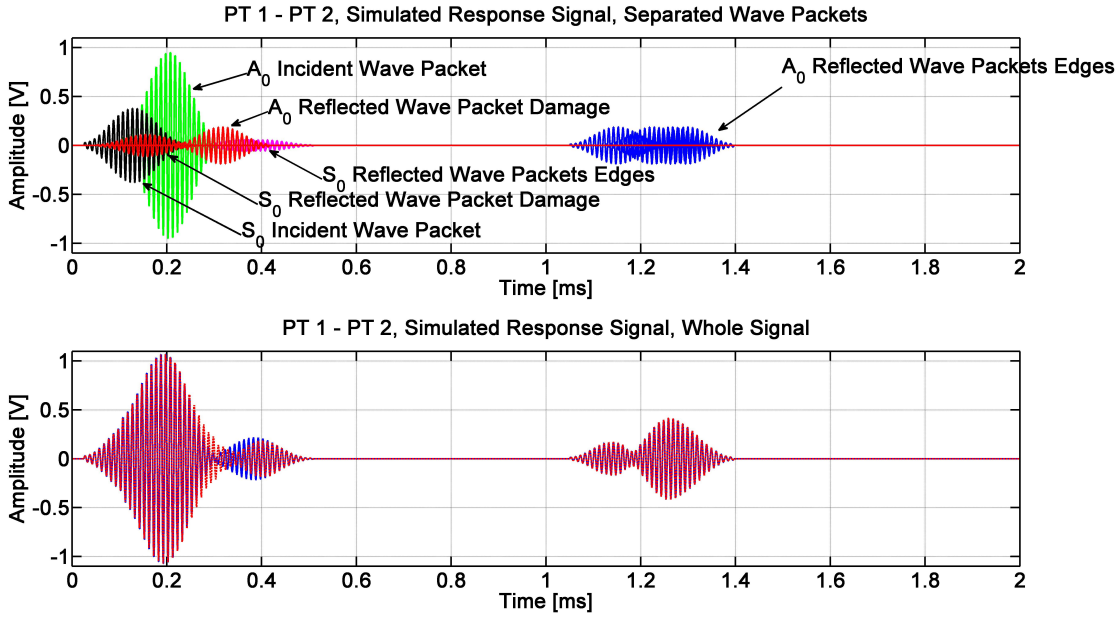

Figure 14: In the lower graph a typical example of a measured signal from Lamb waves at the piezoelectric transducers is displayed. Since the presented signal is simulated, it is also possible to present the single wave pulses within the entire signal (upper graph). Note: the upper graph shows the single wave pulses (not composed) which are contained in the resulting signal (lower graph).

In principle, it is not possible to identify the different wave packets within the illustrated signal in Fig.(14) with the naked eye. In the upper graph, the individual wave pulses within the signal are displayed, and from this it can be imagined how complex the identification of individual wave pulses can be. In the more detailed description of the damage feature extraction procedure, the individual wave pulses are termed E_n . For example, the A_0 incident wave pulse will be termed E_{A_0inc}.

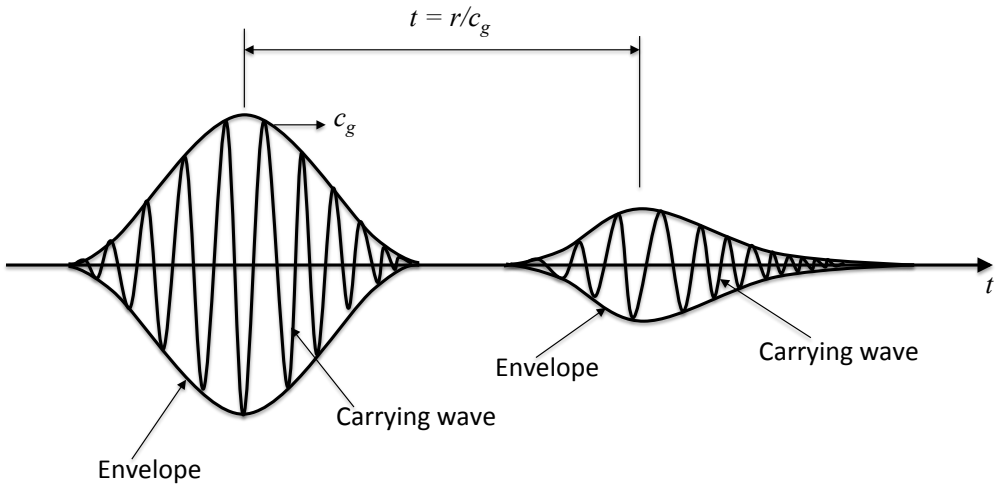

Figure 15: To illustrate the dispersion effect, only one wave pulse is shown in this graph. The initial wave pulse is shown on the left and the same pulse is shown after propagating for a certain distance on the right.

The effect of dispersion on the propagating wave pulses is illustrated in Fig.(15). The initial pulse without the dispersion effect is shown on the left side with its carrier wave and the envelope. After propagating over a certain distance the pulse shown on the right reflects the effect of dispersion on the wave pulse. It can be seen that the shape of the envelope has changed, and further, because of the fact that the high-frequency components of the carrier wave travel at higher speeds, these components are shifted to the right (beginning of the pulse). This is also known as the chirping effect. In this work, the dispersion effect will be termed k_0'' and the chirping effect termed ψ.

All the above influences on the wave pulses are considered in the introduction

of the mathematical model of the single wave pulses involved in the damage estimation process. The general approximate analytical equation for the single wave pulses will be introduced in the next section and the derivation of the equation is explained in more detail in the following section.

Derivation of the Approximate Mathematical Wave Pulse Equation:

In this work, monochromatic waves are of little interest because in its progress, the monochromatic wave acquires no information about a possible disturbance inside a solid structure. The transfer of information from a disturbance requires the variation of one or more of the wave parameters –amplitude or phase. These waves are no longer monochromatic, since their amplitude or frequency is modulated according to the signal transmitted.

In this work it is assumed that the wave pulses propagate as planar waves through a dispersive medium. Fig.(15) shows an example of such a propagating wave pulse in a dispersive medium. A single wave pulse consists of :

- **Carrying wave**: propagates with phase velocity c_p, frequency = excitation frequency
- **Envelope**: propagates with group velocity c_g , frequency < excitation frequency

For the derivation of the approximate mathematical equation used for the mathematical models, we first assume a single wave pulse in the frequency-space domain $\hat{E}(r, \omega)$, whose spectrum is narrowly concentrated in the neighbourhood of frequency ω_0 , at a distance[3] r. At the initial position $r = 0$, the equation for the wave pulse changes to $\hat{E}(0, \omega)$ with an effective frequency band $\mid \omega - \omega_0 \mid \leq \Delta\omega$, where $\Delta\omega << \omega_0$. The spectrum now consists of a low-frequency component, the envelope $\hat{F}(0, \omega)$ and a high-frequency component, i.e., the carrier wave $\hat{E}(0, \omega)$ where the link between both frequency components of the wave pulse is given by [76].

$$\hat{E}(0, t) = \hat{F}(0, w - w_0). \tag{32}$$

[3]The wave pulse is assumed to travel on a 1D axis referred to as r

By applying the modulation property of the Fourier transform to Eq.(32) the corresponding time-domain signal is given by

$$E(0,t) = e^{jw_0 t} F(0,t) \tag{33}$$

which is a sinusoidal carrier modulated by a slowly varying envelope. The equation for the envelope in the time domain is given by [76] as follows.

$$F(0,t) = \frac{1}{2\pi} \int_{-\infty}^{\infty} e^{j(\omega-\omega_0)t} \hat{F}(0,\omega-\omega_0) d\omega \tag{34}$$

If the wave pulse is now launched into a dispersive medium, the pulse propagated to distance r will be given by

$$E(r,t) = \frac{1}{2\pi} \int_{-\infty}^{\infty} e^{j(\omega_0 t - k_0 r)} \hat{F}(0,\omega-\omega_0) d\omega \tag{35}$$

where $k(\omega)$ is the wave number, which depends on the frequency ω. The relationship between wave number $k(\omega)$ and the distance of travel of the wave pulse is as shown below.

$$k(\omega) = \frac{\omega t}{r} \tag{36}$$

Because $\hat{F}(0,\omega-\omega_0)$ restricts the effective range of the integration to a narrow band about ω_0, $k(\omega)$ can be expanded to a Taylor series about ω_0:

$$k(\omega) = k_0 + k_0'(\omega-\omega_0) + \frac{1}{2}k_0''(\omega-\omega_0)^2 + ... \tag{37}$$

where $k_0 = k(\omega_0)$, $k_0' \frac{dk}{d\omega} = \frac{1}{c_g}$ is the inverse of the group velocity and $k_0'' = \frac{d^2k}{d\omega^2}$. The second derivative of the wave number k_0'' is referred to as the dispersion coefficient, and is responsible for the spreading of the wave pulse. Inserting Eq.(37) in Eq.(35) we obtain:

$$F(r,t) = \frac{1}{2\pi} \int_{-\infty}^{\infty} e^{j(\omega-\omega_0)t - j(k-k_0')r - jk_0'' r \frac{(\omega_0-\omega)}{2}} \hat{F}(0,\omega-\omega_0) d\omega \tag{38}$$

The solutions of this integral in the time and frequency domains are shown below.

$$F(r,t) = \frac{1}{\sqrt{2\pi j k_0'' z}} exp\Big[- \frac{t - k_0' r}{2 j k_0'' r} \Big] \hat{F}(0, \omega - \omega_0) \tag{39}$$

$$\hat{F}(r,\omega) = e^{j k_0' r \omega} e^{-j k_0'' r \frac{\omega^2}{2}} \hat{F}(0,\omega). \tag{40}$$

In this work, it is assumed that the wave pulses propagate as Gaussian wave pulses. The envelope for a Gaussian wave pulse at initial position $r = 0$ is calculated as [76]

$$F(0,t) = exp\Big[- \frac{t^2}{2\tau_0^2} \Big] \tag{41}$$

and in the frequency domain as

$$\hat{F}(0,\omega) = \sqrt{2\pi\tau_0^2} e^{-\tau_0^2 \frac{\omega^2}{2}}. \tag{42}$$

The envelope $\hat{F}$ in the frequency-space domain for a launched wave pulse can be calculated by inserting Eq.(42) in Eq.(40), leading to

$$\hat{F}(r,\omega) = \sqrt{2\pi\tau_0^2} e^{-\tau_0^2 \omega^2/2} e^{j k_0' r \omega - j k_0'' r \omega^2/2} \tag{43}$$

Transferring Eq.(43) into the time domain gives

$$F(r,t) = \sqrt{\frac{\tau_0^2}{\tau_0^2 + j k_0'' r}} exp\Big[- \frac{(t - k_0' r)^2}{2(\tau_0^2 + j k_0'' r)} \Big]. \tag{44}$$

Thus, we effectively have the replacement $\tau_0^2 \rightarrow \tau_0^2 + j k_0'' r$. Assuming that k_0' and k_0'' are real, we find the magnitude of the propagating wave pulse as follows:

$$|F(r,t)| = \underbrace{\Big[\frac{\tau_0^4}{\tau_0^4 + (k_0'' r)^2} \Big]^{1/4}}_{\text{Amplitude of wave pulse}} \underbrace{exp\Big[- \frac{(t - k_0' r)^2 \tau_0^2}{2\sqrt{(\tau_0^2 + (k_0'' r)^2)}} \Big]}_{\text{Envelope shape of wave pulse}} \tag{45}$$

where we used the property $|\tau_0^2 + j k_0''| = \sqrt{\tau_0^4 + (k_0'' z)^2}$. It can be assumed that the carrier wave $E(r,t)$ will not be affected by the dispersion effect, and therefore

the equation for the traveling wave pulse in a dispersive medium is given by

$$E(r,t) = F(z,t)e^{j(\omega_0 t - k_0 r)} \tag{46}$$

Putting together the carrier wave and the envelope of the wave pulse leads to the following equation.

$$E(r,t) = \underbrace{\left[\frac{\tau_0^4}{\tau_0^4 + (k_0'' r)^2}\right]^{1/4} exp\left[-\frac{(t-k_0' r)^2 \tau_0^2}{2\sqrt{(\tau_0^2 + (k_0'' r)^2)}}\right]}_{\text{Amplitude and Envelope shape of wave pulse}} \underbrace{e^{j(\omega_0 t - k_0 r)}}_{\text{Carrying wave}} \tag{47}$$

Eq.(47) is valid for a propagating wave pulse in a dispersive medium. As well as the center frequency, further frequency components exist within the carrier wave. High-frequency components propagate at higher wave speeds in comparison to low-frequency components. This separation of the frequency components leads to chirping of the carrier wave. In this work, the chirping of the carrier wave is taken into account using the additional term $\frac{\psi t^2}{2}$, resulting in the following wave pulse equation used in this work:

- **Approximate Analytical Equations:**
  For the calculation of the individual previously known propagating wave pulses $E_{S_0 inc}$, $E_{A_0 inc}$, $E_{S_0 ref}$ and $E_{A_0 ref}$ expected within the measured signal $x(t)$, the equation for a plane wave propagating in a dispersive medium is used. The equation is as follows.

$$E_n(r,t) = \underbrace{\left[\frac{\tau_0^4}{\tau_0^4 + (k_0'' r)^2}\right]^{1/4}}_{\text{Amplitude of wave pulse}} \underbrace{exp\left[-\frac{(t-k_0' r)^2 \tau_0^2}{2\sqrt{(\tau_0^2 + (k_0'' r)^2)}}\right]}_{\text{Envelope of wave pulse}} \underbrace{e^{j(\omega_0 t + \frac{\psi t^2}{2} - k_0 r)}}_{\text{Carrying wave}} \tag{48}$$

  It is assumed in this work that the wave pulse propagates as a Gaussian wave pulse with a pulse width τ_0 through the structure. The other parameters in Eq.(48) are: the propagation distance r, the time t, the wave number k, the inverse of the group velocity $k_0' = \frac{1}{c_g}$, the dispersion coefficient k_0'', the angular frequency ω_0 and the coefficient for chirping ψ.

  All single calculated wave pulses will be summed in the output sequence of

<Static mathematical models> and supplied as input for < Adaptive mathematical models >, as illustrated in Fig.(13). The main difference between the wave pulses assumed for the static mathematical models and the adaptive mathematical models is the possibility of varying certain parameters of the approximated mathematical equation, and therefore Eq.(47) can be modified as follows:

$$E_n(r,t) = a_{1n} exp\Big[- \frac{(t - k_0' a_{2n})^2 \tau_0^2}{2\sqrt{(\tau_0^2 + a_{3n}^2 a_{2n}^2)}} \Big] e^{j(\omega_0 t + \frac{a_{4n} t^2}{2} - a_{2n})} \tag{49}$$

where the adaptive parameters are the amplitude of the wave pulse (first part of Eq.(48)) which is the new adaptive parameter a_{1n}, the propagation distance r which is the new a_{2n}, the wave number k_0'' which is the new a_{3n}, the dispersion coefficient k_0'' and the chirping coefficient ψ which is the new a_{4n}. All adaptive parameters $a = [a_{1n}, a_{2n}, ..., a_{4n}]$ and their corresponding parameters used for the static mathematical model are listed in Table (1).

Table 1: Wave pulse parameters of the parameter vector a^k.

Wave pulse parameter	a_n	Description
A_n	a_{1n}	Wave pulse amplitude
r	a_{2n}	Wave pulse propagation distance
k_0''	a_{3n}	Dispersion coefficient
ψ	a_{4n}	Chirping coefficient

- **Envelope calculation:**
  For the calculation of the envelope, the Hilbert transform is used in this work. The two envelope signals F and F_{est} are calculated using the following equations.

$$F_{est} = HT(\sum_{i=1}^{n} E_n) \tag{50}$$

$$F = HT(x(t)) \tag{51}$$

Here, E_n are the different wave pulses estimated using the approximate analytical equation given by Eq.(49). The term HT indicates the Hilbert transform for the calculation of the envelope signals.

- **Non-linear least mean square parameter estimation (NLMS):**
  For fitting the parameters of the approximated signal x_E to the parameters of the input signal $x(t)$ the Levenberg-Marquardt algorithm for nonlinear least square calculation is used[4].

3.3.6 Sequence of the Damage Feature Extraction Algorithm

The sequence of the DFE algorithm described in the flow chart in Fig.(13) is as follows:

1. Start first iteration step $k = 0$ $(k = 1, 2, ..., k_{max})$
   - Initial parameter vector $a^0 = [a_{1n}, a_{2n}, ..., a_{4n}]$; n is the number of wave pulses E_n within the estimated signal x_E
   - Set initial step size μ^0
   - Set $\beta_0 = 0.25$ (assumed step size criteria)
   - Set $\beta_1 = 0.75$ (assumed step size criteria)
   - Set threshold value for minimum allowed squared error $\left\|S\right\|$: ϵ_1
   - Set threshold for minimum change of parameter vector ϵ_2
   - Set maximum number of iteration steps k_{max}
2. Calculate sum of squared error $S(a^k)$ between the estimated envelope F_{est}, and the envelope of the input signal F and the derivative

$$S(a^k) = \left\|F - F_{est}(a^k)\right\|^2 \tag{52}$$

$$\frac{\partial S(a^k)}{\partial a^k} = \frac{\partial \left\|F - F_{est}(a^k)\right\|^2}{\partial a^k} = J(a^k) \tag{53}$$

   where $J(a^k)$ is the Jacobian.

[4]The functional principle of the NLMS and an explanation of why the Levenberg-Marquardt algorithm is used in this work can be found in section (3.2).

3. Minimize the linear least square problem:

$$\left\| \begin{pmatrix} J(a^k) \\ \mu I \end{pmatrix} s^k + \begin{pmatrix} S(a^k) \\ 0 \end{pmatrix} \right\| \Rightarrow min$$

   The result of the minimization s^k is the correction factor.

4. Update:

   - $a^{k+1} = a^k + s^k$
   - $S(a^{k+1}) = S(a^k + s^k)$

5. Calculate criteria for new step size:

$$\rho_\mu = \frac{\left\|S(a^k)\right\|^2 - \left\|S(a^k - s^k)\right\|^2}{\left\|S(a^k)\right\|^2 - \left\|S(a^k) + J(a^k)s^k\right\|^2} \tag{54}$$

   - If $\rho_\mu \leq \beta_0$: s^k is not accepted, μ is doubled and new correction factor s^k is calculated
   - If $\beta_0 < \rho_\mu$: s^k is accepted, μ is retained
   - If $\rho_\mu \geq \beta_1$: s^k is accepted; μ is halved

6. Repeat step 2 to step 4 until:

   - $\left\|S_{a^k}\right\| \leq \epsilon_1$ or
   - $\left\|a^k - a^{k-1}\right\| \leq \epsilon_2(\left\|a^{k-1}\right\| + \epsilon_2)$ or
   - $k \geq k_{max}$

7. When the iteration has stopped, the resulting parameter vector $a = [a_{1n}, a_{2n}, ..., a_{4n}]$ of the estimated envelope F_{est} represents the best fit to the envelope of the input signal.

For a better overview of the functionality of the damage feature extraction process, the entire sequence is listed below.

Input signal:

F	envelope of measured input signal $y(t)$

Initial parameters:

$a^0 = [a_{1n}, a_{2n}, ..., a_{4n}]$;	parameter vector
μ^0;	initial step size
$\beta_0 = 0.25$, $\beta_1 = 0.75$;	criteria for step size (experience values)
ϵ_1;	threshold minimum squared error $\|s\|$
ϵ_2;	threshold minimum change of a^k
k_{max};	maximum number of iterations
$k = 0$	first iteration

Step 1:

$F_{est}(a^k) = Hilbert(y_{est}(a^k))$	calculate envelope of model signal y_{est}
$S(a^k) = \|F - F_{est}(a^k)\|^2$	calculate sum of squared error $S(a^k)$
$\frac{\partial S(a^k)}{\partial a^k} = \frac{\partial \|F - F_{est}(a^k)\|^2}{\partial a^k} = J(a^k)$	calculation of Jacobian J

Step 2:

$\left\| \begin{pmatrix} J(a^k) \\ \mu I \end{pmatrix} s^k + \begin{pmatrix} S(a^k) \\ 0 \end{pmatrix} \right\| \Rightarrow min$	minimize linear least square problem

Step 3: (update)

$a^{k+1} = a^k + s^k$

$S(a^{k+1}) = S(a^k + s^k)$

Step 4:

$\rho_\mu = \frac{\|S(a^k)\|^2 - \|S(a^k - s^k)\|^2}{\|S(a^k)\|^2 - \|S(a^k) + J(a^k)s^k\|^2}$	calculate criteria for new step size
if $\rho_\mu \leq \beta_0$	s^k is not accepted, μ is doubled and new correction factor s^k is calculated
if $\beta_0 < \rho_\mu$	s^k is accepted, μ is retained
if $\rho_\mu \geq \beta_1$	s^k is accepted, μ is halved

Step 5: repeat step 2 to step 4 until:

$\|S_{a^k}\| \leq \epsilon_1$ or

$\|a^k - a^{k-1}\| \leq \epsilon_2(\|a^{k-1}\| + \epsilon_2)$ or

$k \geq k_{max}$

Result: $a^k = [a_{1n}, a_{2n}, ..., a_{4n}]$ estimated parameter vector

3.4 Validation of the Proposed Damage Feature Extraction Procedure

When using Lamb waves for damage detection two main questions must be considered, i.e., how the environmental conditions will influence the measured result and whether it is possible to identify overlapping damage features. If it is possible to identify overlapping features, the ratio of overlapping which can be dealt with must be estimated.

In order to answer these questions, the following validation process was developed for the DFE procedure.

1. Investigation of how environmental effects such as temperature change or synchronization effects will influence the DFE procedure,

2. Testing of the ability and stability of the DFE procedure for overlapping wave packets with varying amplitudes and overlapping ratios.

3.4.1 Investigation of Environmental Effects

Environmental effects such as temperature changes will influence the propagation of the Lamb wave inside a structure, leading to a shift in several wave parameters such as the occurrence time or the amplitudes of the different wave packets. However, even a small difference in the occurrence time of the wave packets within the measured signal $x(t)$ and the estimated signal $x_E(t)$ makes direct comparison impossible. Therefore, in this work the difference produced by environmental effects between the estimation and the measured signal will be compensated for by the introduced adaptive process. In order to test the ability of the proposed adaptive procedure, a synthetic input signal $x(t)$ is used. The test parameters of the synthetic signal are changed slightly in a stepwise manner during the proof, in order to test the stability of the DFE procedure and to estimate the boundaries within which the DFE procedure will provide suitable results. The calculation of the synthetic signal and the parameters used are described and listed in APPENDIX B.

In order to simulate a more realistic scenario, additional Gaussian white noise with an SNR of 40 dB was added to the (synthetic) input signal $x(t)$. The signal

$x(t)$ was applied to the DFE procedure described in section (3.3). The initial parameters $a^0 = [a_1, a_2.., a_n]$ used for the calibration step are listed in Table (2).

3.4.2 Calculation of the Synthetic Signal

The calculation of the synthetic input signal $x(t)$ is based on the equation (48) described in section 3.4. The calculated input signal $x(t)$ consists of:

- Incident wave pulses $E_{A_{0inc}}$ and $E_{S_{0inc}}$
- Reflected wave pulses from an area of damage $E_{A_{0damage}}$ and $E_{S_{0damage}}$

The parameters listed in Table (2) for the calculation are based on measurements performed on a real aluminium plate. In principle, the synthetic signal can be expanded by additional wave pulses such as reflected wave packets from the edges of the structure.

Table 2: Values of the wave parameters for the calculation of the synthetic signal.

Description	Parameter	Values	Dim.
Excitation Frequency	f	100	[kHz]
Propagation distance, actuator-sensor	r_{inc}	200	[mm]
Propagation distance, actuator-damage-sensor	r_{dam}	200 - 400	[mm]
Group velocity	$c_{g_{A0}}$	1120	[m/s]
	$c_{g_{S0}}$	5,300	[m/s]
Amplitude incident wave pulse	$A_{A_{0inc}}$	1	[V]
	$A_{S_{0inc}}$	0.5	[V]
Amplitude reflected damage wave pulse	$A_{A_{0refdam}}$	0.01 - 0.1	[V]
	$A_{S_{0refdam}}$	0.005 - 0.05	[V]
Pulse width	τ_{A0}	0.003	[ms]
	τ_{S0}	0.001	[ms]
Dispersion coefficient	$k''_{0_{A0}}$	1e-4	[-]
	$k''_{0_{S0}}$	0	[-]
Chirping parameter	Ψ_{A0}	1e-8	[-]
	Ψ_{S0}	0	[-]

3.4.3 Validation Without Damage-Related Features

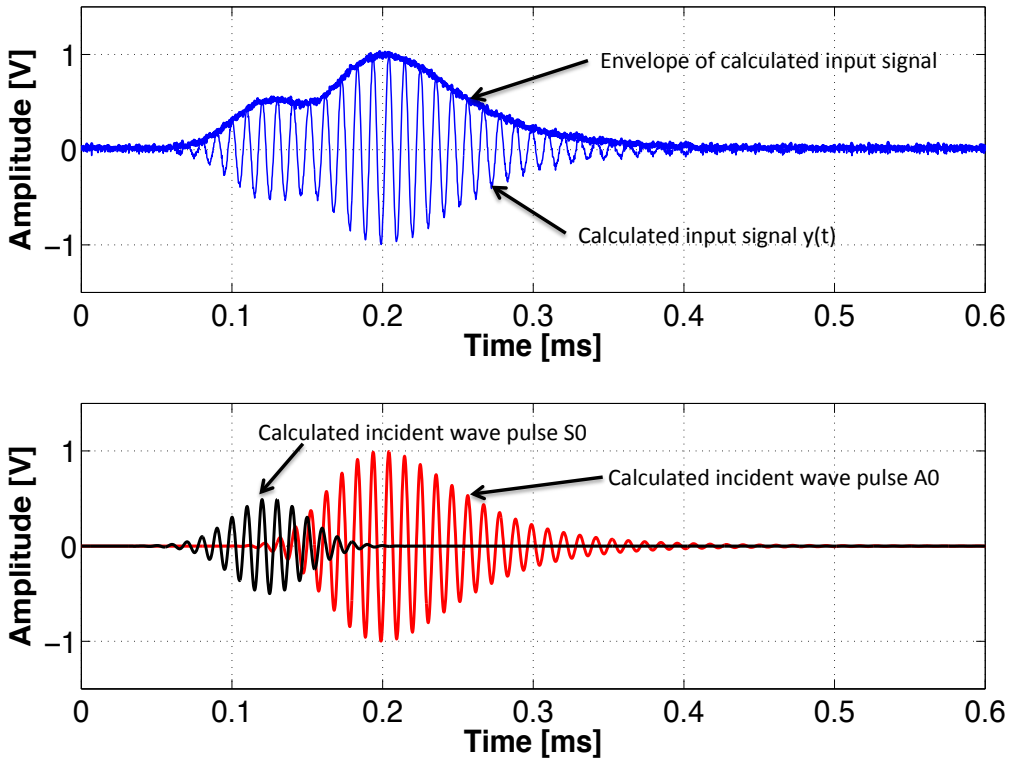

Figure 16: Calculated synthetic signal $x(t)$ without damage-related features used in this experiment. In the top graph, the synthetic signal used for the test is displayed. In the graph below, the incident wave packets (A_0 and S_0) within the calculated signal are displayed.

For the example presented here, only the first incident wave packets E_{S_0inc} and E_{A_0inc} are present in the input signal $x(t)$ (the pristine state of the structure is assumed). The input signal $x(t)$ used in this section is illustrated in the top graph in Fig.(16). As explained above, the parameters of the synthetic signal $x(t)$ were changed stepwise with regard to the relationship between the parameters of $x(t)$ and the initial parameters a_0 of the estimated signal $x_E(t)$. The test started with a

relationship of 0.1, which means that the value of the synthetic signal parameters were smaller than the initial parameters of the estimated signal, and ended with a relationship of 4.0, which means that the values of the synthetic signal were much higher than the initial parameters of the estimated signal. The parameters of the synthetic signal $x(t)$ which were changed during the proof test are listed in Table (3) below. For this proof test it was assumed that only the A_0 incident wave packet is affected by dispersion and chirping.

Table 3: Wave pulse parameters of the synthetic signal $x(t)$ changes during the proof test.

Wave pulse parameter	Description
$A_{A_{0inc}}$	Amplitude of incident A_0 wave pulse
$r_{A_{0inc}}$	Propagation distance of incident A_0 wave pulse
$k''_{0_{A0}}$	Dispersion coefficient of incident A_0 wave pulse
ψ_{A0}	Chirping coefficient of incident A_0 wave pulse
$A_{S0_{inc}}$	Amplitude of incident S_0 wave pulse
$r_{S0_{inc}}$	Propagation distance of incident S_0 wave pulse

The various ratios between the parameters used for the calculation of the synthetic signal $x(t)$ are listed in Table (4).

Table 4: Parameter range for the calculation of the synthetic signal.

$A_{A0_{inc}}/a_{01}$	$r_{A0_{inc}}/a_{02}$	$k''_{0_{A0}}/a_{03}$	ψ_{A0}/a_{04}	$A_{S0_{inc}}/a_{05}$	$r_{S0_{inc}}/a_{06}$
0.1 - 4	0.1 - 4	0.1 - 4	0.1 - 4	0.1 - 4	0.1 - 4

3.4.4 Results for the Investigation of Environmental Effects

The results of this investigation are displayed in the individual plots in Fig.(17). Plot (a) shows the results for the estimation of the envelope of the E_{A0inc} incident wave pulse, plot (b) shows results for the envelope of the E_{S0inc} incident

wave packet and plot (c) shows results for the estimation of the whole simulated signal. For all three plots. the root mean-squared error (RMSE) between the estimated and the calculated signal was plotted against the ratio of the estimated and simulated amplitudes. The RMSE is calculated as:

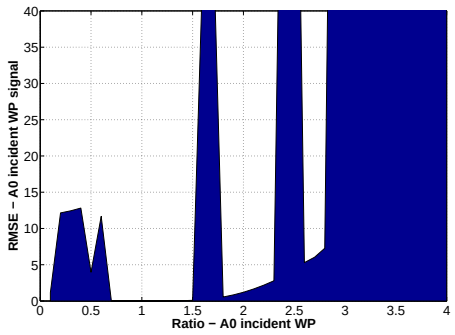

(a) RMSE - A_0 incident wave pulse

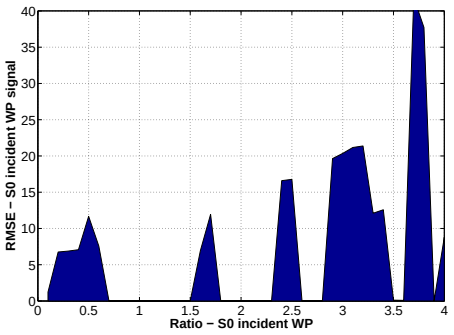

(b) RMSE - S_0 incident wave pulse

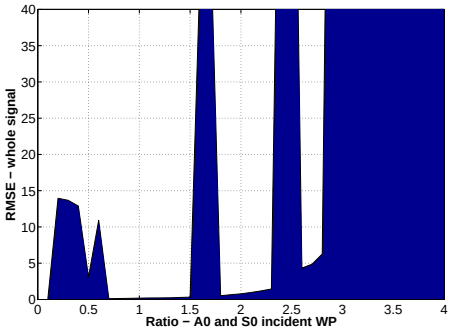

(c) RMSE - whole signal

Figure 17: Root mean-square error (RMSE) between the input and the estimated signal.

$$RMSE = \sqrt{\frac{1}{n}\sum_{i}(F_{est}(n) - F(t))^2} \tag{55}$$

where $F_{est}(n)$ represents the envelope of the estimated signal and $F(t)$ represents the envelope of the calculated signal.

When considering the results of the investigation present in Fig.(17) it becomes obvious that the damage feature extraction algorithm works stable in the range of the ratio between 07 and 1.5. Here, the calculated RMSE is 0. Outside of this region the RMSE changes abrupt to a very high level (>40) and drops back to normal levels, which is illustrated as spikes in the Figures. The reason for the extreme outliers is the phase shift between the two wave signals. For a phase shift of approximately 180° the two wave packets are cancelling each other (destructive interference) and an estimation outside of the stable region (ratio = 0.7 - 1.5) is not possible any more. After the two wave packets are in constructive interference it is again possible to estimate the wave pulse parameters but an increasing of the ratio between the real wave parameters and the initial wave parameters used for the damage feature extraction algorithm the RMSE increases. For a ratio above 2 the damage feature extraction algorithm is not any more able to estimate the real wave parameters.

In summary, after the investigation of the DFE algorithm calibration process it can be stated that:

- The proposed DFE algorithm is able to adjust the wave pulse parameters of the expected wave pulses to the parameters of the wave pulses within the input signal,
- This process works with both stable and noisy input signals,
- The results of the investigation where the algorithm was tested with different input wave signal parameters showed a good correlation between the estimated signal and the measured signal over a range of ratios $\frac{\text{real wave pulse parameters}}{\text{initial wave pulse parameters}}$ between 0.7 and 1.5. Below and above this range the algorithm is not able to estimate the wave parameters with sufficient accuracy.

3.4.5 Validation with Damage-Related Features

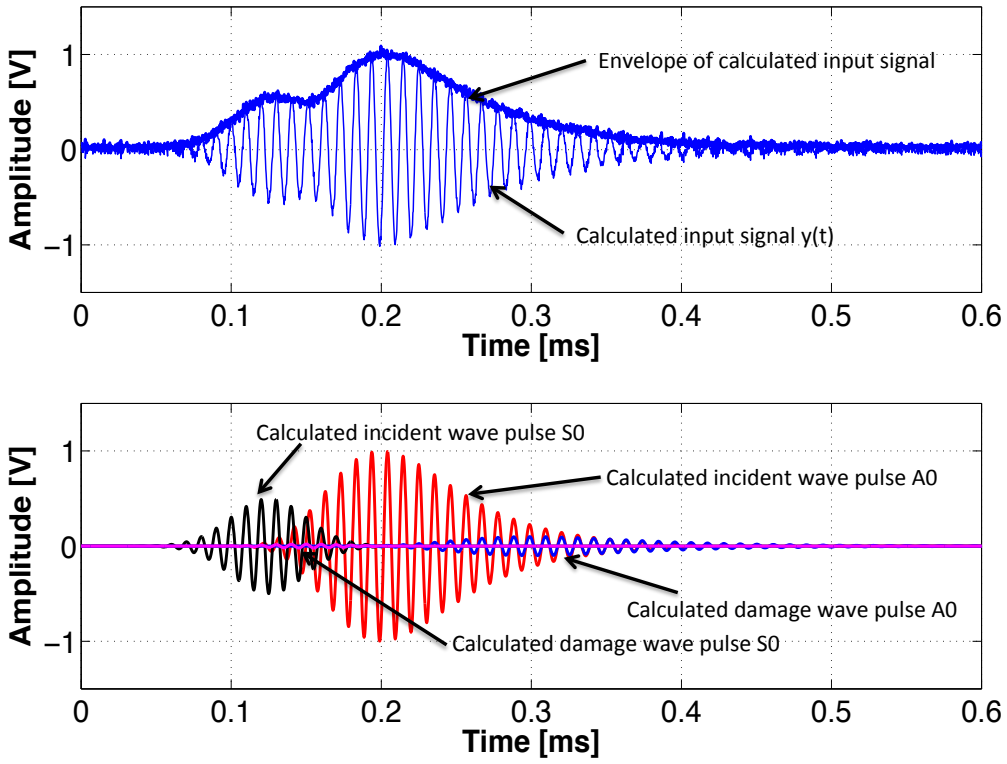

Figure 18: Calculated synthetic signal $x(t)$ with damage-related features used in this experiment. In the top graph, the synthetic signal used for the test is displayed. In the graph below, the incident wave packets (A_0 and S_0) and the reflected wave packets (A_0 and S_0) from the damage within the calculated signal $x(t)$ are displayed.

After the first proof test step described in section 3.4.1, the DFE procedure was tested with damage-related features hidden inside the synthetic signal $x(t)$. Therefore, the input signal $x(t)$ for the DFE procedure was expanded by the addition of two wave packets $E_{A_{0damage}}$ and $E_{S_{0damage}}$ reflected from the damage, as illustrated in Fig.(18) in the lower graph. The parameters used for the calculation of the synthetic signal xt are listed in Table (6). The calculated synthetic signal $x(t)$, its

envelope and the single wave packets integrated into the signal are illustrated in Fig.(18). The upper graph in Fig.(18) shows the entire synthetic signal $x(t)$ with its envelope used for the proof test and the lower graph shows the single wave pulses within the synthetic signal. The initial parameters for the estimated of the signal $x_E(t)$ are listed in Table (5).

Table 5: Initial parameter values a^0 for the DFE procedure.

a_{01}	a_{02}	a_{03}	a_{05}	a_{06}	a_{06}	a_{07}	a_{08}	a_{09}	a_{10}
$A_{A_{0inc}}$	$r_{A_{0inc}}$	$k''_{0_{A0}}$	ψ_{A_0}	$A_{S_{0inc}}$	$r_{S_{0inc}}$	$A_{A_{0dam}}$	$r_{A_{0dam}}$	$A_{S_{0dam}}$	$r_{S_{0dam}}$
1	0.2	1e-4	1e-8	0.5	0.2	0.001	0.01	0.001	0.01

Table 6: Parameters and their values for the calculation of the input signal $x(t)$ with damage.

$A_{A_{0inc}}$	$r_{A_{0inc}}$	$k''_{0_{A0}}$	ψ_{A0}	$A_{S_{0inc}}$	$r_{S_{0inc}}$	$A_{A_{0dam}}$	$r_{A_{0dam}}$	$A_{S_{0dam}}$	$r_{S_{0dam}}$
1	0.2	1e-4	1e-8	0.5	0.2	0.02	0.2	0.01	0.2

For the nonlinear least mean square algorithm, the following settings are used:

- $\mu^0 = 0.01$;
- $\epsilon_1 = 10e^{-3}$;
- $\epsilon_2 = 10e^{-8}$;
- $k_{max} = 100$;

As explained for the first proof test in section (3.4.3), the parameters of the synthetic signal were varied over a certain range. The DEF procedure demonstrated its sufficiency over the same range of parameters as in the first proof test.

3.4.6 Results for Investigation with Damage-Related Features

After the DEF procedure has estimated the minimum error between the input signal $x(t)$ and the estimated signal x_E, the procedure stops, and the parameters of interest are presented as the output. The parameters obtained from the above experiment are displayed in Table (7), and it can be shown that the estimated parameters correlate well with the given parameters for the synthetic signal. As already mentioned, the proof test was carried out for a wider parameter range, and the results were comparable to the results from the test described here in more detail.

Table 7: Resulting values of the parameter vector a^k.

$A_{A_{0inc}}$	$r_{A_{0inc}}$	$A_{S_{0inc}}$	$r_{S_{0inc}}$	$A_{A_{0damage}}$	$r_{A_{0damage}}$	$A_{S_{0damage}}$	$r_{S_{0damage}}$
a_{01}	a_{02}	a_{03}	a_{04}	a_{05}	a_{06}	a_{07}	a_{08}
1	0.2	0.5	0.2	0.001	0.2	0.001	0.2

The obtained output parameters are then used to calculate the graph of the wave packets, as displayed in Fig.(19) below. In this figure, only the reflected wave packets are considered.

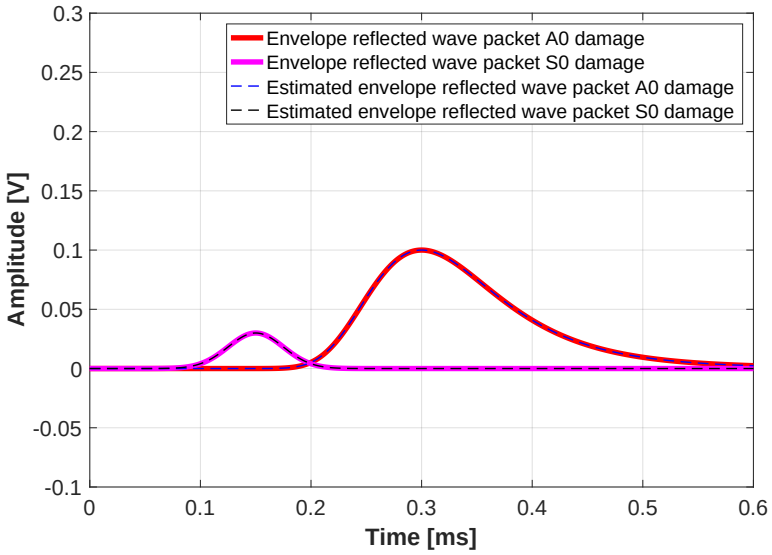

Figure 19: Comparison between the calculated envelope and the estimated envelope of the reflected wave packets (A_0 and S_0) from the damage.

The two solid lines indicate the envelope of the reflected wave packets A_0 (red line) and S_0 (magenta line). The two dashed lines represent the estimated envelopes for both wave packets, identified by the DFE procedure. The resulting parameters for the example described here are listed in Table (7).

3.4.7 Investigation of Overlapping Wave Packets

In order to test the functionality of the DFE procedure for overlapping wave pulses, a test was performed where two wave pulses were overlapped stepwise (see Fig.(20)). The ratio of the overlapping between the two wave pulses was varied between 0% (no overlapping) and 100% (total overlapping). Furthermore, the amplitude ratio between the two pulses was varied between 0.01 (the amplitude of the second pulse is 100 times smaller than the first pulse) and 0.1 (the amplitude of the second pulse is 10 times smaller than the first pulse). The goal of the DFE procedure is to identify wave pulses which are around 10 times smaller than the incident wave packets and which are 100% overlapped by another wave

packet. These are reasonable values for detection of hidden damage features within a measured signal.

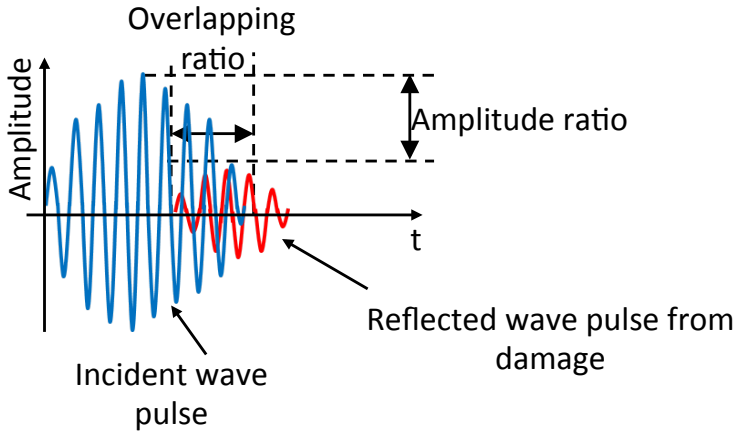

Figure 20: Overlapping wave packets used for the proof test. The wave packet on the left (blue) indicates the incident wave packet with a relatively high amplitude in comparison to the second wave packet (right packet, red) which indicates the reflected wave packet from an area of damage. The overlapping and amplitude ratios between the two wave packets were changed stepwise during the test.

In Fig.(21), the results for a varying amplitude ratio between the incident wave packet and the reflected wave packet from the damage are shown. The interesting damage-related feature in this proof test is the propagation distance r between the actuator, damage and sensor. The results of the proof test are plotted in four graphs, with the difference between the real propagation distance and the estimated distance δr on the y-axis and the overlapping ratio on the x-axis. Graph (a) shows the results for an amplitude ratio of 0.01, graph (b) for a amplitude ratio of 0.03, graph (c) for an amplitude ratio of 0.05 and graph (d) for an amplitude ratio of 0.1. Amplitude ratios lower than 0.01 are meaningless in this investigation because the amplitude of the reflected wave packet would be lower than the amplitude of the signal noise.

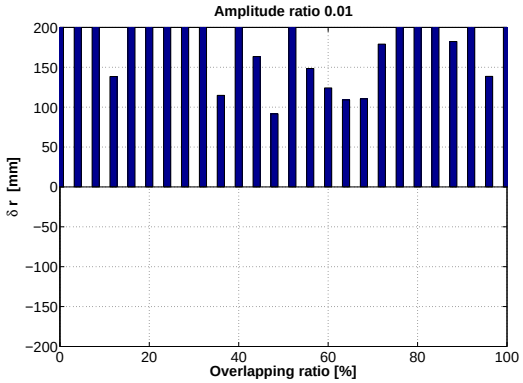

(a) δr for amplitude ratio 0.01

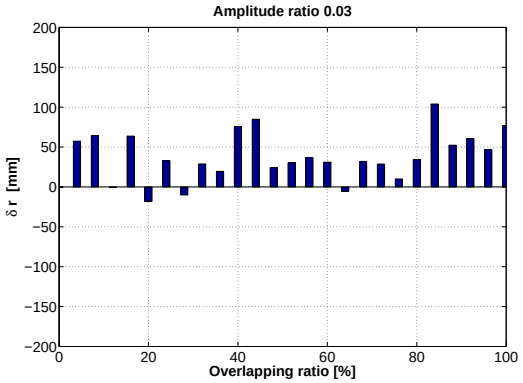

(b) δr for amplitude ratio 0.03

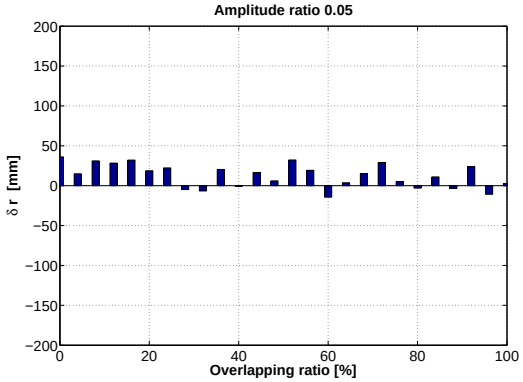

(c) δr for amplitude ratio 0.05

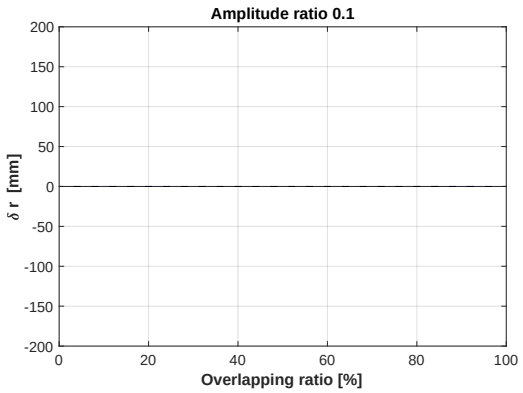

(d) δr for amplitude ratio 0.1

Figure 21: Resulting error δr between the real (known) propagation distance of a wave pulse and the estimated propagation distance. It can be seen that with increasing amplitude ratio between the overlapping wave pulses, the accuracy of the estimation result increases. The overlapping ratio between the wave pulses has no direct effect on the estimation result (see also Fig.20)

3.4.8 Results for the Investigation of Overlapping Wave Packets

From the results of the above study, the following key findings and conclusions can be drawn:

- As assumed in advance, for an amplitude ratio between the incident wave

pulse and the reflected wave pulse of 0.01, the DFE algorithm shows the worst performance ($\delta r > 200mm$), and with increasing amplitude ratio the results of the DFE algorithm show better agreement between the estimated propagation distance and the real propagation distance,

- For higher amplitude ratios, the DFE algorithm enables estimation of the propagation distance of the reflected wave packet with a reasonable difference between the real and the estimated propagation distance. The averaged values of $\bar{\delta r}$ for the different amplitude ratios were:
  - $\bar{\delta r}$ for 0.01 amplitude ratio > 200 mm,
  - $\bar{\delta r}$ for 0.03 amplitude ratio = 31 mm,
  - $\bar{\delta r}$ for 0.05 amplitude ratio = 12 mm,
  - $\bar{\delta r}$ for 0.1 amplitude ratio = 3.5 mm.

3.5 Chapter Summary and Discussion

The interpretation of signals caused by propagating Lamb waves in solid media is complicated due to various circumstances. For example, the Lamb waves propagate dispersively through the structure and may spread out into different wave modes. Furthermore, different wave packets within a measured signal may overlap, which makes the identification of individual wave packets and their arrival times at the sensor complicated. However, in order to use Lamb waves for the identification of damage inside a structure, a completely new signal analysis method has been introduced in this chapter. The signal analysis method is based on static and adaptive mathematical models, summarized as a model-based approach. The advantages of the introduced model-based approach are:

- The possibility of identifying different Lamb wave modes and their arrival times at the sensor even when the individual wave packets are overlapped,
- Independent adjustment of the process to different environmental conditions,
- Autonomous identification of the Lamb wave specific parameters, such as dispersion coefficient and chirping parameter,

- Identification of the arrival times of reflected wave packets from the damage, including where the wave packets are overlapped by the incident wave packets.

For the validation of the damage feature extraction (DFE) procedure, single wave parameters of a calculated synthetic signal were varied within a certain range in order to test the stability of the process for changing measurement signals. It was found that the introduced DFE procedure can be applied over a range within which the wave parameter may change. The validation was restricted to synthetic signals only. From the results of the validation process, the following conclusions may be drawn:

- The DFE procedure enables the estimation of reflected wave packets from damage for the crack sizes specified in the requirement list for the entire system,
- The procedure enables the automatic compensation of environmental effects such as the time shift due to changing temperatures or differences in the measured signal amplitude caused by the measurement system,
- The procedure also enables the estimation of overlapping wave packets and their respective Lamb wave modes.

In principle it would be possible to identify multiple reflected wave packets from different damage areas inside the structure. In this case, the arrival time detection process must be expanded using further approximated analytical equations for the calculation of the wave packets. The NLMS algorithm can then estimate the number of reflected wave packets which are likely to exist in the measured signal and their Lamb wave modes.

4 Model-Based Damage Localization

In this section, the procedure for the localization of the damage on a 2D structure will be introduced. At the beginning of the investigation consisting of practical experiments with Lamb waves on aluminium plates, the trilateration procedure was used for the estimation of the damage position. During these experiments it was found that in certain areas the estimated position did not correlate with the real location of the damage. In order to find the root cause of this deviation, a numerical simulation was carried out. The results highlighted the main drawbacks of the trilateration process and will be described at the beginning of this section.

For this reason, a new method for the localization of damage on 2D structures has been invented in this work, based on a model-based approach in combination with a nonlinear least squares algorithm. The introduction of the new localization method followed by the proof of concept based on a numerical simulation is given in the following subsections.

4.1 The Trilateration Procedure and its Drawbacks

The sensor arrangement directly influences the damage localization process. For example, an unsuitable arrangement can cause lower precision in the estimation of the damage position, or can even make it impossible to estimate the position of the damage. In order to investigate the behaviour of different sensor arrangements in the damage estimation process, a simulation of the process was developed, as presented below.

As previously explained, the trilateration method with intersecting ellipses is used for the estimation of the damage position. One problem with the trilateration method is that, in certain cases, it is not possible to estimate an intersection point between the individual ellipses, and hence it is not possible to identify the position of a possible defect. The reasons may differ; one reason may be possible uncertainties in the determination of the wave propagation distance r. The shape and the size of the damage can also have an impact on the wave propagation distance, as illustrated in Fig.(22). This figure shows how the rays of an impinging

wave pulse are reflected from a circular area of damage.

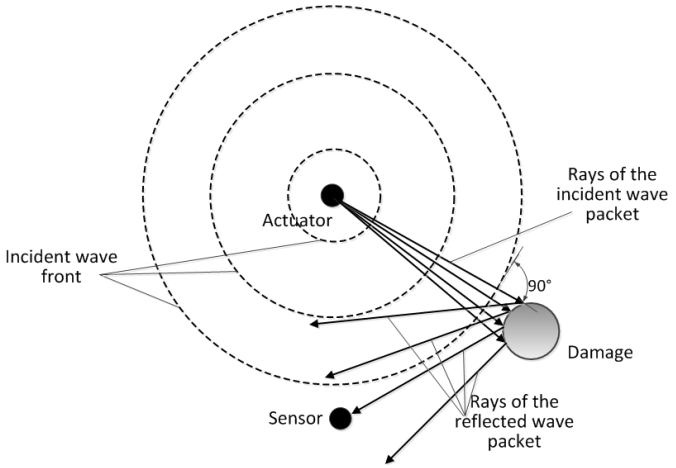

Figure 22: Impinging and reflected wave rays at a circular area of damage.

The effect on the trilateration process of uncertainties in the propagation distance r is illustrated in Fig.(23). Here, the three calculated ellipses do not intersect at a single point, resulting in an intersection area.

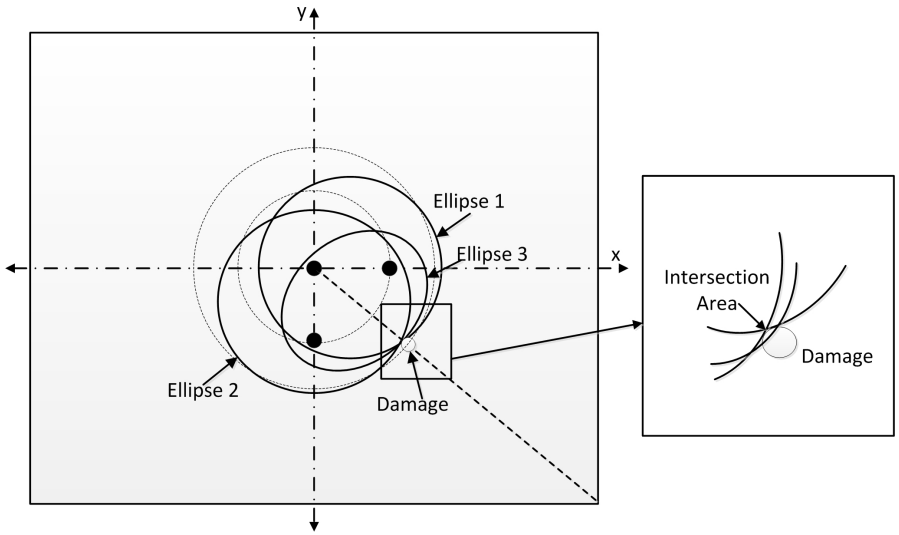

Figure 23: Intersection area due to propagation distance uncertainties.

The arrangement of the piezoelectric transducers as actuators and sensors may

also have an impact on the trilateration process which has not previously been fully understood. To gain a better understanding of the connections and the influences on the trilateration process, a numerical simulation of the trilateration process was carried out. At this point, the simulation was carried out for a symmetric 2D structure, as will be used for the validation of the developed SHM system. For other symmetric structures, the simulation must be adapted to the respective geometrical dimensions. The simulation procedure is illustrated in Fig.(24). First, a two-dimensional structure is covered with a mesh grid where each nodal point represents a possible position of the damage. The piezoelectric transducers are located around the center of the two-dimensional structure, designated here as S_1, S_2 and S_3.

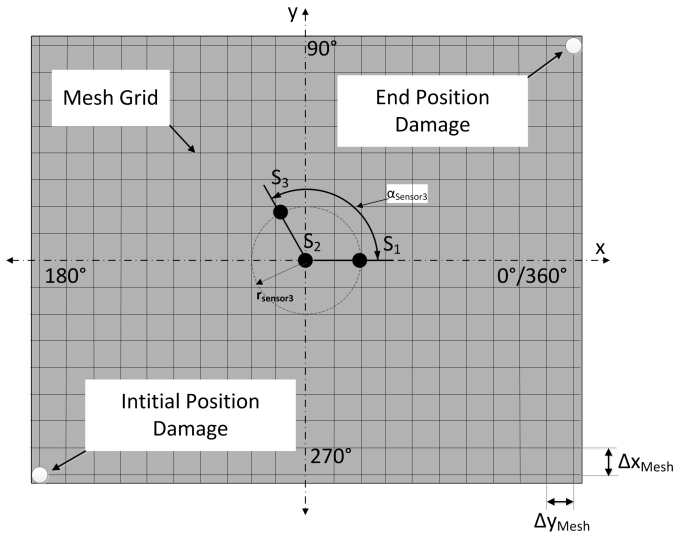

Figure 24: Schematic drawing of 2D structure used for the numerical simulation of the trilateration process.

For the simulation, the position of the damage was varied stepwise, from the initial position to the end position (Fig.(24)). The position of the piezoelectric transducers S_1 and S_2 on the two-dimensional structure was the same throughout the simulation. Only the position of the piezoelectric transducer S_3 was varied, starting from position S_2 in 5-degree increments around the center of the two-

dimensional structure. For each position of the damage and each sensor position, the propagation distances between actuator, damage and sensors r are calculated. This information is used to compute the corresponding ellipses and their intersection point. The propagation distance contains an element of error. The assumed error may be affected, for example, by an uncertainty in the determination of the arrival time of the reflected wave packets from the damage. In addition, the size and shape of the damage was taken into account, as shown in Fig.(22). The respective parameters for the simulation are listed in Table (8).

4.2 Simulation Results and Discussion

The numerical simulation showed that there are basically two different possible arrangements of the sensors, each giving different results for the trilateration process. The difference between the two possible sensor arrangements is the size of the area over which damage can be detected and how precisely the damage can be located. The two sensor arrangements are discussed below.

The first sensor arrangement is more suitable for estimating damage over a relatively large area of the structure. Here, the piezoelectric transducers are arranged linearly. The results from the simulation are shown in Fig.(25) for $\pm 1\%$ uncertainty, and in Fig.(26) for $\pm 3\%$ uncertainty in the estimation of the wave packet propagation distance. The different areas on the structure are divided in ratios, where the area inside Ratio = 1 means, Ratio = distance between sensors / distance away from the middle sensor position. The size of the detectable damage for each ratio area is given as number (e.g. 10 mm^2 for the Ratio = 1 area in Fig.(25)).

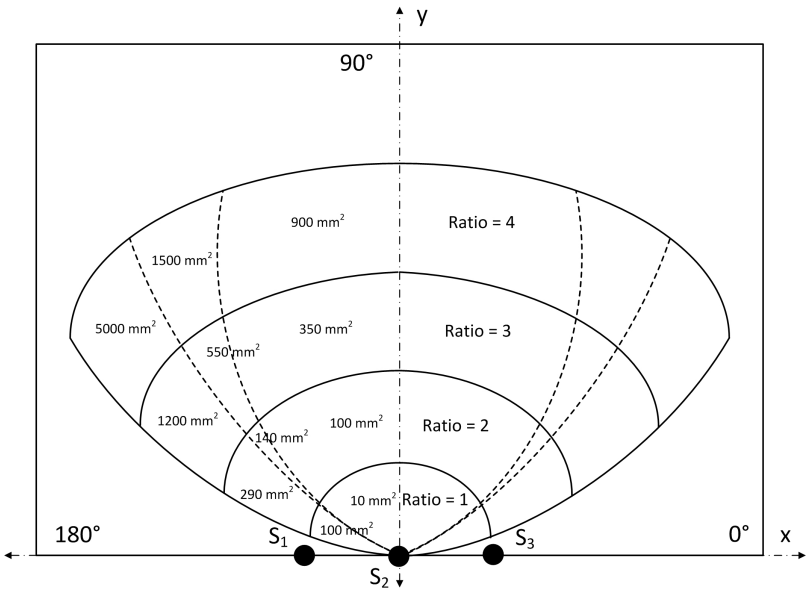

Figure 25: Simulation result for the linear sensor arrangement and ±1% uncertainty.

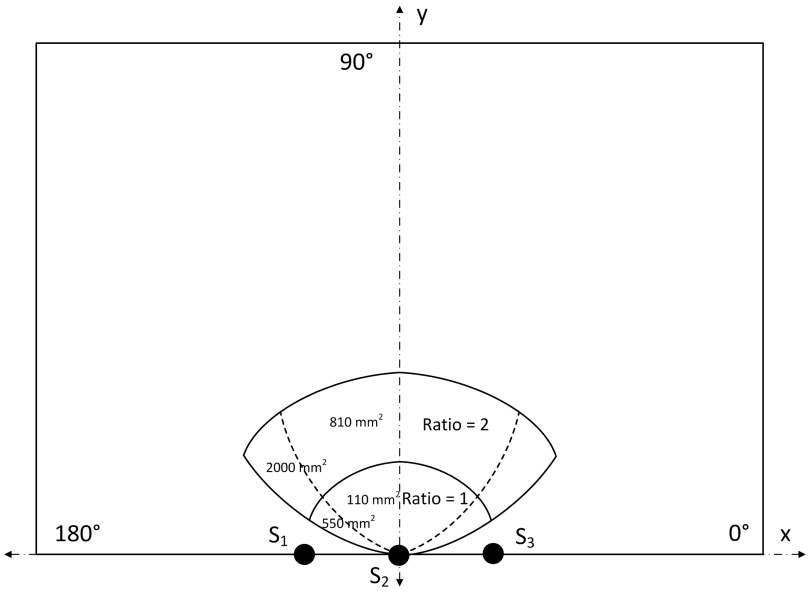

Figure 26: Simulation result for the linear sensor arrangement and ±3% uncertainty.

A linear sensor arrangement is more suited to monitoring a relatively large area on the structure because of the position of the ellipses relative to each other. The individual ellipses have the same shape and differ only in their size. Furthermore, in our specific case, all the ellipses are axisymmetric about the x-axis. This means that the center line for all ellipses is the line of the sensor arrangement. Depending on the location of the damage, the size of each ellipse changes. However, the relative positions of the ellipses remain the same. The angle between the three ellipses at the intersection point is equal for every damage position. Therefore, the ellipses will intersect over a larger area on the structure compared to sensor arrangements where the center lines of the individual ellipses are not the same.

The second sensor arrangement is more suitable for detecting the position of the damage more precisely. The results from the simulation are shown in Fig.(27) for $\pm 1\%$ uncertainty, and in Fig.(28) for $\pm 3\%$ uncertainty in the estimation of the wave packet propagation distance.

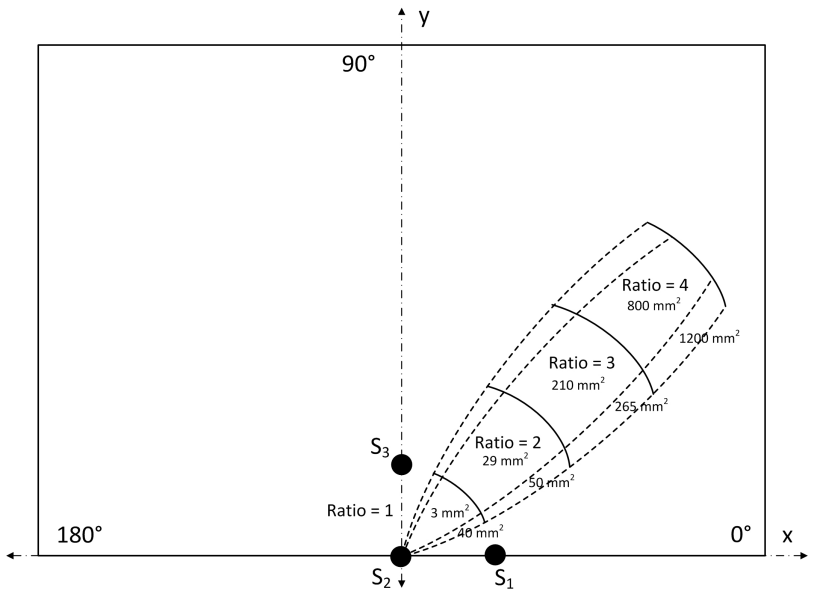

Figure 27: Simulation result for the rectangular sensor arrangement and $\pm 1\%$ uncertainty.

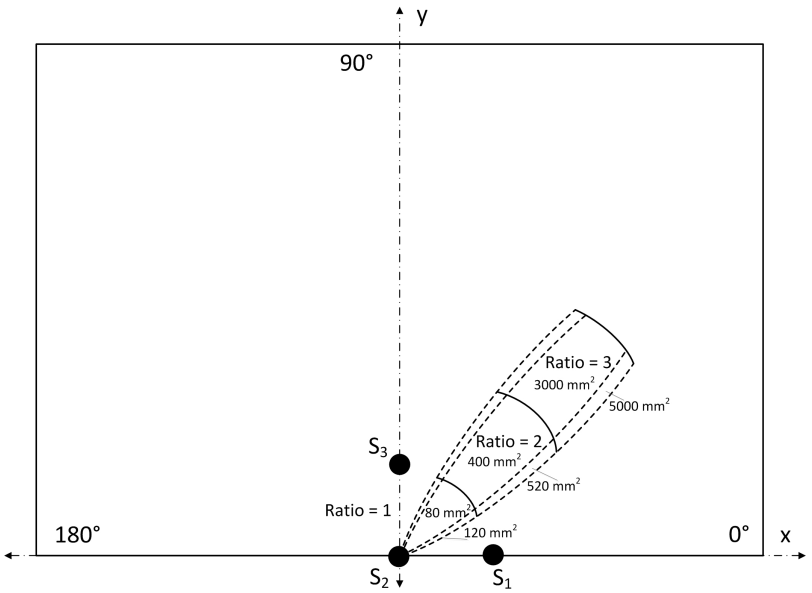

Figure 28: Simulation result for the rectangular sensor arrangement and ±3% uncertainty.

The size of the intersection area for ±1% uncertainty is 3 mm^2, and for ±3% uncertainty the size is 80 mm^2. If one considers a damage area of size approximately 700 mm^2, the intersection area of the ellipses for ±1% uncertainty will be 70 times smaller, and for ±3% uncertainty the area is around seven times smaller. From the two graphs in Fig.(27) and Fig.(28), it can be seen that with increasing angle of the damage away from the the y- axis, the intersection area increases. The smallest intersection area occurs when the damage is approximately at an angle of 45° to the sensor arrangement. Fig.(27) and Fig.(28) show how the size of the intersection area increases when the ratio between sensor arrangement and damage increases. Furthermore, the intersection area is larger when the uncertainty is higher.

The results from the simulation show that different sensor arrangements are suitable for different purposes. In summary:

- The arrangement of sensors on the structure has a direct influence on the possible monitoring region and the accuracy of the estimated position,

- The uncertainties in the distances between actuator, damage and sensor influence the estimated damage position. A higher degree of uncertainty leads to a less precise estimation of the damage position,
- The arrangement of the sensors in the form of a line is best suited to monitoring the largest possible area of the structure,
- The arrangement of the sensors in the form of a right triangle gives the best accuracy if the damage is at an angle of 45° to the sensor arrangement.

In the specification for developing the SHM system, it was required to estimate an 30 mm crack on a two-dimensional structure. The position of the crack should be determined with an accuracy of 50 mm x 50 mm on a 1000 mm x 1000 mm structure. This means that when using the trilateration method with intersecting ellipse lines:

- For ±1% uncertainty, a linear arrangement can be used up to a ratio of 4.0 and approximately ±45° from the center point of the sensor arrangement,
- If a more precise determination of the damage position is needed, the rectangular sensor arrangement as shown in Fig.(27) should be used,
- For an uncertainty of ±3% the linear sensor arrangement is only useful in the near field of the sensors,
- Here, the rectangular sensor arrangement enables the localization of the damage up to a sensor/distance ratio of 3.0, which is equivalent to a distance of 300 mm from the center of the two-dimensional structure.

For relatively small uncertainties, the introduced localization method meets the required specification of the SHM system. For higher uncertainties, the localization method is able to determine the damage position with the specified accuracy only in the near field of the sensor arrangement. This issue limits the applicability of the presented localization method for the specified SHM system. In the section below a second type of trilateration for localization is introduced which enables the damage position to be estimated over a wider range in a two-dimensional structure.

4.3 Improvement of the Damage Position Estimation Using the Model-Based Approach

The process described above for the estimation of the damage position or the area where the damage is located on the structure shows good results in the near field of the sensor arrangement. For the application specified in this work, the accuracy of the damage location by this method might be sufficient. However, the damage localization process has some further disadvantages:

- In order to monitor the specified area on a structure, two different sensor arrangements are needed,
- The possible damage area increases with increasing distance of the damage away from the sensor arrangement,
- In certain cases, the ellipses do not intersect at all because of uncertainties and unfavourable arrangements of the elliptical lines.

In order to eliminate the disadvantages listed above, the trilateration method was expanded using the nonlinear least mean square (NLSM) estimation. The main differences from the conventional trilateration method with ellipse line intersection are:

- Only one type of sensor arrangement is needed for the localization,
- Even with uncertainties in the estimation of the propagating distance it is possible to determine the position of the damage in the specified area on the structure.

In the following, the damage localization method with trilateration and NLMS is introduced. First, the theoretical background is described, together with the functional principle. Subsequently, the validation of the introduced method is demonstrated based on simulated damage positions on a virtual two-dimensional structure. The results of the simulation and the limitations of the presented damage localization are discussed at the end of this section.

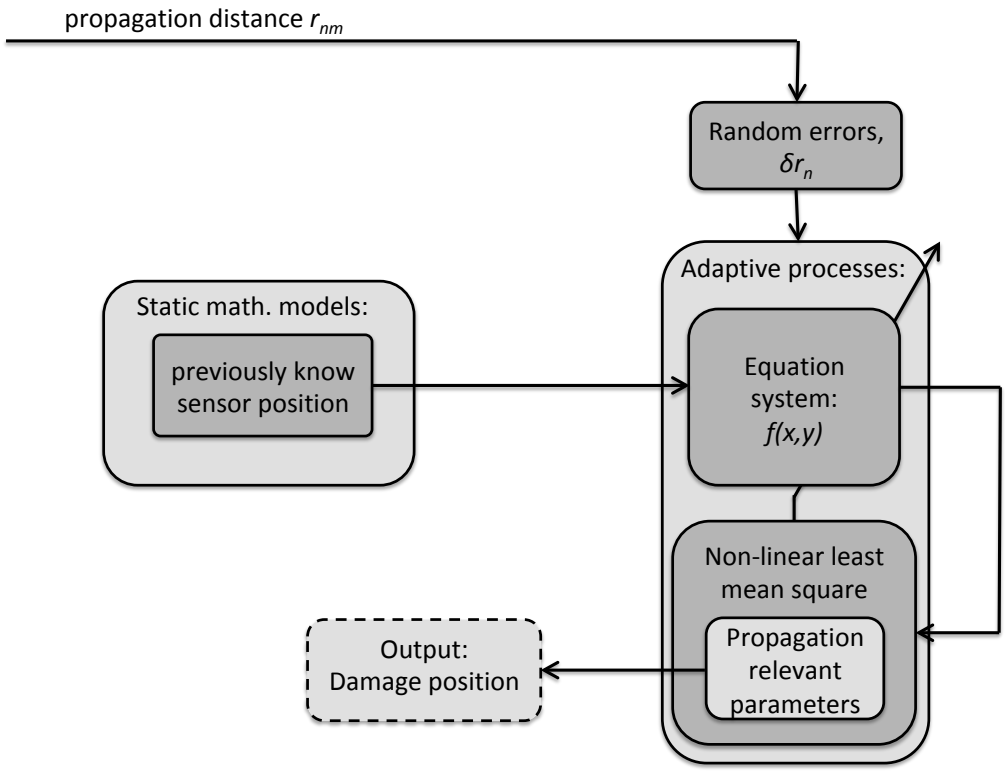

Figure 29: Schematic drawing of the model-based damage localization process introduced in this work. The estimated propagation distance of the reflected wave packets from the damage are the input for the process. The random errors δr_n are the errors caused by the estimation process.

As explained in the section above, information about the propagation time between the actuator, the damage and the sensor can be extracted from the measurements. In this work, this is called the time-of-arrival (TOA). From this information, the propagation distance r can be calculated using information about the propagation group velocity c_g of the wave packets. The propagation distance r can be separated into a forward-propagation path from the actuator to the damage and a back-propagation path from the damage to the sensor. For example, in Fig.(29) the distance between position S_1 and the damage is designated d_1 and the distance between the damage and the sensor S_2 is designated d_2. The entire distance between S_1, damage D and sensor S_2 is calculated as follows.

$$r_{12} = d_1 + d_2. \tag{56}$$

In a 2 dimensional Cartesian coordinate system, this distance can be expressed as

$$r_{12} = \sqrt{(x - x_1)^2 + (y - y_1)^2} + \sqrt{(x - x_2)^2 + (y - y_2)^2} \tag{57}$$

where the unknown damage position D is denoted by (x, y). The following system of nonlinear equations can be derived for all possible propagation distances between the three sensor positions and the damage position.

$$\mathsf{f(x,y)} = \begin{pmatrix} \sqrt{(x - x_1)^2 + (y - y_1)^2} + \sqrt{(x - x_2)^2 + (y - y_2)^2} - r_{12} \\ \sqrt{(x - x_1)^2 + (y - y_1)^2} + \sqrt{(x - x_3)^2 + (y - y_3)^2} - r_{13} \\ \sqrt{(x - x_2)^2 + (y - y_2)^2} + \sqrt{(x - x_3)^2 + (y - y_3)^2} - r_{23} \\ \sqrt{(x - x_2)^2 + (y - y_2)^2} + \sqrt{(x - x_1)^2 + (y - y_1)^2} - r_{21} \\ \sqrt{(x - x_3)^2 + (y - y_3)^2} + \sqrt{(x - x_1)^2 + (y - y_1)^2} - r_{31} \\ \sqrt{(x - x_3)^2 + (y - y_3)^2} + \sqrt{(x - x_2)^2 + (y - y_2)^2} - r_{32} \end{pmatrix} \tag{58}$$

Because of the possibility of using each piezoelectric transducer as a sensor or as an actuator, six propagation distances r are possible. This leads to six nonlinear equations and an overestimated equation system where (x,y) is the unknown damage position. The nonlinear equation system in Eq.(58) can be solved using a nonlinear least mean square approach.

One problem when using the nonlinear least mean square method for position estimation is choosing the initial value for the NLMS algorithm. If the initial value chosen is too far from the real position, the NLMS does not converge to a minimum. Here, the Levenberg-Marquardt NLMS algorithm is able to converge to a minimum even when the initial position is not in the near field of the position estimate. The disadvantage of a longer calculation duration compared to other NLMS algorithms is less important in this work.

For the validation of the improved damage position estimation process, a simulation was developed similar to that for trilateration with ellipses. A mesh grid with

a side length of 100 mm x 100 mm was placed over the simulated two-dimensional structure. Each node of the grid is equivalent to a position for the damage. From the known damage position, first the distances between actuator, damage and sensors r_{12},...,r_{32} are calculated. Subsequently, the expected uncertainties in the estimation of the propagation distance due to the determination of the TOA are added to the propagation distances, leading to the following equation:

$$\mathsf{f}(\mathsf{x},\mathsf{y}) = \begin{pmatrix} \sqrt{(x-x_1)^2+(y-y_1)^2} + \sqrt{(x-x_2)^2+(y-y_2)^2} - r_{12} \pm \delta r \\ \sqrt{(x-x_1)^2+(y-y_1)^2} + \sqrt{(x-x_3)^2+(y-y_3)^2} - r_{13} \pm \delta r \\ \sqrt{(x-x_2)^2+(y-y_2)^2} + \sqrt{(x-x_3)^2+(y-y_3)^2} - r_{23} \pm \delta r \\ \sqrt{(x-x_2)^2+(y-y_2)^2} + \sqrt{(x-x_1)^2+(y-y_1)^2} - r_{21} \pm \delta r \\ \sqrt{(x-x_3)^2+(y-y_3)^2} + \sqrt{(x-x_1)^2+(y-y_1)^2} - r_{31} \pm \delta r \\ \sqrt{(x-x_3)^2+(y-y_3)^2} + \sqrt{(x-x_2)^2+(y-y_2)^2} - r_{32} \pm \delta r \end{pmatrix} \tag{59}$$

where (x, y) is the unknown damage position, (x_n, y_n) is the position of the sensor and δr is the uncertainty due to the propagation distance estimation process. Eq.(59) was implemented in a MATLAB routine where the unknown position (x, y) was calculated by the NLMS.

The entire simulation was repeated for two different sensor arrangements and two different values of the uncertainty. The first sensor arrangement was located around the center of the virtual structure, with each sensor 100 mm away from the center point of the structure as shown in Fig. (30) and Fig. (31(a)). In the second sensor arrangement, the positions of the sensors are at the two lower edges and the upper middle of the structure, as shown in Fig. (30) and Fig. (33(b)). This results in the maximum possible triangular area on the virtual structure. For both sensor arrangements, the simulation was repeated with uncertainties of $\pm 1\%$ and $\pm 3\%$.

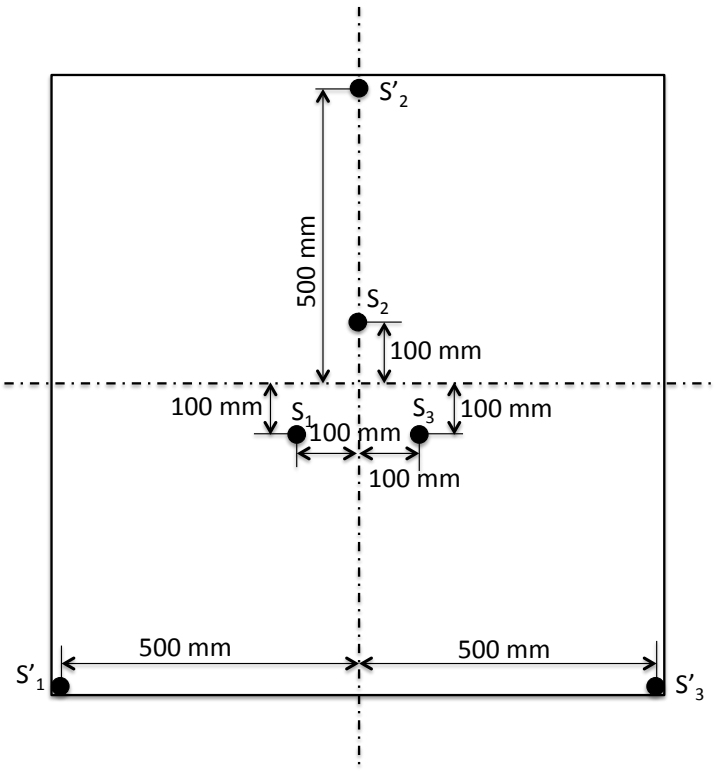

Figure 30: Drawing of the test setup for the evaluation of the NLSM localization process. Two different sensor configurations are tested during the proof test.

Table 8: Parameters for the simulation process.

Description	Parameter	Values	Dimension
Mesh size		100 x 100	[mm]
Mesh number		11x11	
First sensor configuration	S_1	(-100, -100)	[mm]
	S_2	(0, 100)	[mm]
	S_3	(100, -100)	[mm]
Second sensor configuration	S_1'	(-500, -500)	[mm]
	S_2'	(0, 500)	[mm]
	S_3'	(500, -500)	[mm]
Uncertainties	$\pm$ 1%, $\pm$ 3%		
NLMS Levenberg-Marquardt	initial value	$x_0 = 0$, $y_0 = 0$	

The results of the simulations are shown in Fig.(31) for an uncertainty of $\pm 1\%$ with the first sensor configuration and in Fig.(32) for an uncertainty of $\pm 1\%$ for the second sensor configuration. Here, in the sub-figures (a) the virtual two-dimensional structure is shown with the respective sensor positions marked as black circles, the real damage position marked as a blue star and the estimated damage position marked by a red circle. In the sub-figures (b) the respective estimation errors are shown, calculated as follows. The same applies for the results with $\pm 3\%$ uncertainties illustrated in Fig. (33) and (34).

$$\text{Estimation error} = \sqrt{(x_{damage} - x_{estimate})^2 + (y_{damage} - y_{estimate})^2} \tag{60}$$

Here, x_{damage} and y_{damage} give the real position of the damage and $x_{estimate}$ and $y_{estimate}$ give the estimated position of the damage.

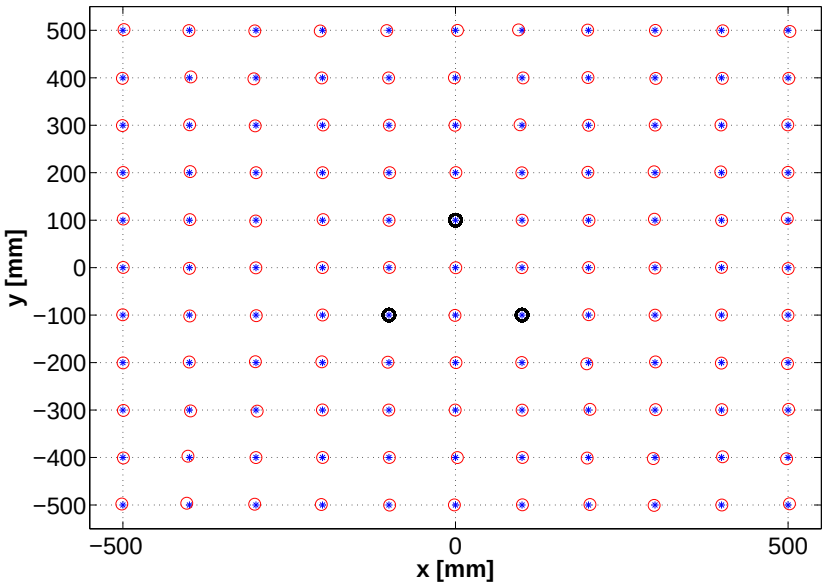

(a) Sensor configuration 1

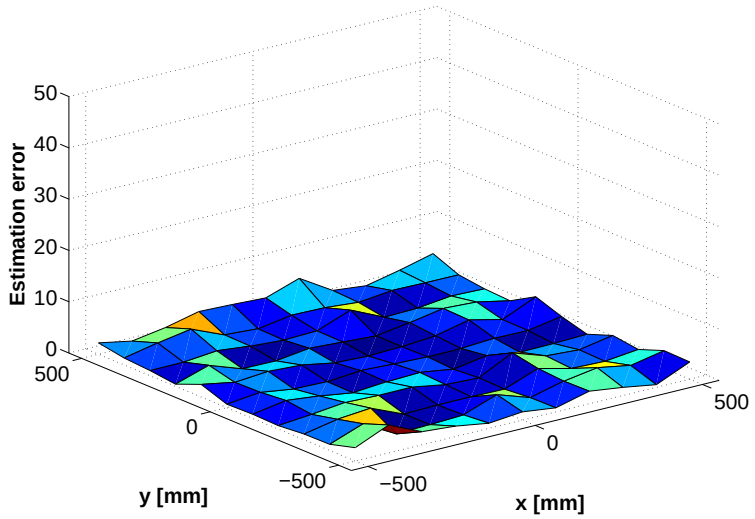

(b) Estimated error, sensor configuration 1

Figure 31: Position estimation with sensor configuration 1 and ±1% uncertainty. Notice: The colours in Figure (b) are used for a better contrast of the illustration and do not correspond with the values in the graph.

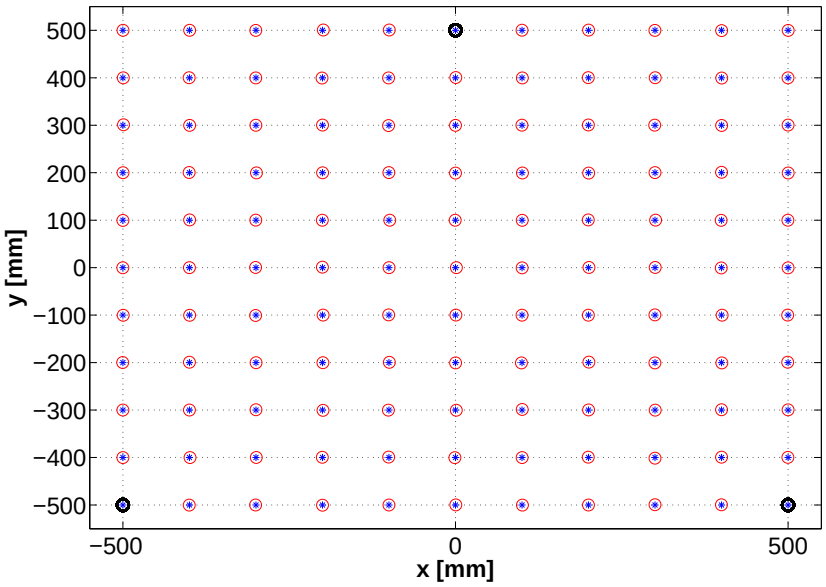

(a) Sensor configuration 2

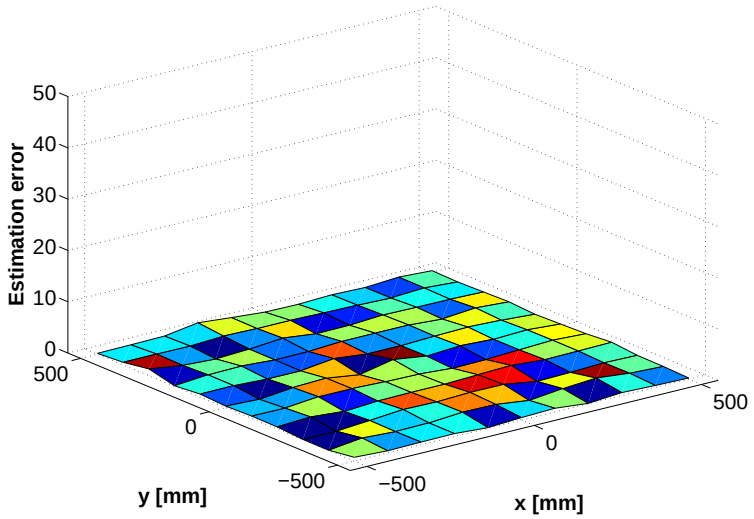

(b) Estimated error, sensor configuration 2

Figure 32: Position estimation with sensor configuration 1 and ±1% uncertainty. Notice: The colours in Figure (b) are used for a better contrast of the illustration and do not correspond with the values in the graph.

The simulation result for the first sensor arrangement shows a relatively good correlation between the simulated and the estimated damage positions in the near field of the sensor arrangement. The average estimation error in this area is approximately 0.3 mm. For damage positions further away from the sensor arrangement, the value of the average estimation error increases to 1.8 mm and the maximum estimation error is 4.6 mm. For the second sensor arrangement, the average estimation error over the entire surface of the virtual structure is 0.2 mm, with a maximum value of 0.5 mm. At the beginning of this work, the allowable error for the estimation of the damage position was specified as 10%-20% of the damage size. Furthermore, the damage required to be estimated was defined as a crack with a length 0.3% of the structures length. For the virtual structure used for the simulation this implies a crack size of 30 mm, leading to an estimation error of 7.0 mm. Thus, the maximum estimation error for both investigated sensor arrangements was below the specified maximum level.

For the simulation with $\pm 3\%$ uncertainty in the determination of the propagation distance r between actuator, damage and sensor, the results for the first sensor arrangement show acceptable correlation between the simulated and the estimated damage position only in the near field of the sensor arrangement, which corresponds to approximately 50% of the entire investigated area (Fig.(33(a)). Here, the average value of the estimation error is 5.2 mm. Further away from the sensor arrangement the average value of the estimation error increases to 8.5 mm with a maximum estimation error of 28 mm on the edges of the structure (Fig.(33(b)). In this area of the structure the value of the estimation error is higher than the specified value of 7.0 mm.

In the results for the second sensor arrangement, the average estimation error over the entire investigation area is 1.3 mm, with a maximum estimation error of 3.1 mm (Fig.(34). Thus, the arrangement of the sensors on the edges of the structure, as illustrated in Fig.(34) is suitable for determining the position of the damage within the entire investigated area with the specified accuracy.

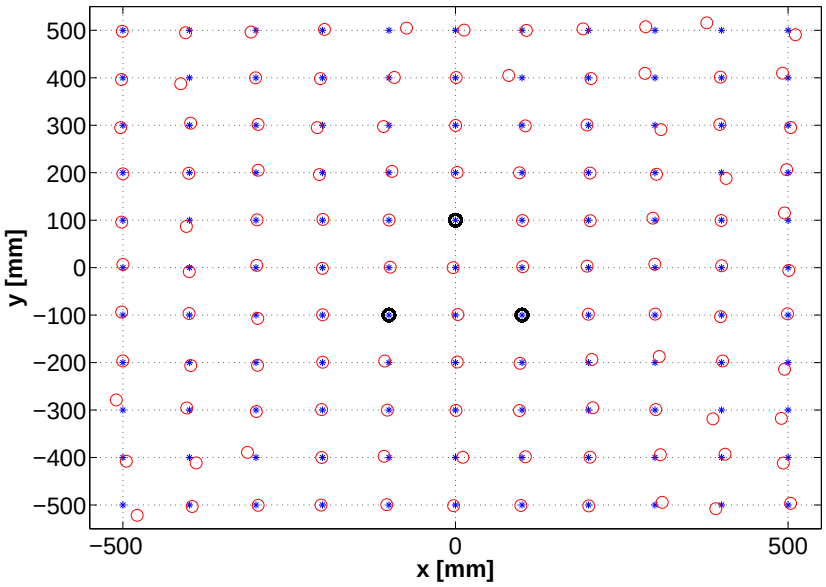

(a) Sensor configuration 1

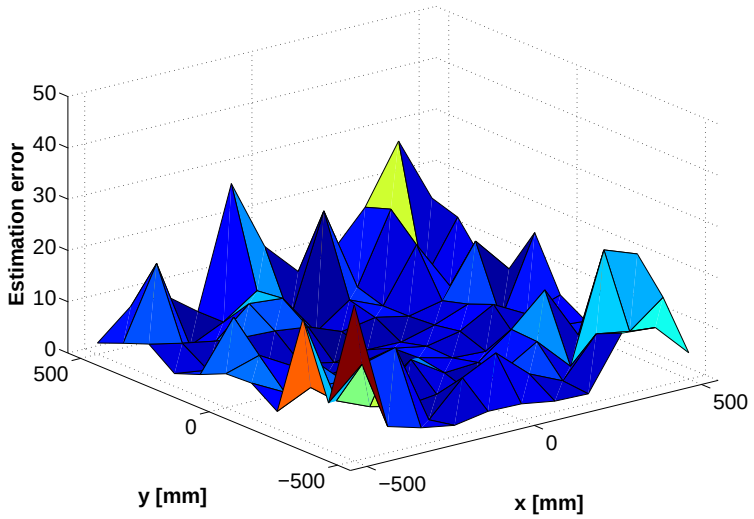

(b) Estimated error, sensor configuration 1

Figure 33: Position estimation with sensor configuration 1 and uncertainty of ±3%. Notice: The colours in Figure (b) are used for a better contrast of the illustration and do not correspond with the values in the graph.

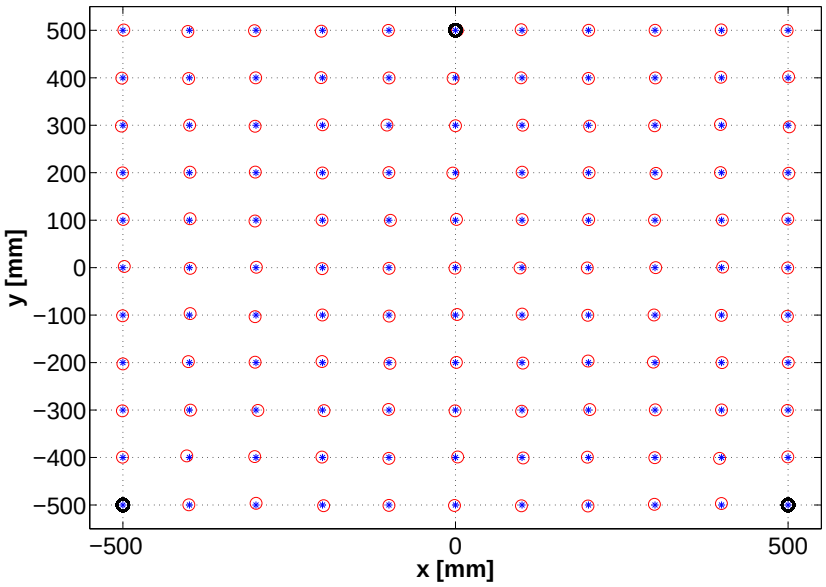

(a) Sensor configuration 2

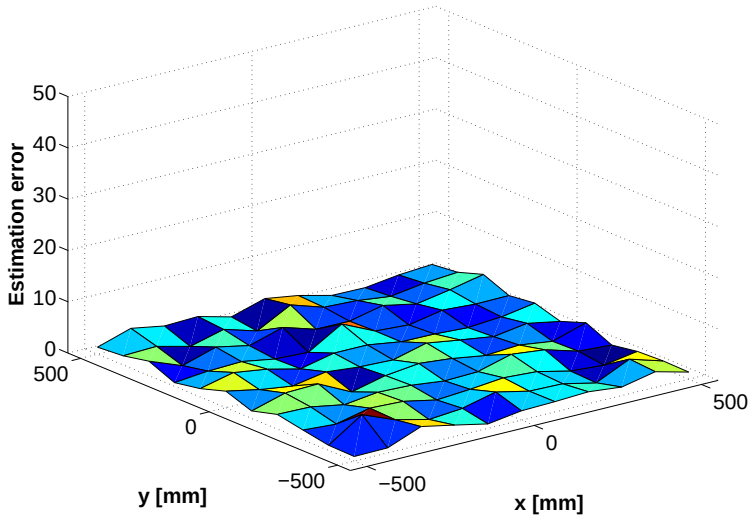

(b) Estimated error, sensor configuration 2

Figure 34: Position estimation with sensor configuration 2 and uncertainty of ±3%. Notice: The colours in Figure (b) are used for a better contrast of the illustration and do not correspond with the values in the graph.

In summary, the following conclusions can be drawn from the investigation of the improved trilateration process.

- The combination of trilateration with nonlinear least mean square determination has advantages over the trilateration method using the intersection of ellipses, such as:
  - Reduction of the sensor numbers
  - Reduction of the damage position estimation error
- The damage position estimation error depends on how the sensors are arranged on the structure
- The sensor arrangement where the damage position is between the sensors shows the lowest estimation error.

It should be mentioned here that the sensor arrangement where the damage is situated between the sensors demonstrated the best performance with respect to damage position estimation. However, it should be clarified whether this sensor arrangement is applicable in practice. For example, it should be investigated whether the sensor position close to the edges of the structure leads to undesirable reflections of the incident wave packets.

5 Structural-Health Monitoring System Implementation

5.1 Aircraft Fuselage Skin Panel

As discussed in the introduction, one possible application for the introduced SHM system is the monitoring of an aircraft fuselage skin. Cracks starting from the fastener hole edges represent one type of possible and critical damage to the aircraft fuselage skin. Due to the fact that the aircraft cabin is pressurized, the skin panel is exposed to mechanical stress during each flight cycle, which can lead to crack propagation starting from the fastener hole. This situation in itself does not represent a major risk because the structure was developed to withstand certain cracks with a defined crack length. However, if the crack reaches a critical length and a second crack propagates from an adjacent fastener hole, the situation becomes more serious. In Fig.(35), an example of a collapsed aircraft skin panel is shown. The initial crack started from a single fastener hole, and after several years of in-service operation of the aircraft the crack reached a critical length, connecting several fastener holes, which can lead to the collapse of the structure within a fraction of a second.

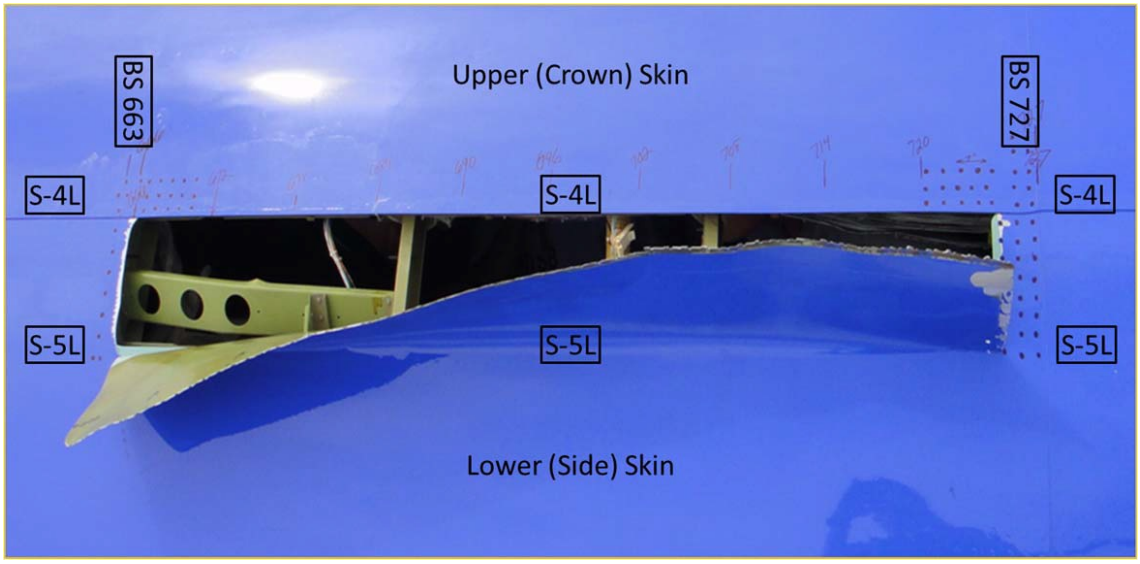

Figure 35: Example of a collapsed skin panel of an aircraft affected by the propagation of a crack between several fastener holes (source: www.arhiva.dalje.com).

After the affected skin panel section was removed for further investigation (Fig.(36)), it was estimated that the crack had propagated between several fastener holes of the lap joint. The initial crack started from a single fastener hole. The reason for the initial crack was incorrect assembly of the fasteners during the production of the aircraft.

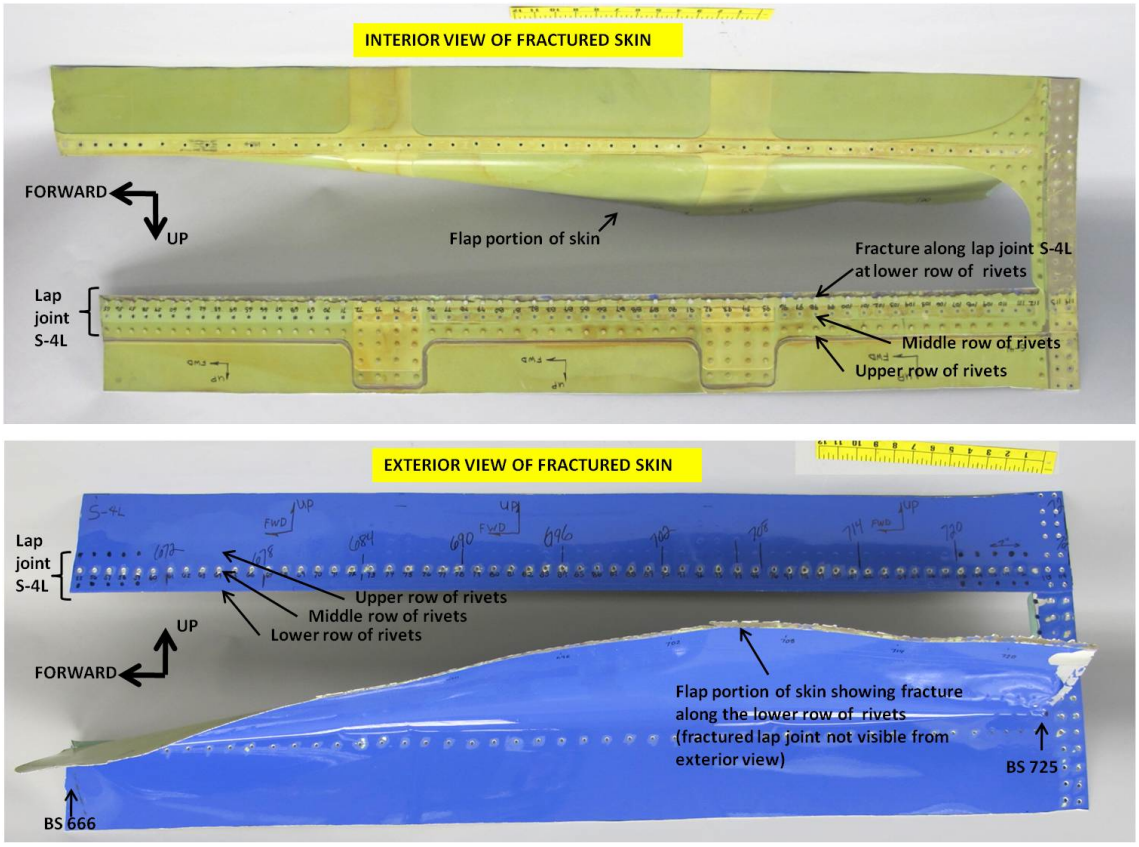

Figure 36: The same skin panel as shown in Fig.(35) but with the skin panel removed from the aircraft for further investigation. It can clearly be seen that the skin panel was separated at lap joint S-4L and the loose section of the panel was pushed outwards (source: www.alchetron.com).

Of course, the damage type illustrated above is a fault which very seldom occurs and only a few cases of a similar magnitude are known. This is because of the compulsory inspection of such areas on aircraft by applying non-destructive testing methods such as eddy-current inspection. Unfortunately, this kind of inspection is very time-consuming given that the structure must be scanned by a single hand-operated eddy-current probe. A more efficient inspection method would be to scan the area of interest (in the above example the lap joint area), from a single point. The Lamb wave inspection technique is appropriate for inspecting large areas on thin plate-like structures by applying sensors at only a few positions on

the structure.

The theory of Lamb wave propagation and the method of extracting the damage features from the measured signal is described in detail in the preceding chapters. In this chapter, the application of a Lamb wave-based inspection technique in combination with a complete SHM system is explained. The SHM system consists of:

1. Piezoelectric transducers as sensors,
2. Wireless measurement system,
3. Damage feature extraction algorithm,
4. Damage localization algorithm.

Apart from the piezoelectric transducers, all parts of the SHM system were developed in the framework of this thesis.

5.2 Specification of Structural-Health System Developed in this Thesis

This chapter includes two main aspects. First, an SHM system was developed relating as closely as possible to a specific application. For this reason, a discussion was conducted with an airline and an aircraft maintenance facility. The discussion results are listed in the requirement catalogue shown in Table (9). The second aspect was to describe the development of the different components for the SHM system accurately, demonstrate their limits and identify other possible applications.

The first questions to answer are related to the specific structure observed. In this case, the aluminium alloy planking of the aircraft structure was selected for the application of the SHM system because the planking forms a high proportion of the aircraft structure and is important for the integrity of the whole aircraft. However, because it represents a high percentage of the aircraft structure, it must be relatively lightweight, and this is achieved by keeping the planking as thin as

possible. One problem that occurs on the planking is that of small cracks starting from rivet holes (see example of real damage in the preceding chapter). The holes are needed for the connection between the supporting ribs and the planking. These small cracks can occur as the age of the aircraft increases (Fig.(37)).

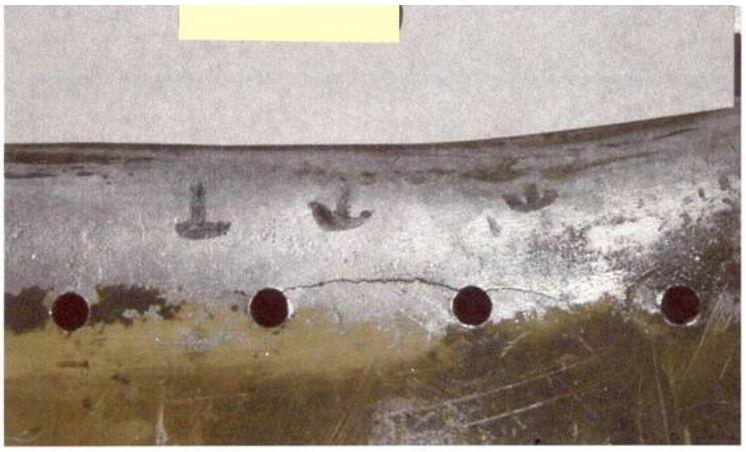

Figure 37: Example of damage. Multiple cracks beginning at the holes for the rivets (source: FAA (U.S. Department of Transportation)).

When the cracks reach a certain length, that part of the structure must be replaced. This ensures that there is no sudden collapse of the structure. The crack length is monitored by non-destructive testing at the usual inspection intervals (C check: every 2,000 flight hours). These fatigue cracks can be observed on the horizontal tailplane planking. Based on the identified critical area, a list of requirements was created for the SHM system, as shown in Table (9).

Table 9: Requirements for the SHM system (in this work).

Level of SHM integrity:	Level 2 (estimation of damage position)
Application requirements:	Subsequent and permanent installation
Operability:	- Application by NDE-trained personnel
	- Independent recognition of damage areas and their positions
	- Real-time evaluation of measurement results
Monitoring area dimension:	Approximately 1 m x 1 m
	thickness 1 mm
Operation conditions	System should work under workshop conditions
Structure specification:	- Plate-like structure
	- Assumed to be quasi-isotropic
Total mass of SHM system (only integrated parts)	Approximately 2%-5% of monitored structure mass
Damage to be detected:	- Fatigue cracks
	- Approximately 0.3 % of monitored structure size
	- Accuracy of 10%-20% of defect size
Sensors	- Permanently installed
	- No influence on structure integrity
Data collection unit	- Self-powered
	- Flexible to install
	- No influence on the aircraft avionics

In order to integrate the SHM system as part of an aircraft, an aviation certification for the system must first be issued. An aviation authorization is not planned as part of this work. The effort would be beyond both the financial resources and the time frame, and could only reasonably be undertaken by the aircraft manufacturer.

In Fig.(38) the various components of the SHM system are illustrated together with the specimen structure for the validation test. The components are: (1) the

specimen structure, (2) the sensors/actuators and their arrangement, (3) three wireless sensor nodes and (4) the central server with graphical user interface and embedded signal processing.

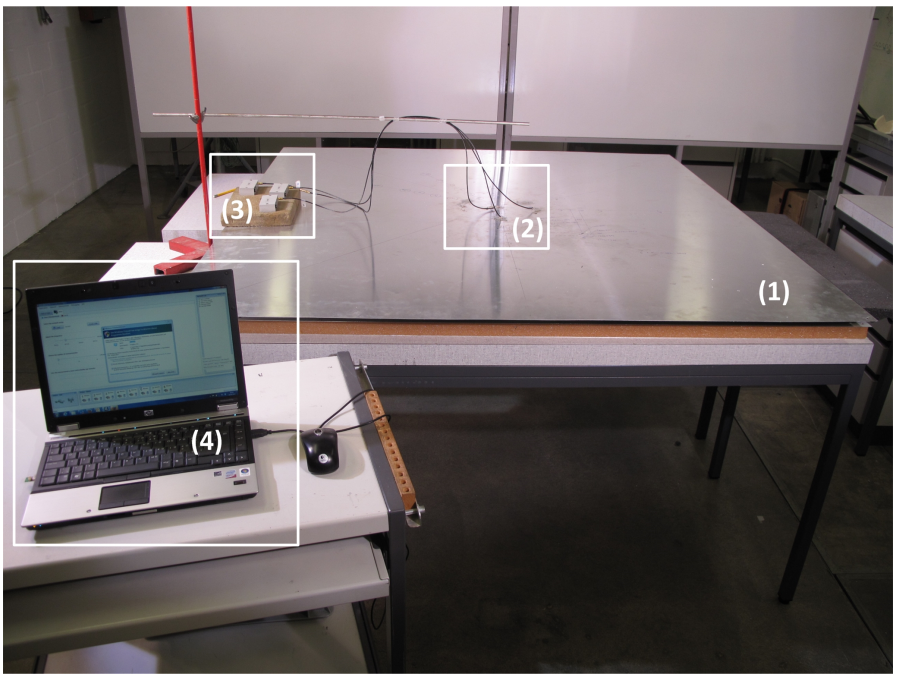

Figure 38: Photograph of the experimental setup. The various components are: (1) aluminium alloy plate, (2) piezoelectric transducers fix bonded onto the plate, (3) wireless measurement devices and (4) central processing unit with wireless receiver, operation software, damage feature extraction algorithm and damage localization algorithm. Note: The connection between wireless notes and piezoelectric transducers are made by using wires.

In the following section, the various parts of the SHM system are explained, and at the end of this chapter the evaluation test for the entire SHM system is explained and discussed.

5.3 Wireless Measurement System

One aspect which is sometimes neglected in the development phase of a monitoring system is the question of how the data from the sensors are processed and transmitted on to the evaluation unit. For example, most of the commercially

available data acquisition systems designed for permanent installation or for short-term tests employ cables to transmit sensor data to a central server. However, the use of cables has disadvantages, especially when a monitoring system is mainly intended for applications in difficult-to-access areas. Examples of disadvantages are the additional weight, or the possibility of short cuts or line interruptions[77]. Furthermore, the capacitances of the cables, especially if they are relatively long, can influence the measured data.

One way to avoid the disadvantages of cables is the use of wireless systems, where the measurement data are transmitted via radio to a processing unit outside the structure. In the last 10 years, a number of wireless SHM systems have been developed for research purposes. Commercial wireless systems are becoming available. Lynch and Kenneth [78] provided a detailed summary of wireless SHM systems for the period 1998 to 2005. The majority of the wireless sensors described in their paper were developed for applications on civil structures. D*ü*rager et al. [79] listed wireless systems which were developed especially for monitoring applications where piezoelectric transducers are used.

In the framework of this thesis, a wireless system was developed for applications where Lamb waves are used in combination with piezoelectric transducers. Compared with existing wireless systems for similar applications, this system offers numerous advantages, such as relatively small dimensions, lightness, high amplitude of excitation voltage, embedded anti-noise filtering and optimized time synchronization between the central server and the wireless sensor units. Furthermore, a graphical user interface enables convenient use of the wireless system. The development process, the main technical specifications and the validation process of the wireless system are explained in [79] and summarized here. The main technical specifications for a single wireless node are listed in Table (10).

The wireless system described in [79] and used in this study consists of a central server and a number of wireless signal processing units (SPUs). An illustration of the whole wireless system and its components is given in Fig.(39). A commercially available personal computer was used as the central server.

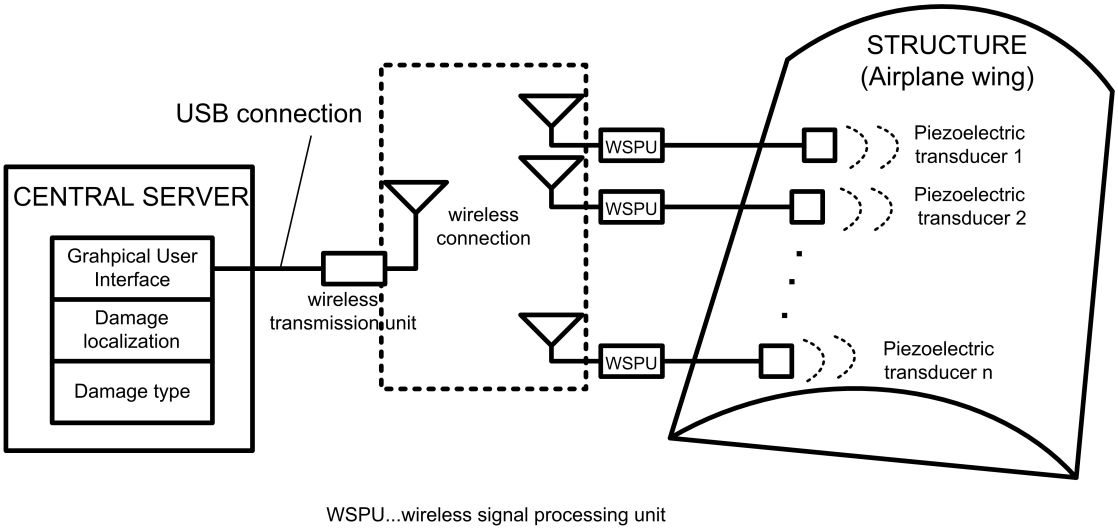

Figure 39: Illustration of the wireless system used in this work for data acquisition, consisting of: (1) piezoelectric transducers, (2) mechanical waves, (3) wireless signal processing units and (4) central server with embedded damage detection process.

The wireless SPU used in this study offers the possibility of exciting a piezoelectric transducer and measuring its voltage signal. The dimensions of the single wireless SPU were 85 mm x 40 mm x 10 mm including the plastic protective container. The total weight of a single SPU including the embedded battery is 30 g. The main electronic parts of the SPU are the microprocessor, the analog-to-digital and digital-to-analog converters, the wireless interface for the connection to the central server and the adaptive filters for smoothing of the measured signal and the excitation. The various electronic components are connected via a peripheral interface. The electric circuit diagram of a single SPU with the various electronic parts is shown in Fig.(40). It has to be mentioned here that the connection between the single SPU and the piezoelectric transducer is made by sûsinf wires. In order to keep the wire length short the SPU's should be placed as near as possible to the piezoelectric transducers.

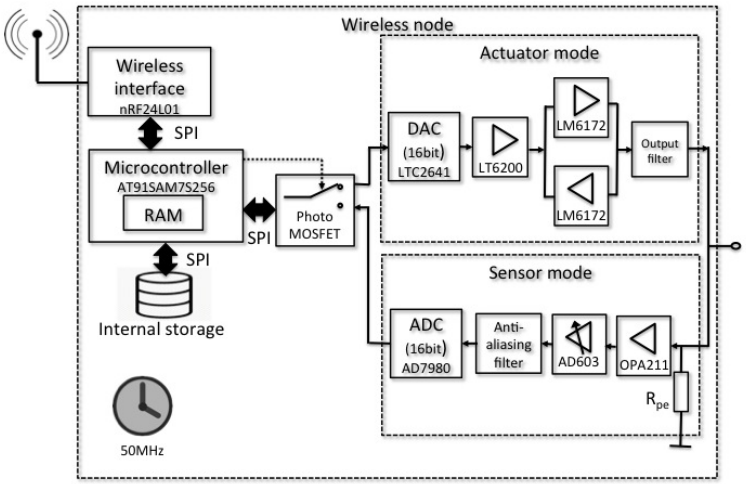

Figure 40: Electric circuit diagram of a wireless sensor node.

The excitation signal for the piezoelectric transducer is a sine sweep with 18 cycles, modulated with a Hamming window with an amplitude of 60V peak-to-peak. The excitation frequency can be selected on the central server in a range from 30 kHz to 300 kHz with a step size of 1 kHz. Zhao et al. [80] used a special tone-burst pulser to obtain an output voltage of 70 V peak-to-peak. However, their concept required wireless power transmission with a special rectangle array design. In contrast to the work of Zhao et al., the wireless system presented here employs a concept with two amplifiers, one as inverter, one non-inverting, and a lower input voltage for the amplifiers is required. Therefore, the output voltage of the integrated battery is sufficient for the direct supply of the amplifiers and no additional voltage supply is needed.

In order to measure the voltage from the piezoelectric transducers, the voltage drop over an internal resistor R_{pe} (Fig. 40) is measured. This leads to a relatively high input impedance for the wireless SPU (in comparison with the internal resistor); a problem which is solved by using a non-inverting amplifier at the input. For a smooth signal, an anti-aliasing filter is integrated into the circuit just before the analog-to-digital converter (ADC). The ADC has a 16-bit resolution with a

sampling frequency of 1 MHz. This leads to a signal-to-noise ratio (SNR) of about 87 dB. By taking into account the Nyquist sampling theorem, (sampling frequency $>$ 2 x signal frequency) a sampling frequency of about 1 MHz is (more or less) enough for a signal frequency up to 300 kHz [20].

One of the main challenges for a wireless sensor network for SHM applications is the time synchronization between the different wireless SPUs in the network [81]. For applications using elastic wave propagation, the time synchronization between the different components at different locations in the network is of prime importance [82]. For the wireless system used here, the time synchronization process between the central server and each individual wireless sensor node in the network works as follows. When the operator starts a measurement on the central server, a time synchronization impulse is produced. This impulse propagates through the air and will be received from every wireless sensor node at nearly the same time. Here, the only time delay between the different wireless sensor nodes is due to the different propagation distances for the signal through the air. For example, for the maximum possible transmission distance of 100 m, the time delay can be calculated as follows:

$$\triangle t_{Air}(\triangle s = 100m) = \frac{\triangle s}{c} = \frac{100m}{299,729km/s} = 33ns \tag{61}$$

where c is the speed of light through the air. The synchronization impulse is now received by the wireless interface at each individual wireless sensor node. The wireless interface transmits an interrupt impulse to the embedded microcontroller. The time delay for receiving the synchronization signal is given by the hardware of the wireless interface, with a maximum time delay (from the data sheet) of about $\triangle t_{interface} = 500$ ns. The wake-up process for the embedded microcontroller requires a maximum time of $\triangle t_{\mu C} = 18$ ns. The maximum time delay from the start of the synchronization process to the actual function on the current wireless sensor node is therefore as shown below. $\triangle t_{Air} + \triangle t_{interface} + \triangle t_{\mu C} = 851$ ns. This estimated time delay was verified during the validation test.

When the measurement data stored on each individual wireless sensor node

are transmitted wirelessly to the central server, the central server first sends a request signal, and each wireless sensor node transmits the stored measurement data wirelessly to the central server. The measurement data are organized into data packets with a length of 32 bytes. As the whole payload length is used, it is possible to achieve a transmission rate of 41.66 kBit/s. One drawback of wireless data communications in networks is the possibility of losing data during the wireless transmission. For the data transmission in the wireless system developed here, the so-called end-to-end recovery process is used [83].

In the framework of this project, the possibility of using the vibration energy of the structure for recharging the embedded battery was also explored. The development process and the validation of the energy-recovery system is described in [84]. It has been shown that the piezoelectric transducers, in this case active fibre composites, are not sufficient for completely recharging the batteries. However, for simpler sensor nodes with a lower energy consumption, the presented process could be quite useful.

Table 10: Technical specification of a single wireless sensor node.

Description	Value
Maximum output voltage	60 Vpp
Maximum sampling rate	1 MHz
Maximum resolution	16 bit
Signal-to-noise ratio	85 dB
Maximum transmission range (outdoor)	100 m
Power requirements	1,399 mW (active mode) 50 mW (inactive mode)
Dimensions	85 mm x 40 mm 10 mm
Weight	30 g

In summary, it can be shown that the wireless system used is very suitable for

research purposes. The system provides a number of innovations that offer benefits to the application in the field of damage detection, (e.g., flexibility of application, intuitive use and use of relatively small and lightweight components). For use in professional applications such as the monitoring of aircraft components, however, the system must be optimized for the specific application. Then, both the size and the energy consumption of the system could be reduced to a required level. Furthermore, the developed wireless system could also be used for these types of applications assuming it meets the conditions for approval for integration.

5.4 Example of Application and Practical Assessment of the System

In this chapter, the validation experiments for the developed SHM system are presented. All experiments were carried out on a specimen structure with material properties close to the structure of interest specified for the application on aircraft structures (Table (9)). All experiments were performed under laboratory conditions.

5.4.1 Experimental Setup

An aluminium alloy plate (5005-H14) with 1 mm thickness and a size of 1.5 m x 1.5 m was used as a specimen structure. The properties listed in Table (11) were used for comparing the material properties of the specimen and the specified structure. Here, the material properties of both plates were roughly comparable. For the experiments, the aluminium plate was supported at its lower surface by a hard foam plate.

Table 11: Material properties of aluminium alloy 5005-H14 and aluminium alloy 6013-T3.

	5005-H14	6013-T3
Modulus, E:	50 GPa	31 GPa
Poisson's ratio:	-0.33	n.a.
Density, ρ:	2.700 g/m^3	2.7100 g/m^3
Yield stress, Y:	500 MPa	379 MPa

The SHM system was tested using two different types of damage. The first type was more artificial, i.e., the damage was simulated using two circular permanent magnets, one mounted on the upper surface and the other mounted opposite the first on the bottom surface of the specimen structure (Fig.(41)).The advantage of the use of permanent magnets is that they can be removed from the surface. The diameters of the circular magnets were 30 mm. For the second type of damage, a slot was milled through the aluminium plate. Unfortunately, this type of damage is not reversible. Therefore, the experiment with the milled slot was the last experiment carried out (Fig.(42)). The length of the slot was 30 mm.

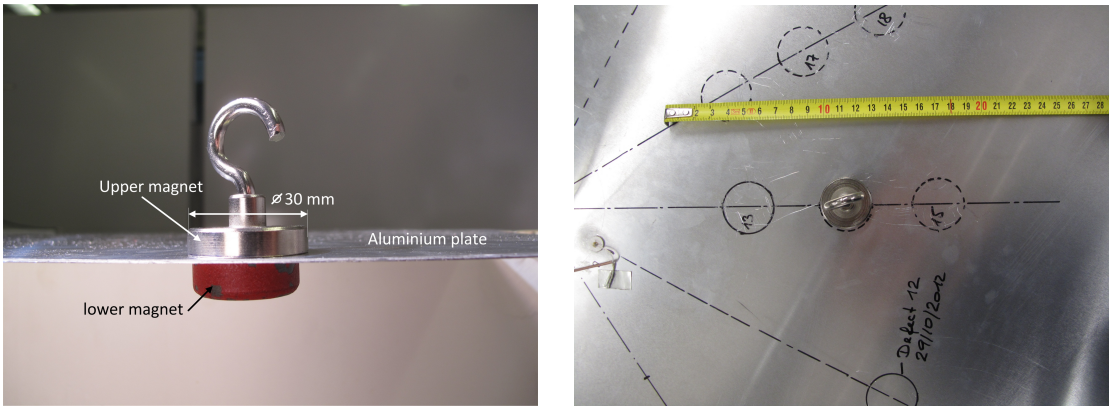

Figure 41: Photograph of the two permanent magnets with the aluminium plate between (left picture). The right picture shows the permanent magnet as a top view.

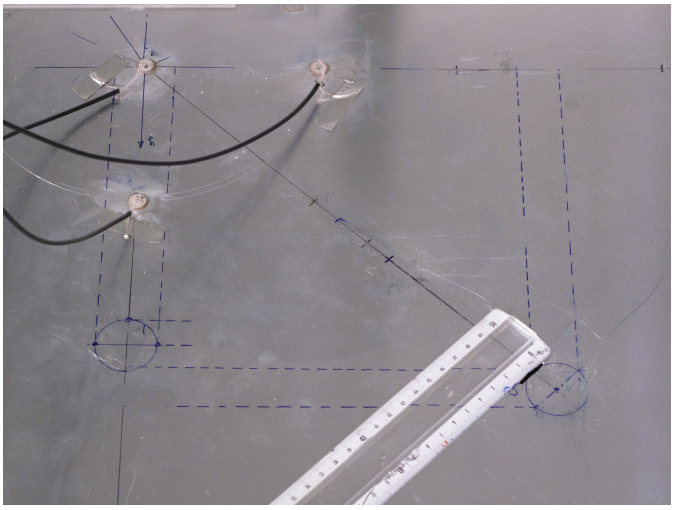

Figure 42: Photograph of the milled slot through the specimen structure.

In Fig.(38), the various components of the SHM system are illustrated together with the specimen structure for the validation test. The various components are: (1) the specimen structure, (2) the sensors/actuators and their arrangement, (3) three wireless sensor nodes and (4) the central server with graphical user interface and embedded signal processing.

For the experiments, three circular piezoelectric transducers (PTs) of type PZT 26 from Ferroperm Piezoceramics (www.ferroperm-piezo.com) were arranged on the structure. The PTs were placed firstly as a linear sensor arrangement (Fig.(43), left drawing) and secondly as rectangular sensor arrangement (Fig.(43), right drawing) on the structure. All PTs were permanently bonded onto the specimen structure by gluing. For the bonding, a two-component conductive adhesive was used, which was able to use the structure as common ground.

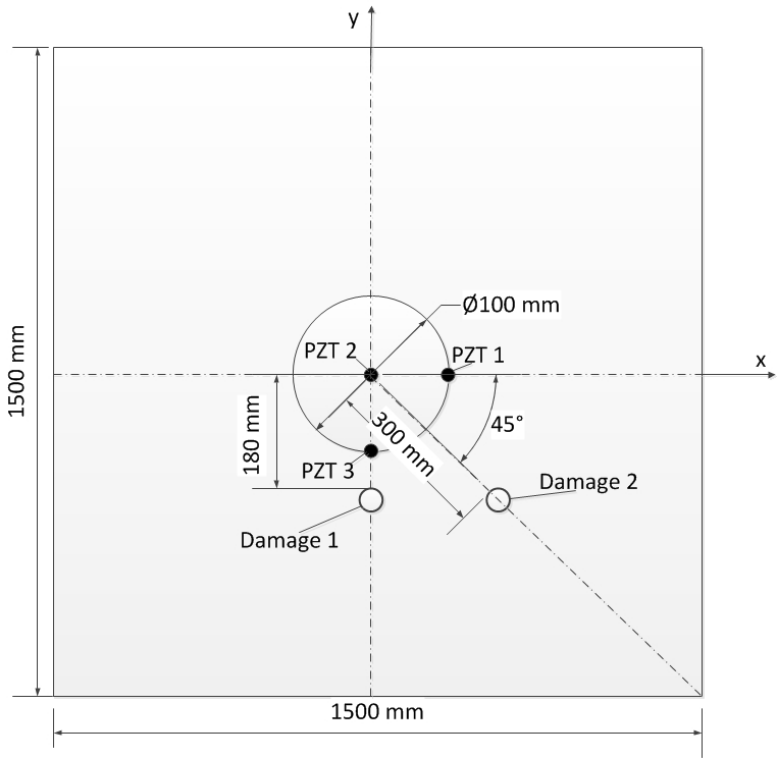

Figure 43: Drawing of the specimen structure with the sensor arrangement and the damage positions.

Table 12: Sensor arrangement selected for the present experiment.

Sensor arrangement		(x, y)
PZT 1	[mm]	(100, 0)
PZT 2	[mm]	(0, 0)
PZT 3	[mm]	(0, -100)

Excitation Signal

For exciting the Lamb waves into the structure a sine sweep signal with 18 cycles modulated with a Hamming window was used in the experiments. The amplitude of the excitation pulse was 60V peak-to-peak with a center frequency of 100 kHz. The values of the excitation signal parameters are listed in Table (13).

Table 13: Parameters for the excitation signal (present experiment).

Parameter 1	Value
Signal form	Sine burst modulated with Hamming window
Excitation frequency	100 kHz
Number of cycles	18
Signal amplitude	60 Vpp

5.4.2 Validation Results

The results section is split into two parts. In the first part, the results from the experiments with the reversible damage are described. In the second part the results for the milled slot in the specimen structure will be presented.

Results for Imperfection Position 1

The first damage position was chosen so that the reflected wave packet from the damage was overlapped by the incident wave packets. In Fig.(44), the signal measured at sensor position 3 (PZT 3) excited by sensor 1 (PZT 1) without the damage is shown as an example. The upper graph shows the signal resulting from the wireless measurement. In the lower graph, the time duration of the signal between the incident wave packet and the first reflected A_0 wave packets from the boundaries is limited.

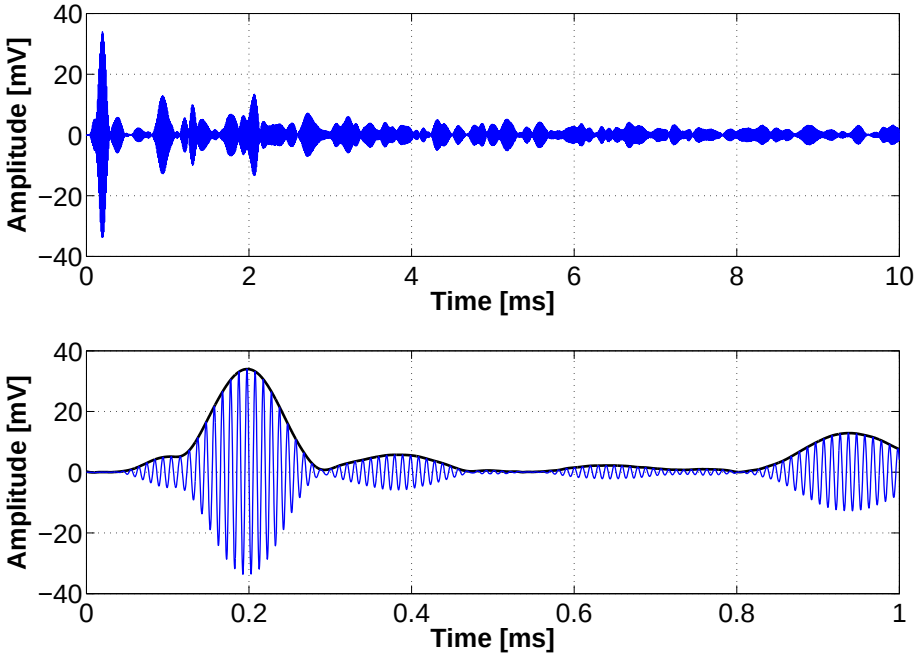

Figure 44: Example of a measured signal without damage. Actuator = PZT 1, sensor = PZT 3. Upper graph: measured signal during a 10 ms period. Lower graph: signal reduced to a time period of 1 ms (time period between incident signal and first reflection from the boundaries).

As a first step, the parameters of the incident wave packets within the measured signal are estimated using the developed estimation procedure described in chapter 3.3. In the measured signal (Fig.(44), lower graph) additional wave packets are present. These are caused by reflections from the edges of the structure. The S_0 reflected wave packets from the edges appear between 0.28 ms and 0.48 ms and those for the A_0 reflected wave packets between 0.81 ms and 1.5 ms. For the estimation process, only the S_0 reflected wave packets from the edges are considered, because the reflected wave packets from the first type of damage are expected to appear between the incident wave packets and the S_0 reflected wave packets from the edges. The results for the estimation process of the incident and reflected wave packet parameters are listed in Table (14). Differences from the simulation arise in the S_0 incident wave packet values for the dispersion coefficient

and the chirping parameter. This indicates weak dispersion of the real S_0 wave packet.

Table 14: Estimated values for the incident wave parameter.

$A_{A_{0inc}}$	$TOA_{A_{0inc}}$	Γ_{A0}	ψ_{A0}	$A_{S_{0inc}}$	$TOA_{S_{0inc}}$	Γ_{S0}	ψ_{S0}
0.98 mV	0.082 ms	0.1e-4	1e-8	0.42 mV	0.046 ms	1e-12	1e-6

Using the estimated wave parameters, the envelopes of the incident wave packets and the S_0 reflected wave packets are illustrated in Fig.(45).

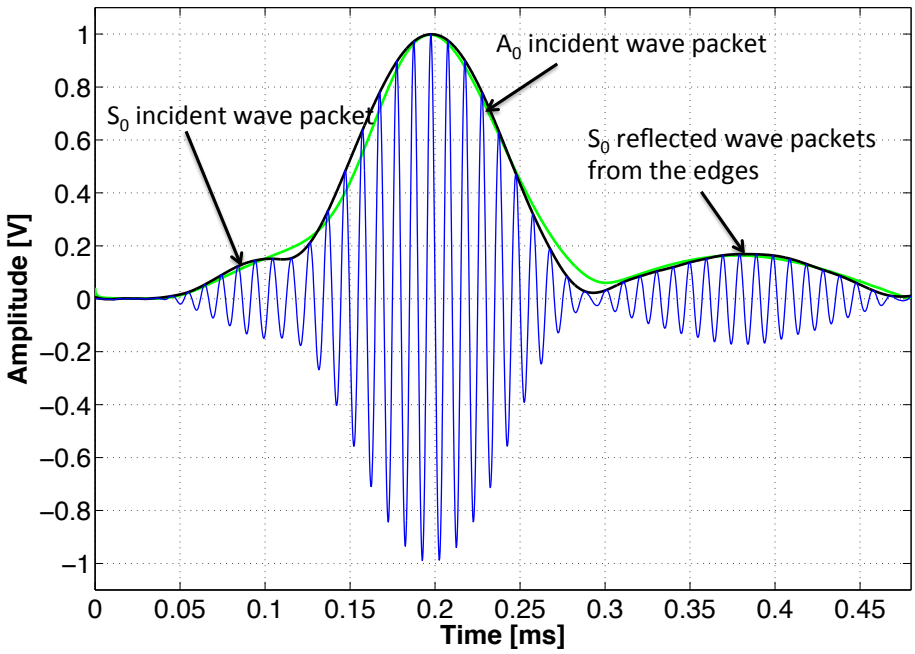

Figure 45: Reduced time section (0 - 0.45 ms) of the measured signal shown in Fig.(44). The first peak belongs to the S_{0inc} wave packet followed by the A_{0inc} wave packet. The wave packet following the A_{0inc} wave packet belongs to the reflected S_0 wave packets from the edges of the structure. (Black line: measured signal, Green line. estimated signal)

There is good agreement between the measured signal envelope (black line) and the estimated signal envelope (green line). The small deviation may be caused by additional environmental vibrations.

In the second step, the parameters of the reflected wave packet from the damage are estimated using the TOA estimation process developed in this work. In Fig.(46), the measured signals and their envelopes with damage (red curve) and without damage (blue curve) are illustrated. As above, only the measured signal at sensor position 3 (PZT 3) which is excited at sensor position 1 (PZT 1) is present. From the figure, it can be seen that the signal from the reflected wave packet from the damage is superimposed on the incident wave packet as well as on the reflected S_0 wave packets from the edges of the structure.

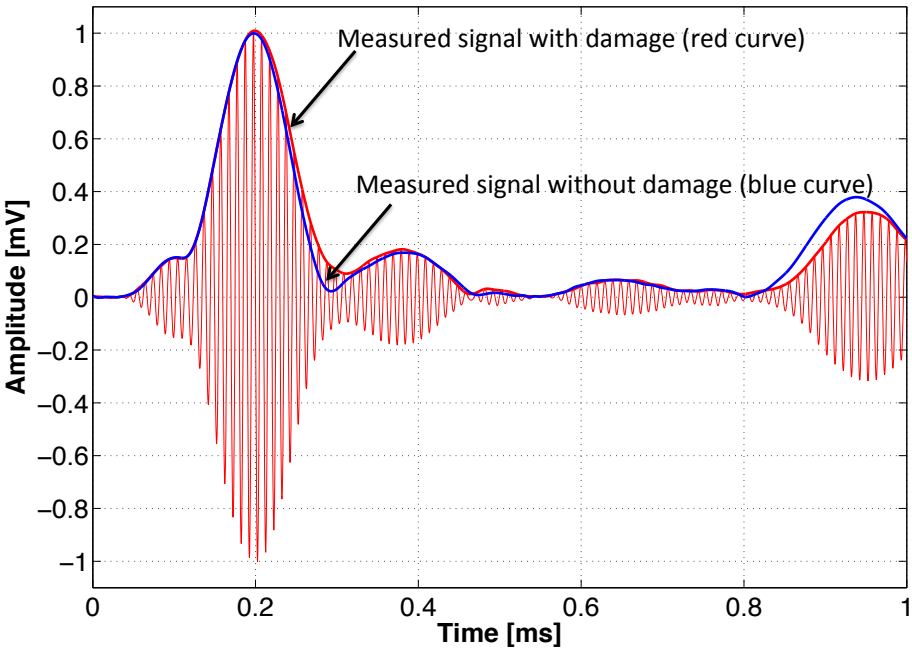

Figure 46: Measured signal with damage (red curve) and without damage (envelope of signal, blue curve).

For a better illustration, the reflected wave packet from the damage was re-calculated using the estimated wave parameters, as shown in Fig.(47). Here, the estimated TOA of the reflected A_0 wave packet from the damage is 0.272 ms. With a wave velocity of the A_0 wave packet of 1,120 m/s this results in a propagation distance between actuator, damage and sensor of 290 mm.

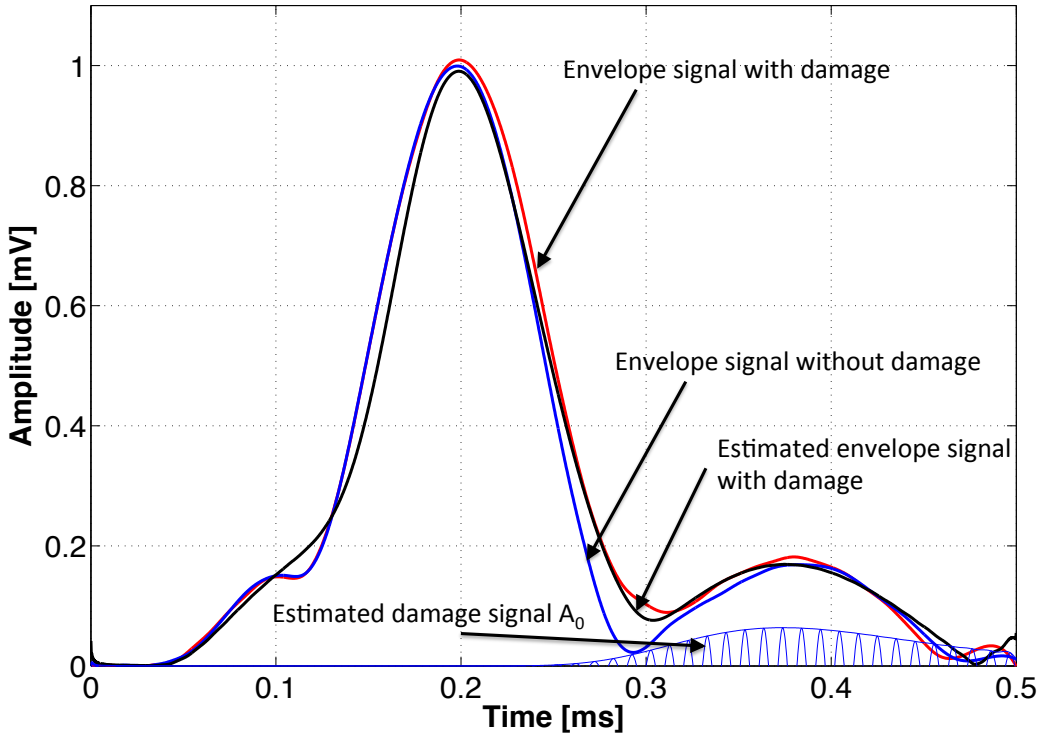

Figure 47: Envelope of measured signal without damage (blue line), envelope of measured signal with damage (red line) and estimated envelope with damage (black line). Calculated signal of A_0 wave packet reflected at the damage (blue curve).

The blue curve in Fig.(47) shows the envelope of the measured signal without damage, the red curve shows the envelope of the measured signal with damage and the black curve shows the estimated envelope of the damage signal. The estimated envelope signal shows slight deviations from the measured signal. However, despite these slight deviations, the parameters for the reflected wave packet from

the damage can be determined with sufficient accuracy. For the reflected S_0 wave packet no values for the wave parameters were estimated. This can be attributed to the fact that no S_0 wave packet was reflected at the damage. The time of arrival of the estimated damage signal A_0 within Fig.(47) correspondents with the real damage position.

The estimation process was applied to all signals measured at the sensor position and to the results for the estimated arrival time of the reflected A_0 wave packet at the damage site. The wave propagation distances thus calculated are listed in Table (15).

Table 15: Estimated values for the TOA and the wave propagation distances.

Propagation line [5]:	S_{12}	S_{13}	S_{23}	S_{21}	S_{31}	S_{32}
TOA:	0.34 ms	0.26 ms	0.23 ms	0.35 ms	0.26 ms	0.20 ms
Estimated distance:	381 mm	290 mm	250 mm	388 mm	290 mm	220 mm
Real distance:	385 mm	285 mm	260 mm	385 mm	285 mm	260 mm
Δr:	4 mm	15 mm	10 mm	3 mm	5 mm	40 mm

Results for Damage Localization - Damage 1

All calculated propagation distances are afterwards applied to the damage position estimation process described in the section above. The estimation of the damage position was carried out twice: once with trilateration using the intersection of ellipse lines and then using trilateration with the nonlinear least mean square procedure. The results are illustrated in Fig.(48). There, the sensor positions are marked as black filled circles, the real damage position is marked by a blue circle and the ellipses are drawn as ellipse lines around the sensor and damage positions. The intersection points of the ellipses are marked by blue circles. It can be seen from Fig.(48) that the ellipse lines do not intersect at the damage position which

[5]The term propagation line means the actuator-damage-sensor propagation distance. For example: S_{12} = PZT1-damage-PZT2 distance

correlates to the simulation results of the sensor arrangement described in the section above. This is in contrast to the calculation of the damage position using nonlinear LMS. Here, the estimated damage position correlates well with the real damage position.

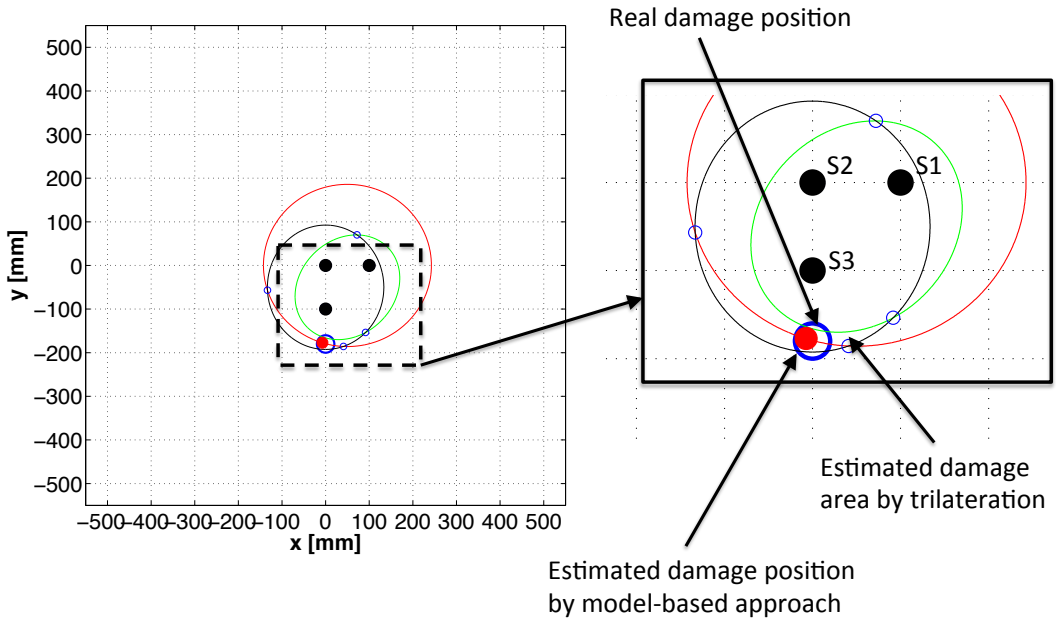

Figure 48: Results of the damage localization for damage 1. Blue circle = real damage position, red dot = estimated damage position using the model-based approach and points of ellipse intersection = estimated damage area using the trilateration method.

Results for Damage Position 2

The second position of the defect was chosen so that the reflected wave packet from the damage was not overlapped by the two incident wave packets. The results from the TOA estimation process and the calculated propagation distance of the reflected wave packet from the damage are listed in Table (16).

Table 16: Estimated values for the TOA and the wave propagation distances.

Propagation line [6]:	S_{12}	S_{13}	S_{23}	S_{21}	S_{31}	S_{32}
TOA:	0.40 ms	0.35 ms	0.40 ms	0.40 ms	0.34 ms	0.40 ms
Estimated distance:	451 mm	388 mm	453 mm	453 mm	385 mm	450 mm
Real distance:	458 mm	316 mm	458 mm	458 mm	316 mm	458 mm
Δr:	7 mm	72 mm	5 mm	5 mm	69 mm	8 mm

As before, the distances are applied to the damage estimation process carried out for the trilateration with ellipse intersection and for the trilateration with NLMS. The results are illustrated in Fig.(49).

[6]The term propagation line means the actuator-damage-sensor propagation distance. For example: S_{12} = PZT1-damage-PZT2 distance

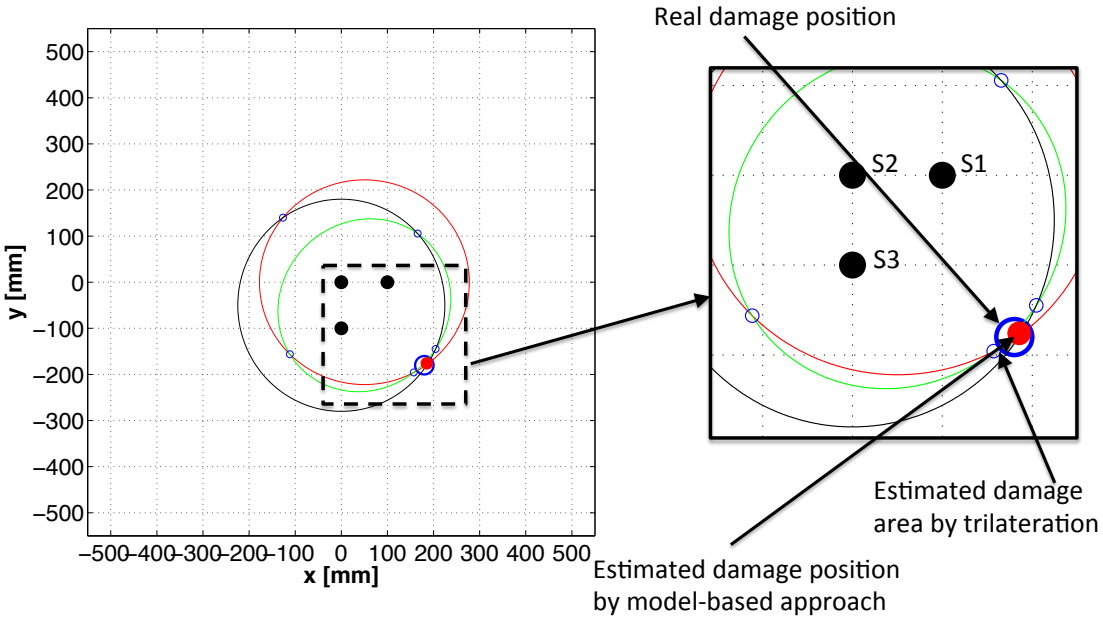

Figure 49: Results of the damage localization for damage 2. Blue circle = real damage position, red dot = estimated damage position using the model-based approach, points of ellipse intersections = estimated damage area using the trilateration method.

The results in Fig.(49) show good correlation between the estimated and the real position of the damage for both damage localization processes. As shown in the simulation for the ellipse intersection method, for this position of the damage and with exactly the same arrangement of sensors as used for this experiment, the position can be estimated sufficiently well. For a different damage position, the arrangement of the sensors must be changed. However, in reality this is not possible. The second introduced localization method using trilateration in combination with the nonlinear LMS, shows better results for a fixed sensor arrangement, which makes it more suitable for the estimation of the damage position.

Results for the Milled Slot in the Specimen Structure

After the experiments with removable defects on the structure, the structure was subjected to permanent damage. A slot was milled into the specimen structure in order to simulate a type of crack damage to the structure. The experiments with this type of real damage were only performed for one damage location on the structure. The results from the TOA estimation process and the calculated propagation distances of the reflected wave packet from the damage are listed in Table (17).

Table 17: Estimated values for the TOA and the wave propagation distances.

Propagation line [7]:	S_{12}	S_{13}	S_{23}	S_{21}	S_{31}	S_{32}
TOA:	0.39 ms	0.35 ms	0.37 ms	0.40 ms	0.32 ms	0.38 ms
Estimated distance:	436 mm	392 mm	414 mm	448 mm	358 mm	425 mm
Real distance:	440 mm	320 mm	440 mm	440 mm	320 mm	440 mm
Δr:	4 mm	72 mm	24 mm	8 mm	38 mm	15 mm

As in the experiment with the artificial damage, the TOA of the reflected wave packets from the damage are used for the determination of the crack position. The result for the ellipse intersection and for trilateration with NLMS are shown in Fig.(50).

[7]The term propagation line means the actuator-damage-sensor propagation distance. For example: S_{12} = PZT1-damage-PZT2 distance

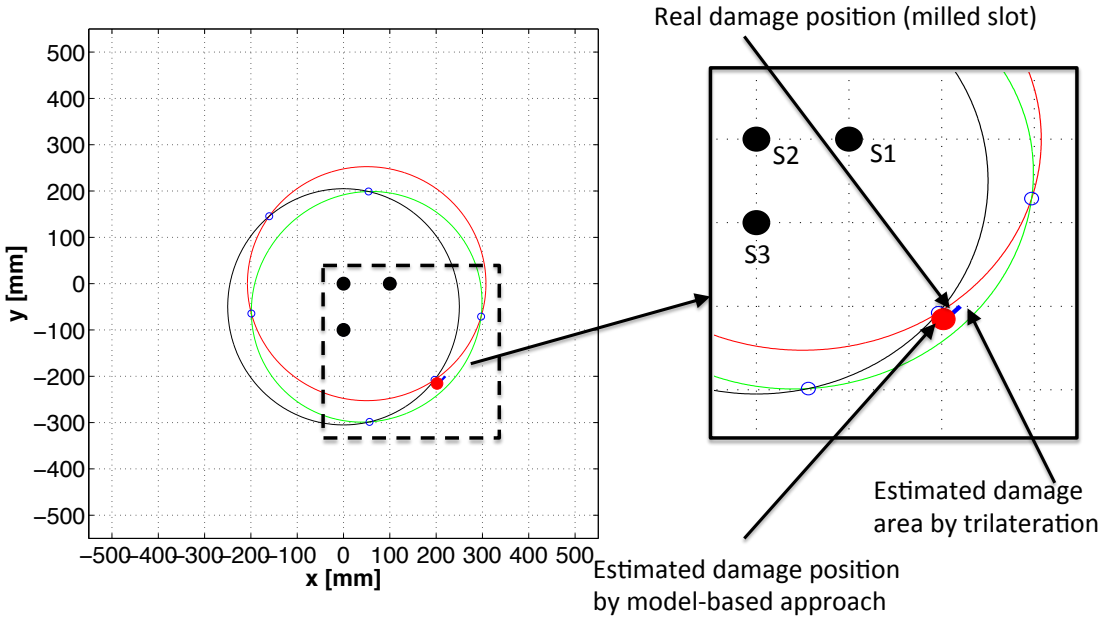

Figure 50: Result of the damage localization for the milled slot. Blue line = real damage position, red dot = estimated damage position using the model-based approach, points of ellipse intersections = estimated damage area using the trilateration method.

Here, it is clearly shown that it is in principle possible to estimate the position of the crack damage using either localization method. The intersection method, however, results in a relatively large area between the intersection points of the ellipses, which in turn means a large potential area for the location of the damage. As demonstrated in the experiment above, the localization method with trilateration in combination with NLMS shows better results for the estimated damage position. For this reason, the trilateration localization method in combination with NLMS is recommended in preference to the method of intersection of ellipse lines.

5.4.3 Discussion of Results

As has been discussed in the simulation for the different sensor arrangements, the selection of the sensor arrangement has an impact on the results of the damage position estimation. For a damage position nearly perpendicular to the sensor arrangement (x-axis or y-axis) the rectangular sensor arrangement provides no useful results. In these areas the individual ellipses do not overlap. By using the linear sensor arrangement the estimation of the damage position is possible, but less precise.

The experiments showed generally that with increasing distance of the damage away from the sensor arrangement, the estimated damage area increases. The results from the sensor arrangement simulation showed that when using the trilateration method for damage detection it is not possible to estimate the damage position when it is at a distance greater than five times the size of the sensor arrangement. In these cases another location method may be more efficient.

The results for the estimation of the real damage show good agreement with the real damage position. The measured results shown in Fig.(50) are for the experiment with a crack length of 30 mm.
Compared to the measurements with the removable defect, the results of the simulated crack in the aluminium plate show a higher amplitude. That may be expected because the change of the structure behaviour due to the removable defect is less pronounced. However, it must be clearly stated that neither of the defects occurs in reality. The selected defects are only an approximation to reality and are used to verify the functionality of the SHM system. In order to test the system for the planned application, a structure specified in the requirement list must be used. Furthermore, this structure must to be loaded in a fatigue test until a crack occurs. These experiments are planned in collaboration with the two project partners mentioned at the beginning. Only through these real load tests will it be possible to tune the system for the desired application.

6 Conclusion

6.1 Summary

As stated in the introduction, modern structures no longer represent stand-alone solutions; the trend is towards structure systems. This means that structures will become more "intelligent" in the future. A key element of such structure systems will be data processing. In this work, the data processing is a mathematical reflection of the entire physical behaviour of the structure system.

Here, the scientific focus was on the introduction of a new data processing concept for structure systems, with the goal of monitoring the integrity of a structure. The main difference, in comparison to existing data processing solutions for the monitoring of structures (structural-health monitoring), is the ability of the proposed solution to adapt to situations which are not previously known. This is made possible through a combination of approximated analytical mathematical models of the predictable physical processes and adaptive mathematical models for previously unknown physical processes such as damage events or environmental effects on the structure system.

At the beginning of this work, existing data processing solutions for structure monitoring are discussed and compared with the new software approach. The resulting comparison is illustrated in a diagram which could be used as a kind of standard for assessing the requirements of a software for structural monitoring.

Most of this thesis consists of the introduction of a novel data processing approach for the extraction of damage-related features within a measured signal. First, the theoretical background is discussed and the proposed concept is derived. A practical example of the data processing approach is then given based on the analysis of Lamb wave signals. The subsequent proof of concept is based on a practical example where the signals for the test of the proposed damage feature extraction process (data processing) are synthetically calculated signals, because this allows the possibility of tuning the input signal for the procedure and testing towards the boundaries.

Focusing only on the scientific part –the introduction of the novel data processing concept for structural systems –would not be sufficient, because for an

in-depth consideration of the structural system the various components involved in the concept must be considered. Therefore, an entire structural-health monitoring system, consisting of sensor arrangement, wireless data acquisition and damage localization algorithm, was developed in the framework of this thesis. The development steps, including all the necessary simulations and the practical testing of the entire system, are explained in the second part of the thesis.

It should be noted that the validation of the proposed data processing method was limited to following assumptions:

- Only the first two Lamb wave modes are consider (first symmetrical- S_0, and first anti-symmetrical mode A_0,
- The simulated signals and the practical test are based on a wave propagation in an isotropic material,
- Effects caused by the piezoelectric actuators or sensors are not taken into account,
- For the estimation of the damage features only the reflected wave packets form the damage are consider. Scattered wave packets are not taken into account,
- The geometrical complexity of the assumed structure for the simulation and for the practical test are limited to a rectangular plate without curvature,
- No attentional structure elements such as rivets or stringers are taken into account,
- A monitoring of possible detachments (partially or completely) of the piezoelectric transducers are not taken into account,
- It is assumed that no ageing is effecting the piezoelectric transducers or the structure.

Furthermore, the present wireless measurement system has following limitations:

- The transmission distance (100 m) was only tested for indoor applications,

- The connection between sensor node and piezoelectric transducer is wire based,
- Only the excitation frequency of the wave pulse can be varied. All other parameters such as wave pulse amplitude, wave pulse shape or measuring time (10 ms) are fix defined within the system and can not be changed,
- The wireless system is not validated against a common standard (e.g. CE standard) and is not approved for the use in aerospace applications.

To summarise, the SHM system developed in this thesis is also not yet ready for real-world applications, but nevertheless, preparatory work for reaching this goal has been undertaken. With the considerations and methods developed here, it should be possible to develop an SHM system based on guided waves for various applications in plate-like structures. In principle, the application is not limited to aircraft. Further applications could be found in various fields where lightweight structures are used. Furthermore, the system is not restricted to aluminium structures. Various tests on CFRP plates undertaken during the experimental phase of this work demonstrated the functionality of the SHM system for this type of material also.

6.2 Further Work and Outlook

From the viewpoint of the author, the future for data processing and damage feature extraction in the field of structural-health monitoring will involve the representation of the involved physical processes by mathematical models of a type corresponding with Level 6 (the highest level) as listed in Fig.(4). Although the examples presented in this work demonstrated reasonable performance, the potential of the model-based approach is far from being fully exploited. For example, in this work, only the measured signals gained from the piezoelectric transducers were taken into account, but in principle several other readings from other sensors, such as temperature or vibration sensors, could also be taken into account. Of course, the consideration of further data results in the need for more mathematical models, which increases the complexity of the entire damage feature

extraction procedure, but the reliability of the information obtained will increase, even in cases where there are missing data. The author therefore recommends implementing the presented solution with data from multiple sensors.

In summary, following further investigations on the proposed data processing method for damage feature extraction are recommenced:

- Even though the proposed data processing method are able to handle the case of multiple damages, this ability was not tested in the framework of this thesis,

- The proposed method should be adapted to more realistic and therefore more complicated structures. For instance, multiple reflections of the incident wave pulse at a fastener row or at multiple stringers should be a topic of investigation,

- As stated above, the feasibility of the proposed data processing method was limited to isotropic wave propagation, and the case of anisotropic wave propagation as for example in composite material was not considered in this thesis. The expansion of the proposed data processing method to anisotropic wave propagation would expand the proposed method to further applications, such as for example monitoring applications of structures made of composite,

- In this thesis only the reflected wave pulses from a damage is considered as possible damage feature. But, in order to increase the sensibility of the SHM system also the scattered wave pulses from the damage should be considered in the mathematical model,

There is no doubt that an integrated SHM system can reduce operating costs for an aircraft. This makes the application of the SHM system very interesting for airlines. However, most SHM systems are not ready for applications in commercial aircraft. Many laboratory-based SHM systems are available, but none of these systems has yet been integrated into a real application. There is a clear need to bring the systems from the laboratory stage of development into real applications.

A further follow-up project is planned on a wind turbine in order to monitor its rotor blades. The material of the rotor blades is CFRP. The aim of this project is

to be able to detect impact damage to the rotor blades. The use of an autonomous wireless monitoring system is a particular advantage for this type of application. By combining the wireless system with an energy-harvesting system, the system developed here can provide some advantages for such applications. Using the procedure described in this work and the developed simulation, it should be possible to use an SHM system for this application.

References

[1] C. R. Farrar and K. Worden, *Structural Health Monitoring: A Machine Learing Perspective*. Wiley, 2012.

[2] K. Worden and J. M. Dulieu-Barton, "An overview of intelligent fault detection in systems and structures," *Structural Health Monitoring*, vol. 3, no. 1, pp. 85–98, 2004.

[3] P. Qiu, *Introduction to Statistical Process Control*. Chapman and Hall, 2014.

[4] Y. Ling and S. Mahadevan, "Integration of structural health monitoring and fatigue damage prognosis," *Mechanical Systems and Signal Processing*, vol. 28, pp. 89 – 104, 2012.

[5] V. Giurgiutiu, *Structural Health Monitoring with Piezoelectric Wafer Active Sensors*. Academic Press, 2008.

[6] W. Staszewski, S. Mahzan, and R. Traynor, "Health monitoring of aerospace composite structures - active and passive approach," *Composites Science and Technology*, 2009.

[7] C. Boller, F.-K. Chang, and Y. Fujino, *Encyclopedia of structural health monitoring*, vol. 1. New York: Wiley, 2009.

[8] C. Boller and M. Buderath, "Fatigue in aerostructures - where structural health monitoring can contribute to a complex subject," *Philosophical transactions of the royal society A*, vol. 365, pp. 561–587, 2007.

[9] P. de Castro, S. Travares, V. Richter-Trummer, P. de Matos, P. Moreira, and L. da Silva, "Damage tolerance of aircraft panles," *Revista da Associacao Portuguesa de Analise Experimental de Tensoes*, vol. ISSN 1646-7078, 2010.

[10] W. Staszewski, C. Boller, and G. R. Tomlinson, *Health monitoring of aerospace structures: smart sensor technologies and signal processing*. John Wiley & Sons, 2004.

[11] J. V. Candy, *Model-based signal processing*, vol. 36. John Wiley & Sons, 2005.

[12] K. Worden, C. R. Farrar, G. Manson, and G. Park, "The fundamental axioms of structural health monitoring," in *Proceedings of the Royal Society of London A: Mathematical, Physical and Engineering Sciences*, vol. 463, pp. 1639–1664, The Royal Society, 2007.

[13] C. R. Farrar, P. J. Cornwell, S. W. Doebling, M. B. Prime, *et al.*, "Structural health monitoring studies of the alamosa canyon and i-40 bridges," *Los Alamos National Laboratory, Los Alamos, NM, Technical Report LA-13635-MS*, 2000.

[14] A. J. Croxford, J. Moll, P. D. Wilcox, and J. E. Michaels, "Efficient temperature compensation strategies for guided wave structural health monitoring," *Ultrasonics*, vol. 50, no. 4, pp. 517–528, 2010.

[15] G. Liu, Y. Xiao, H. Zhang, and G. Ren, "Baseline signal reconstruction for temperature compensation in lamb wave-based damage detection," *Sensors*, vol. 16, no. 8, 2016.

[16] M. Salmanpour, Z. S. Khodaei, and M. Aliabadi, "Guided wave temperature correction methods in structural health monitoring," *Journal of Intelligent Material Systems and Structures*, vol. 28, no. 5, pp. 604–618, 2017.

[17] M.-A. Torres-Arredondo, J. Sierra-Pérez, and G. Cabanes, "An optimal baseline selection methodology for data-driven damage detection and temperature compensation in acousto-ultrasonics," *Smart Materials and Structures*, vol. 25, no. 5, p. 055034, 2016.

[18] A. J. Dawson, J. E. Michaels, and T. E. Michaels, "Isolation of ultrasonic scattering by wavefield baseline subtraction," *Mechanical Systems and Signal Processing*, vol. 70-71, pp. 891 – 903, 2016.

[19] J. Chen, Z. Li, J. Pan, G. Chen, Y. Zi, J. Yuan, B. Chen, and Z. He, "Wavelet transform based on inner product in fault diagnosis of rotating machinery: A review," *Mechanical Systems and Signal Processing*, vol. 70-71, pp. 1 – 35, 2016.

[20] A. Oppenheim and R. Schafer, *Discrete-time signal processing*. Prentice Hall, New Jersey, 2010.

[21] B. Xu and V. Giurgiutiu, "Single mode tuning effects on lamb wave time reversal with piezoelectric wafer active sensors for structural health monitoring," *Journal of Nondestructive Evaluation*, vol. 26, pp. 123–134, 2007.

[22] J.-B. Ihn and F.-K. Chang, "Pitch-catch active sensing methods in structural health monitoring for aircraft structures," *Structural Health Monitoring*, vol. 7, no. 1, pp. 5–19, 2008.

[23] V. Giurgiutiu and A. Cuc, "Embedded non-destructive evaluation for structural health monitoring, damage detection, and failure prevention," *Shock and Vibration Digest*, vol. 37, no. 2, p. 83, 2005.

[24] M. G. Droubi, N. H. Faisal, F. Orr, J. A. Steel, and M. El-Shaib, "Acoustic emission method for defect detection and identification in carbon steel welded joints," *Journal of Constructional Steel Research*, vol. 134, pp. 28 – 37, 2017.

[25] M. M. R. Taha, A. Noureldin, J. L. Lucero, and T. J. Baca, "Wavelet transform for structural health monitoring: A compendium of uses and features," *Structural Health Monitoring*, vol. 5, no. 3, pp. 267–295, 2006.

[26] S. Dong, M. Yuan, Q. Wang, and Z. Liang, "A modified empirical wavelet transform for acoustic emission signal decomposition in structural health monitoring," *Sensors*, vol. 18, no. 5, 2018.

[27] A. Sarrafi and Z. Mao, "Statistical modeling of wavelet-transform-based features in structural health monitoring," in *Model Validation and Uncertainty Quantification, Volume 3* (S. Atamturktur, T. Schoenherr, B. Moaveni, and C. Papadimitriou, eds.), (Cham), pp. 253–262, Springer International Publishing, 2016.

[28] J. Chen, J. Rostami, P. W. Tse, and X. Wan, "The design of a novel mother wavelet that is tailor-made for continuous wavelet transform in extracting defect-related features from reflected guided wave signals," *Measurement*, vol. 110, pp. 176 – 191, 2017.

[29] J. Amezquita-Sanchez and H. Adeli, "Signal processing techniques for vibration-based health monitoring of smart structures," *Archives of Computational Methods in Engineering*, vol. 23, no. 1, pp. 1–15, 2016.

[30] A. Noel, A. Abdaoui, A. Badawy, T. Elfouly, M. Ahmed, and M. Shehata, "Structural health monitoring using wireless sensor networks: A comprehensive survey," *IEEE Communications Surveys Tutorials*, vol. PP, no. 99, pp. 1–1, 2017.

[31] H. Park, H. Lee, H. Adeli, and I. Lee, "A new approach for health monitoring of structures: terrestrial laser scanning," *Computer-Aided Civil and Infrastructure Engineering*, vol. 22, no. 1, pp. 19–30, 2007.

[32] H. Sohn, K. Worden, and C. Farrar, "Novelty detection using auto-associative neural network," tech. rep., Los Alamos National Lab., NM (US), 2001.

[33] S. Haykin, "Neural networks: A comprehensive approach," *IEEE Computer Society Press*, 1994.

[34] Z. Su and L. Ye, "Lamb wave-based quantitative identification of delamination in cf/ep composite structures using artificial neural algorithm," *Composite Structures*, vol. 66, no. 1, pp. 627–637, 2004.

[35] H.-F. Lam, K.-V. Yuen, and J. L. Beck, "Structural health monitoring via measured ritz vectors utilizing artificial neural networks," *Computer-Aided Civil and Infrastructure Engineering*, vol. 21, no. 4, pp. 232–241, 2006.

[36] Y. Bao, Z. Tang, H. Li, and Y. Zhang, "Computer vision and deep learning–based data anomaly detection method for structural health monitoring," *Structural Health Monitoring*, p. 1475921718757405, 2018.

[37] R. Zhao, R. Yan, Z. Chen, K. Mao, P. Wang, and R. X. Gao, "Deep learning and its applications to machine health monitoring," *Mechanical Systems and Signal Processing*, vol. 115, pp. 213–237, 2019.

[38] Y.-J. Cha, W. Choi, G. Suh, S. Mahmoudkhani, and O. Büyüköztürk, "Autonomous structural visual inspection using region-based deep learning for

detecting multiple damage types," *Computer-Aided Civil and Infrastructure Engineering*, vol. 33, no. 9, pp. 731–747, 2018.

[39] M. Birchmeier, D. Gsell, M. Juon, A. Brunner, R. Paradies, and J. Dual, "Active fiber composites for the generation of lamb waves," *Ultrasonics*, vol. 1, pp. 73–82, 2009.

[40] D. V. Widder, *Laplace transform (PMS-6)*. Princeton university press, 2015.

[41] C. Zang, M. I. Friswell, and M. Imregun, "Structural health monitoring and damage assessment using measured frfs from multiple sensors, part i: The indicator of correlation criteria," in *Key Engineering Materials*, vol. 245, pp. 131–140, Trans Tech Publ, 2003.

[42] F. Lanza di Scalea, S. Sternini, and A. Y. Liang, "Robust passive reconstruction of dynamic transfer function in dual-output systems," *The Journal of the Acoustical Society of America*, vol. 143, no. 2, pp. 1019–1028, 2018.

[43] B. Peeters and G. De Roeck, "One-year monitoring of the z24-bridge: environmental effects versus damage events," *Earthquake engineering & structural dynamics*, vol. 30, no. 2, pp. 149–171, 2001.

[44] F. Magalhães, A. Cunha, and E. Caetano, "Vibration based structural health monitoring of an arch bridge: from automated oma to damage detection," *Mechanical Systems and Signal Processing*, vol. 28, pp. 212–228, 2012.

[45] H. Park, H. Lee, H. Adeli, and I. Lee, "A new approach for health monitoring of structures: terrestrial laser scanning," *Computer-Aided Civil and Infrastructure Engineering*, vol. 22, no. 1, pp. 19–30, 2007.

[46] S. G. Mallat and Z. Zhang, "Matching pursuits with time-frequency dictionaries," *IEEE Transactions on signal processing*, vol. 41, no. 12, pp. 3397–3415, 1993.

[47] A. Raghavan and C. E. Cesnik, "Guided-wave signal processing using chirplet matching pursuits and mode correlation for structural health monitoring," *Smart Materials and Structures*, vol. 16, no. 2, p. 355, 2007.

[48] B. Xu, V. Giurgiutiu, and L. Yu, "Lamb waves decomposition and mode identification using matching pursuit method," in *SPIE Smart Structures and Materials+ Nondestructive Evaluation and Health Monitoring*, pp. 72920I–72920I, International Society for Optics and Photonics, 2009.

[49] L. De Marchi, M. Ruzzene, B. Xu, E. Baravelli, and N. Speciale, "Warped basis pursuit for damage detection using lamb waves," *IEEE transactions on ultrasonics, ferroelectrics, and frequency control*, vol. 57, no. 12, 2010.

[50] S. Kulkarni and J. Achenbach, "Structural health monitoring and damage prognosis in fatigue," *Structural Health Monitoring*, vol. 7, no. 1, pp. 37–49, 2008.

[51] Q. Zhang, "Statistical damage identification for bridges using ambient vibration data," *Computers and Structures*, vol. 85, no. 7, pp. 476 – 485, 2007.

[52] A. Mosavi, D. Dickey, R. Seracino, and S. Rizkalla, "Identifying damage locations under ambient vibrations utilizing vector autoregressive models and mahalanobis distances," *Mechanical Systems and Signal Processing*, vol. 26, pp. 254 – 267, 2012.

[53] M. W. Vanik, J. L. Beck, and S. K. Au, "Bayesian probabilistic approach to structural health monitoring," *Journal of Engineering Mechanics*, vol. 126, no. 7, pp. 738–745, 2000.

[54] E. B. Flynn, M. D. Todd, P. D. Wilcox, B. W. Drinkwater, and A. J. Croxford, "Maximum-likelihood estimation of damage location in guided-wave structural health monitoring," *The Royal Society*, vol. 467, no. 2133, pp. 2575–2596, 2011.

[55] L. Qiu, S. Yuan, F.-K. Chang, Q. Bao, and H. Mei, "On-line updating gaussian mixture model for aircraft wing spar damage evaluation under time-varying boundary condition," *Smart Materials and Structures*, vol. 23, no. 12, p. 125001, 2014.

[56] E. Kreyszig, *Advanced Engineering Mathematics*. Wiley, 2010.

[57] L. A. Overbey, C. C. Olson, and M. D. Todd, "A parametric investigation of state-space-based prediction error methods with stochastic excitation for structural health monitoring," *Smart Materials and Structures*, vol. 16, no. 5, p. 1621, 2007.

[58] M. Todd, J. Nichols, L. Pecora, and L. Virgin, "Vibration-based damage assessment utilizing state space geometry changes: local attractor variance ratio," *Smart Materials and Structures*, vol. 10, no. 5, p. 1000, 2001.

[59] K. Worden, C. R. Farrar, J. Haywood, and M. Todd, "A review of nonlinear dynamics applications to structural health monitoring," *Structural Control and Health Monitoring*, vol. 15, no. 4, pp. 540–567, 2008.

[60] A. French, "Vibrations and waves," *The M.I.T. Introductory Physics Series*, vol. 41, pp. 59–68, 2008.

[61] A. P. Ruszczyński and A. Ruszczynski, *Nonlinear optimization*, vol. 13. Princeton university press, 2006.

[62] H. Lamb, "On waves in an elastic plate," *Proceedings of the Royal Society of London*, vol. 93, no. Series A, Containing papers of a Mathematical and Physical Character, pp. 114–128, 1971.

[63] J. Rose, *Ultrasonic waves in solid media*. Cambridge University Press.

[64] D. Li, M. Jin, and Q. Feng, "Plate-like structure damage acoustic emission beamforming array technique and probability-based diagnostic imaging method," in *Non-Destructive Testing* (F. P. G. Marquez, M. Papaelias, and N. Zaman, eds.), ch. 3, Rijeka: IntechOpen, 2016.

[65] P. Caweley and D. Alleyne, "The use of lamb waves for long range inspection of large structrues," *Ultrasonics*, vol. 34, pp. 287–290, 1996.

[66] V. Giurgiutiu, J. Boa, and W. Zhao, "Piezoelectric wafer active sensor embedded ultrasonic in beams and plates," *Experimental Mechanics 43*, vol. 4, pp. 428–449, 2003.

[67] S. M. Prasad, K. Balasubramaniam, and C. Krishnamurthy, "Structural health monitoring of composite structures using lamb wave tomography," *Smart materials and structures*, vol. 13, no. 5, p. N73, 2004.

[68] R. A. Osegueda, V. Kreinovich, S. Nazarian, and E. Roldan, "Detection of cracks at rivet holes in thin plates using lamb-wave scanning," *Proc.SPIE*, vol. 5047, pp. 5047 – 5047 – 12, 2003.

[69] P. Tua, S. Quek, and Q. Wang, "Detection of cracks in plates using piezo-actuated lamb waves," *Smart Materials and Structures*, vol. 13, no. 4, p. 643, 2004.

[70] D. Alleyne and P. Cawley, "The interaction of lamb waves with defects," *IEEE Transactions on Ultrasonics, Ferroelectrics, and Frequency Control*, vol. 39, no. 3, pp. 381–397, 1992.

[71] P. Wilcox, M. Lowe, and P. Cawley, "A signal processing technique to remove the effect of dispersion from guided wave signals," *AIP Conference Proceedings*, vol. 39, pp. 381–397, May 1992.

[72] L. Liu and F. Yuan, "A linear mapping technique for dispersion removal of lamb waves," *Structural Health Monitoring*, Sep. 2009.

[73] I. Mason, D. Buchanan, and A. Booer, "Channel wave mapping of coal-seams in the united kingdom," *Geophysics*, vol. 45, pp. 1131–1143, 1980.

[74] G. Smith and I. Mason, "A parametric approach to the compression of seismic by frequency transformation," *Geophysical Prospecting*, vol. 28, pp. 551–571, 1980.

[75] A. Booer, J. Chambers, and I. Mason, "Fast numerical algorithm for the recompression of dispersed time signals," *Electronic Letters*, vol. 13, pp. 453–456, 1980.

[76] S. J. Orfanidis, *Electromagnetic Waves and Antennas*. Prentice Hall, 2003.

[77] J. Lynch, "Design of a wireless active sensing unit for localized structural health monitoring," *Structural Control and Health Monitoring*, vol. 12 (3-4), pp. 405–423, 2005.

[78] J. Lynch and J. Kenneth, "A summary review of wireless sensors and sensor networks for structural health monitoring," *The Shock and Vibration Digest*, vol. 38, pp. 91–128, 2006.

[79] C. Dürager, A. Heinzelmann, and D. Riederer, "A wireless sensor system for structural health monitoring with guided ultrasonic waves and piezoelectric transducers," *Structure and Infrastructure Engineering*, vol. 11, pp. 1177–1186, Nov. 2013.

[80] X. Zhao, "Active health monitoring of an aircraft wing with embedded piezoelectric sensor/actuator network: Ii. wireless approaches," *Smart Materials and Structures*, vol. 16, no. 4, pp. 1218–1225, 2007.

[81] C. Farrar, G. Park, D. Allen, and M. Todd, "Sensor network paradigms for structural health monitoring," *Structural Control and Health Monitoring*, vol. 13, no. 1, pp. 210–225, 2006.

[82] Y. Wang, J. Lynch, and K. Law, "A wireless structural health monitoring system with multithreaded sensing devices: design and validation," *Structure and Infrastructure Engineering*, vol. 3, no. 2, pp. 103–120, 2007.

[83] N. Xu, S. Rangwala, K. Chintalapudi, D. Ganesan, A. Broad, R. Govindan, and D. Estrin, "A wireless sesnor network for structural monitoring," *ACM SensSys '04 international conference on Embedded networked sensor systems*, Nov. 2004.

[84] C. Dürager, "Energy harvesting for wireless sensors by using piezoelectric transducers," *6th European Workshop on Structural Health Monitoring - Tu.3.C.1*, 2012.